The Tantalum isotope inventory of terrestrial and early solar system materials

Inaugural-Dissertation

zur

Erlangung des Doktorgrades

der Mathematisch-Naturwissenschaftlichen Fakultät

der Universität zu Köln

vorgelegt von

Markus Pfeifer

aus Koblenz

Köln, 2017

Berichterstatter	Prof. Dr. Carsten Münker
(Gutachter)	
	PD Dr. Dominik Hezel
Tag der mündlichen Prüfung	18.01.2017

Abstract

Tantalum is the rarest stable element in the solar system and consists of two stable isotopes with a huge difference in abundances (^{180}Ta = ~0.012% and ^{181}Ta = ~99.988%), making ^{180}Ta the rarest stable nuclide in the solar system. Tantalum isotopes are produced together with other heavy isotopes during stellar nucleosynthesis in stars at the end of their life, in red giants as well as in supernova explosions. While ^{181}Ta has been produced by the rapid and slow neutron capture processes (r- and s-process), the rare isotope ^{180}Ta is bred by the branched s- process and by the special neutrino-process, which is only significant for one further heavy nuclide, ^{138}La. Tantalum-180 is the only observationally stable nuclide in an excited nuclear state. Because of this property, nuclear astrophysics has long searched for viable production mechanism to explain the abundance of ^{180}Ta in the solar system. As the earliest materials of the solar system are known to carry nucleosynthetic anomalies as fingerprints of their stellar origin, astrophysical models of Ta nucleosynthesis might be tested in meteorites. The low abundance of ^{180}Ta relative to isotopes of similar mass including ^{181}Ta make Ta isotope compositions to a sensitive tracer of ingrowth from nuclear reactions in neighboring elements like Hf in the early solar system.

In modern geochemistry, Ta is a key trace element, belonging to the group of high field strength elements (HFSE, *i.e.*, Zr, Nb, Hf, Ta). Due to analytical difficulties related to the low abundance of ^{180}Ta, the absolute isotope composition of tantalum is one of the least constrained of any naturally occurring elements and possible natural variations in ^{180}Ta/^{181}Ta have so far not been investigated. The unusual production and physical properties of ^{180}Ta might render Ta isotope compositions useful for tracing nucleosynthetic input or irradiation in the early solar system. Substantial analytical development was required in order to evaluate possible variations of Ta isotope compositions in solar system materials and whether natural Ta stable isotope variations exist on Earth.

Following the introduction to Ta isotope geo- and cosmochemistry in **Chapter I, Chapter II** presents the analytical protocol to obtain high-precision Ta isotopes data and introduces an improved value for the absolute Ta isotope ratio. Using a Neptune^{TM} multicollector-inductively coupled plasma-mass spectrometer (MC-ICP-MS) and different resistors in the Faraday cup amplifier feedback loops (a 10^{10} Ω for ^{181}Ta; 10^{12} or newly developed 10^{13} Ω resistors for ^{180}Ta and Hf interference monitor isotopes) now allows relative analyses of ^{180}Ta/^{181}Ta with an intermediate precision (external reproducibility) of *ca.* ±4 ε (ε refers to one part in 10,000) using 25 to 100 ng Ta and thus even for sample sizes available from meteorites (e.g., 1 g of sample required). The 10^{13} Ω amplifier resistors proved to be of paramount importance for high-precision Ta isotope ratio measurements of low amounts of material. Tailing effects from the large ^{181}Ta beam have previously been underestimated. A thorough assessment of this effect revealed a tailing contribution of ~2.5 %

on the currently recommended IUPAC ratio. Potential systematic biases in the mass discrimination correction are assumed being of minor importance compared to an uncertainty of ~0.4 % achieved for the estimate of the "true" $^{180}Ta/^{181}Ta$ ratio. This work proposes a revised $^{180}Ta/^{181}Ta$ isotope ratio of 0.00011705(41), equivalent to $^{181}Ta/^{180}Ta$ = 8543(30), yielding isotope abundances of 0.011704(41) % for ^{180}Ta and 99.988296(41) % for ^{181}Ta, and an absolute atomic weight for tantalum of 180.9478787(38) u (all uncertainties with k = 2, corresponds to 2 S.D.).

As a tool to trace mass fluxes of Ta and in Earth and solar system objects, **chapter III** presents an improved chemical separation protocol for silicate samples and assesses the challenges in mass spectrometry to resolve possible deviations from the natural $^{180}Ta/^{181}Ta$ ratio. Especially the isobaric interferences from abundant ^{180}Hf and potential molecular interferences on the rare isotope ^{180}Ta and interference monitor isotopes are carefully evaluated. At present, no terrestrial sample or bulk meteorite exhibits Ta isotope compositions that are resolvable from the Ta standard solution, which therefore represents the bulk silicate Earth Ta composition. Likewise, there is no evidence for Ta isotope fractionation during ore forming processes or during progressive Ta depletion in upper mantle melting processes. No isotope effects due to early solar system processes like irradiation or redox related elemental fractionation were observed in bulk meteorites. However, Ta isotope variations may be present within meteorite components as discussed in the following chapter.

In **chapter IV**, Ta isotope measurements were performed on Calcium-Aluminum-rich inclusions (CAIs) the earliest materials formed in our solar system. A diversity of isotope anomalies has been found in CAIs for a range of elements, which is attributed to excesses and depletions of distinct nucleosynthetic components synthesized at different stellar sites. So far, simple models failed to explain the complexity in nucleosynthetic anomalies observed in CAIs. In an approach to identify processes acting on CAIs, and to search for exotic nucleosynthetic anomalies from distinct stellar sources, this work combines high-precision high field strength element (HFSE) concentration and Hf, Ta, and W isotope measurements on 6 CAIs. The HFSE patterns obtained are largely condensation controlled but exhibit differences to thermodynamic predictions in elemental abundances of U and the pairs Mo-W and Nb-Ta, which may be related to inaccuracies in the canonical condensation model. Tantalum isotopes show resolvable anomalies in two of the analyzed CAIs, with ^{180}Ta being enriched relative to ^{181}Ta. If this reflects nucleosynthetic heterogeneity, it is not correlated with p-, s-, or r-process anomalies in neighboring Hf and W. Alternatively, the Ta isotope anomalies may express excess in neutrino process derived nuclides. In combination with recent findings of excesses in ^{50}V and ^{138}La and with ^{50}V, ^{138}La, and ^{180}Ta being odd-odd-isotopes occupying interstitial sites in the chart of nuclides, it is suggested that proton-irradiation from the proto-Sun might have been more efficient in altering certain isotope compositions of heavy elements in CAIs than previously thought.

Kurzzusammenfassung

Tantal ist das seltenste, stabile Element des Sonnensystems und besteht aus zwei stabilen Isotopen mit einem riesigen Unterschied der Isotopenhäufigkeiten (^{180}Ta = ~0.012 % und ^{181}Ta = ~99.988 %), was ^{180}Ta zum seltensten stabilen Nuklid des Sonnensystems macht. Tantalisotope werden zusammen mit anderen schweren Isotopen während der stellaren Nukleosynthese in Sternen am Ende ihres Lebens, sprich Roten Riesen und Supernovae, gebildet. Während ^{181}Ta durch den schnellen und langsamen Neutroneneinfangprozess produziert wird (s- und r-Prozess), wird das seltene Isotope ^{180}Ta durch den verzweigten s-Prozess und durch den Neutrino-Prozess erbrütet, der sonst nur für ein weiteres schweres Nuklid bedeutend ist (^{138}La). Tantal-180 ist das einzige bekannte stabile Nuklid in einem angeregten Kernzustand. Auf Grund dieser Eigenschaft wurde in der nuklearen Astrophysik lange nach eine geeigneten Produktionsmechanismus gesucht um die solare Häufigkeit von ^{180}Ta zu erklären. Da die frühesten Materialien des Sonnensystems dafür bekannt sind nukleosynthetische Anomalien als Zeugnis ihren stellaren Ursprungs zu besitzen, können astrophysikalische Modelle an Meteoriten verifiziert werden. Die geringe Häufigkeit von ^{180}Ta im Verhältnis zu Isotopen ähnlicher Masse, inklusive ^{181}Ta, macht die Ta-Isotopenzusammensetzung zu einem empfindlichen Tracer für den Nachweis von nuklearen Reaktionen im frühen Sonnensystem an Nachbarelementen wie Hf.

In der modernen Geochemie ist Ta ein Schlüsselelement und gehört der geochemischen Gruppe der stark geladen Ionen an (HFSE, bestehend aus Zr, Nb, Hf, Ta). Auf Grund von analytischen Schwierigkeiten in Zusammenhang mit der geringen Häufigkeit von ^{180}Ta, ist das Isotopenverhältnis von Tantal eines der am wenigsten bekannten unter den natürlich vorkommenden Elementen, weswegen natürliche Variationen bisher nie untersucht wurden. Durch die ungewöhnliche Produktion und die physikalischen Eigenschaften von ^{180}Ta könnten sich Ta-Isotopenzusammensetzungen als nützlich erweisen um nukleosynthetischen Eintrag oder Bestrahlung im frühen Sonnensystem nachzuweisen. Substantielle analytische Verbesserungen waren nötig um mögliche Variationen in Materialen des Sonnensystems nachzuweisen und die Frage nach natürlichen Variationen auf der Erde zu klären.

Nach der Einführung zur Geo- und Kosmochemie der Ta-Isotope in **Kapitel I**, wird in **Kapitel II** das analytische Protokoll für hochpräzise Ta Isotopenmessungen vorgestellt. Damit wurde ein verbessertes absolutes Ta-Isotopenverhältnis bestimmt. Mit Hilfe eines Neptune™ Multikollektor-Induktiv gekoppelten Plasma Massenspektrometers (MC-ICP-MS) und verschiedenen Verstärkern angeschlossen an die Faradaydetektoren (ein 10^{10} Ω Widerstand für ^{181}Ta, 10^{12} oder neu entwickelte 10^{13} Ω Widerstände für ^{180}Ta und den Hf Interferenzmonitor) ist es nun möglich relative Analysen von ^{180}Ta/^{181}Ta mit einer externen Reproduzierbarkeit von *ca.* ±4 ε (ε bedeutet ein Teil in 10 000) an 25

bis 100 ng Ta durchzuführen, genug für geringe Probenmengen wie Meteoriten (*z.B.* 1 g). Die 10^{13} Ω Verstärker haben sich als unerlässlich für hochpräzise Ta-Isotopenverhältnismessungen an geringen Probenmengen herausgestellt. Tailingeffekte des ^{181}Ta Ionenstrahls wurden in der Vergangenheit unterschätzt. Eine sorgfältige Untersuchung des Effekts hat einen Anteil von *ca.* 2,5% auf den derzeit akzeptierten IUPAC-Wert offenbart. Mögliche systematische Fehler in der Massendiskriminierungskorrektur sind in Anbetracht der erreichten Unsicherheit von *ca.* 0,4% auf den „wahren“ ^{180}Ta/^{181}Ta-Wert vernachlässigbar. Diese Arbeit stellt ein überarbeitetes Isotopenverhältnis von ^{180}Ta/^{181}Ta = 0.00011705(41) vor, gleichbedeutend mit ^{181}Ta/^{180}Ta = 8543(30). Dies ergibt Isotopenhäufigkeiten von 0.011704(41) % für ^{180}Ta und 99.988296(41) % für ^{181}Ta, und ein absolutes Atomgewicht für Tantal von 180.9478787(38) u (alle Unsicherheiten mit k = 2, entspricht 2 Standardabweichungen).

Als ein Werkzeug um Masseflüsse von Ta in der Erde und in Objekten Sonnensystem zu verfolgen, wird in **Kapitel III** ein verbessertes chemisches Abtrennungsverfahren für silikatische Proben vorgestellt und die Herausforderungen evaluiert um Variationen im ^{180}Ta/^{181}Ta Verhältnis aufzulösen. Besonders die isobare Interferenz des häufigen ^{180}Hf und mögliche molekulare Interferenzen auf dem seltenen ^{180}Ta und den Interferenzmonitoren werden untersucht. Bisher sind keine Ta Isotopenzusammensetzungen in terrestrischen Proben oder Gesamtgesteinsmeteorite von der Ta Standardlösung auflösbar, wodurch diese die Zusammensetzung der silikatischen Gesamterde entspricht. Ebenso gibt es keine Hinweise auf Isotopenfraktionierung während Erzbildung oder allmählicher Ta Elementverarmung des oberen Erdmantels durch Schmelzprozesse. Bestrahlung oder Redox-bedingte Elementfraktionierung im frühen Sonnensystem kann durch Ta Isotopenmessungen in Gesamtmeteoriten ausgeschlossen werden. Dennoch könnten Ta Isotopenvariationen in Komponenten von Meteoriten zu finden sein, wie im nächsten Kapitel diskutiert.

In **Kapitel IV** wurden Ta Isotopenmessungen an Kalzium-Aluminium-reichen Einschlüssen (CAIs) durchgeführt, den frühesten Materialen geformt in unserem Sonnensystem. Diverse Isotopenanomalien wurden in einer Bandbreite an Elementen in CAIs gefunden, die auf Anreicherung und Verarmung von distinkten nukleosynthetischen Anomalien, gebildet in verschiedenen stellaren Umgebungen, zurückgeführt wird. Bisher waren einfache Modelle nicht in der Lage die Komplexität von nukleosynthetischen Anomalien in CAIs zu erklären. In einem Versuch Prozesse, die auf CAIs wirken, zu identifizieren und um exotische nukleosynthetische Anomalien zu suchen, wurden kombinierten HFSE-Konzentrations- und Hf, Ta, und W Isotopenmessungen an 6 CAIs durchgeführt. Die gemessenen HFSE- Muster sind größtenteils kondensationskontrolliert aber zeigen in den Elementkonzentrationen von U und den Paaren Mo-W und Nb-Ta Unterschiede zu den thermodynamischen Vorhersagen, was auf Ungenauigkeiten im kanonischen Kondensationsmodell zurückzuführen sein könnte. Zwei der analysierten CAIs zeigen auflösbare Anomalien in Ta Isotopen,

wobei ^{180}Ta relativ zu ^{181}Ta angereichert ist. Falls dies eine nukleosynthetische Anomalie wiederspiegelt, ist diese nicht mit p-, s-, or r-Prozessanomalien in angrenzenden Elementen Hf oder W korreliert. Als Alternative könnten die Ta Isotopenanomalien Ausdruck eines Überschusses an Neutrino-Prozess abstammenden Materials sein. In Kombination mit Entdeckungen von Überschüssen an ^{50}V und ^{138}La und der Tatsache, dass ^{50}V, ^{138}La und ^{180}Ta alle ungerade-ungerade Isotope sind, die auf einem Zwischenplatz in der Nuklidkarte sitzen, wird vorgeschlagen das Protonenbestrahlung von der proto-Sonne möglicherweise die Isotopenzusammensetzung gewisser Elemente in CAIs beeinflusst haben könnte.

Table of contents

Chapter I

Introduction

1.1 The element Tantalum – chemistry and physics

Tantalum was discovered as a chemical element in 1802. The Swedish chemist Anders Gustaf Ekeberg isolated an unknown oxide from an ore found in south-east Finland (Ekeberg 1802). The same oxide was separated from yttria, a substance containing new chemical elements extracted from a mineral deposit in Sweden near the town of Ytterby, in which the heavy rare earth elements were discovered as well. Another oxide was separated from a mineral from Colombia by Charles Hatchett in 1801 (Griffith and Morris, 2003). Both oxides from Scandinavia and Colombia were first believed to contain the same element until Heinrich Rose proved their difference in 1844. For the heavier element the name Tantalum from Ekeberg was kept, while the lighter one was called Niobium (Holleman and Wiberg, 2007). The name Tantalum derives from Greek mythology. Tantalos was a king who was allowed to dine with the godfather Zeus. To challenge the Gods, he sacrificed his son and served him on the table. This did not go unaware by the Gods who punished Tantalus to eternal pain in Tartarus, the deepest part of the Underworld. Ekeberg chose the Tantalum after the proverbial “torments of Tantalus” as he was unable to dissolve the newly discovered oxide with strong acids. Niobium, which was identified as an offspring of the Ta oxide, was named after the daughter of Tantalus, Niobe (Rose 1844).

In the periodic table, Tantalum belongs to the Vanadium group and has the atomic number 73. Its chemical properties are closely related to those of Niobium, which leads to a virtually identical behavior of both elements in geological systems. This is why both elements are considered as geochemical twins. The valence state of Nb and Ta ions in Earth is 5+ and both elements have very similar ionic radii of 0.68Å and 0.69Å (Shannon, 1976). The metals are very refractory, which is also valid for the metal oxides condensing early from a hot vaporized solar nebula at the beginning of the solar system (Lodders, 2003). The elemental Ta abundance of 0.015µg/g in the solar System is constrained from the CI carbonaceous chondrites, which are the most primitive meteorites and coincide with the element abundances in the Sun’s photosphere (Palme *et al.*, 2014). This makes Tantalum the rarest element in the solar system. The concentration of Ta in the Earth’s mantle is

assumed to be to 0.043µg/g (Palme and O'Neill, 2014), while the crust is enriched to 0.7µg/g (Rudnick and Gao, 2014).

Tantalum consists of only two observationally stable isotopes, ^{180}Ta and ^{181}Ta. What makes Ta exceptional to other elements is the large spread in isotope abundances of 99.9883 % for ^{181}Ta and only 0.0117 % for the minor isotope ^{180}Ta (this thesis). Furthermore, ^{180}Ta is the only stable isotope with a nucleus in an excited state. Interestingly, its ground state decays with a half-time of 8.1 h to ^{180}Hf and ^{180}W, making the higher stability of the excited nucleus a prerequisite for its presence in nature. The large differences in isotope ratios precluded the discovery of ^{180}Ta until 1955 (White *et al.,* 1955). Since then, the official atomic weight has only been updated twice by the *International Union on Pure and Applied Chemistry* due to new isotope abundance measurements (http://www.ciaaw.org/tantalum.htm, accessed 25.11.2016).

The extreme difference in isotope abundances is very challenging for high-precision isotope ratio measurements. The low abundance of ^{180}Ta and the prediction of only minor isotope fractionation in Earth made it unlikely to find resolvable differences in natural materials. Apart from the technical aspect, Ta needs to be efficiently separated from other elements in terrestrial and extraterrestrial samples, especially from Hf and W that cause isobaric interferences in mass spectrometry. Figure 1.1 illustrates the need for an efficient chemical separation protocol and the difficulties in obtaining accurate isotope ratios with abundances of isotopes in the same mass area in primitive meteorites. Particularly ^{180}Hf has almost the same mass as ^{180}Ta and is more than 20,000 times more abundant. Thus, only a small number of scientific publications concentrated on the determination of the Ta isotope ratio in pure standard materials, while different terrestrial and extraterrestrial materials have never been analyzed for their isotope composition.

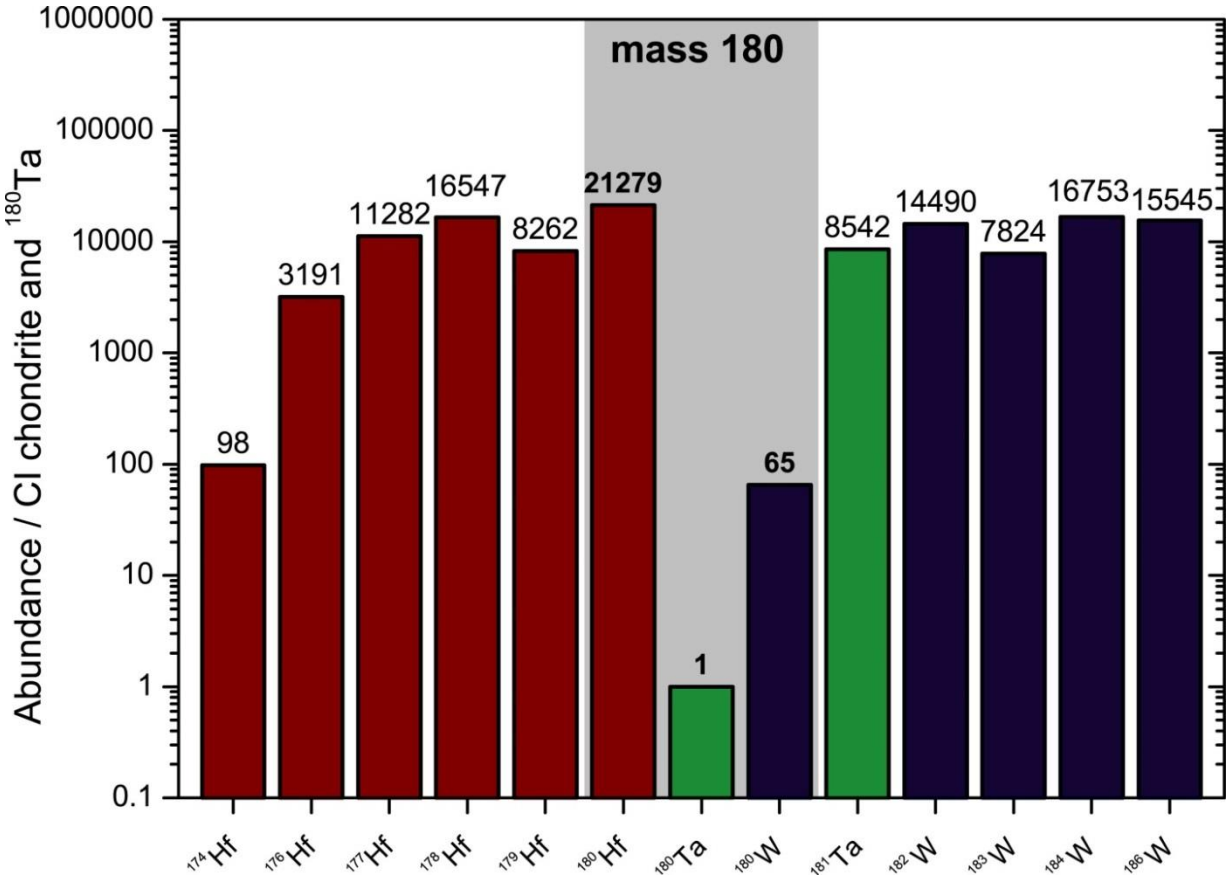

Fig. 1.1 Isotope abundances of elements Hf, Ta, and W in the solar system relative to ^{180}Ta. Tantalum-180 is orders of magnitude rarer than neighboring isotopes and suffers from isobaric interferences from ^{180}W and particularly ^{180}Hf during mass spectrometry. Note that even the small isotopes of Hf and W are by the factors of 65 and 98 more abundant (^{174}Hf and ^{180}W abundances from Peters et al. 2015). Element abundances are taken from Palme *et al.* (2014), abundances of other Hf and W isotope from the recommended IUPAC values Meija *et al.,* 2016, and Ta isotope abundances from this study.

1.2 Nucleosynthesis of heavy elements with emphasis on Tantalum isotopes

The pioneering study about the synthesis of elements in stars was published by Burbidge, Burbidge, Fowler, and Hoyle (B^2FH) in 1957. Following developments and achievements have been reviewed recently (*e.g.*, Meyer, 1994; Wallerstein *et al.,* 1997; Sneden *et al.,* 2008). The elements until the mass region of iron are produced during stellar fusion, where hydrogen is progressively transformed into heavier elements under the release of energy. Most of the nuclides beyond the Fe peak are essentially produced by two processes in massive stars: slow neutron capture (s-process) and rapid proton capture (r-process). The s-process is typical in asymptotic giant branch stars, which are stars of medium size at the end of their lives. During this (post-)red giant stage over tens of thousands of years, precursor nuclides successively capture neutrons until they reach an unstable

isotope and undergo beta-minus decay to convert to the next, proton-richer element (*e.g.*, Herwig, 2005; Bisterzo *et al.,* 2011). This way, seed nuclei from the Fe peak gradually climb up the chart of nuclides through the valley of stability until they reach Bismuth (Fig. 1.2), which is easily modeled and explains the abundance of about 50% of the material in our solar system (Arlandini *et al.,* 1999; Bisterzo *et al.,* 2014). The newly synthesized nuclides are brought to the stellar surface during dredge-up phases initiated by thermal pulses, and are then dispersed into the interstellar medium by massive stellar winds (*e.g.*, Herwig, 2005). The r-process is bound to explosive environments. Compared to the s-process, neutron densities are orders of magnitude higher to overcome beta-decay unstable isotopes and produce the neutron-rich nuclides within seconds. After the explosion event, the nuclides close to the neutron-drop line subsequently decay back towards the valley of stability. In contrast to the well-defined and modelled s-process, the site of the r-process is not unequivocally identified, yet. Most work considers core-collapse supernovae type II (cc SNe II) as the most probable site for universal r-process (*e.g.*, Woosley *et al.,* 2002; Tissot *et al.,* 2016), but there is evidence for decoupling of light and heavy r-process nuclides (Wasserburg *et al.,* 1996; Thielemann *et al.,* 2011; Tsujimoto and Shigeyama, 2014).

However, neutron capture fails to explain the p-rich nuclides to the left of the valley of stability and proton capture is rendered difficult by the Coulomb barrier. Altogether, these isotopes require a distinct production process (Burbidge *et al.*, 1957; Arnould, 1976). P-process nuclides are often one or two orders less abundant than the s- and r-process isotopes. However, this term is somewhat misleading as the different p-nuclides are produced by different nuclear reactions at different stellar sites (Rayet *et al.,* 1995; Arnould and Goriely, 2003; Rauscher *et al.,* 2013). The main site is assumed to be cc SNe II, where gamma-rays induce photo-disintegration reactions on existing s- and r-nuclides, by expelling neutrons from the nucleus (γ-process). The lighter p-process nuclides are under-produced by the γ-process relative to the solar system abundances and require an additional site of formation. Thermonuclear explosions of white dwarfs (supernovae type Ia) are able to produce the lighter p-nuclides by the rapid proton capture process (Travaglio *et al.,* 2011).

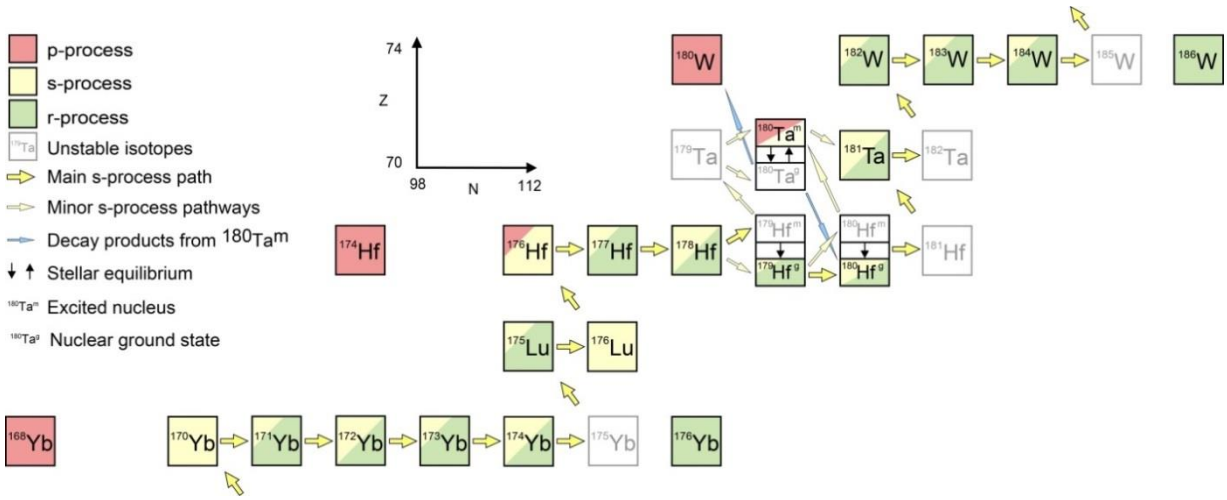

Fig. 1.2 Excerpt from the chart of nuclides illustrating the nucleosynthesis of isotopes in the mass region around Ta. The color code represents the approximate nucleosynthetic contributions. Unstable nuclides and short-lived isomeric states are greyed out. The thick yellow arrows mark the main s-process path up the chart of nuclides with the smaller ones indicating branching. The green r-process nuclides are produced from beta-minus decay of progenitor nuclides initially far to the right of the chart after the r-process event. The red p-rich nuclides cannot be produced by neutron capture reactions. Reactions involving isomeric nuclei are important for the s-process nucleosynthesis around Ta. The ground state and the excited state of ^{180}Ta are present in equilibrium under stellar conditions, whereas the ground state decays away with a half-time of 8.1 hours, as indicated by the blue arrows. Modified after Vockenhuber *et al.* (2007).

Tantalum-180 is about two orders of magnitudes rarer than the directly adjacent p-process isotopes ^{174}Hf and ^{180}W, indicating its unusual production mechanism (see Fig. 1.2). It holds a special position in nucleosynthetic models as it is both produced by branching of the main s-process path and by the special neutrino-process (ν-process; Arnould and Goriely, 2003). Intermediate mass AGB stars favor branching for the production of ^{180}Ta, where an excited state of ^{179}Hf is populated that can decay to ^{179}Ta, which then captures a neutron to produce ^{180}Ta (Fig. 1.2; Beer and Ward, 1981; Yokoi and Takahashi, 1983). A long standing problem in nuclear astrophysics was the survival of the isomeric state of ^{180}Ta as the ground state decays too fast to survive the way out of the star (*e.g.*, Belic *et al.,* 1999; Käppeler *et al.,* 2004). Newest model are able to calculate the fraction of ^{180}Ta surviving stellar conditions and could constrain the s-process ^{180}Ta abundance of the solar system to about 80% (Mohr *et al.,* 2007; Bisterzo *et al.,* 2014). The ν-process is related to cc SNe II, where the formation of the neutron star delivers the high neutrino fluence necessary to receive nuclear reactions (Woosley *et al.,* 1990; Heger *et al.,* 2005). Neutrinos interact only rarely with normal matter which is why the ν-process is only important for two nuclides heavier than iron, ^{138}La and ^{180}Ta. Tantalum-181 is a normal nuclide, produced in comparable abundances by the s- and r-process.

1.3 The building blocks of our solar system

The isotopic composition of elements in our solar system represents a blend from all nucleosynthetic processes. The nucleosynthetic products from ancient stars were ejected into the interstellar medium, mixed, evaporated and condensed, and eventually formed molecular clouds giving birth to new stars like our Sun (Hester and Desch 2005). Figure 1.3 illustrates the building blocks and processes acting on material prior to assembly of the solar system. Evidence of the inheritance of interstellar material in the solar system was found in presolar grains in primitive meteorites (Anders and Zinner, 1993). It is however open, if and to what extent the solar nebula was influenced by later input or inner disk processing to alter the isotope compositions of the different elements.

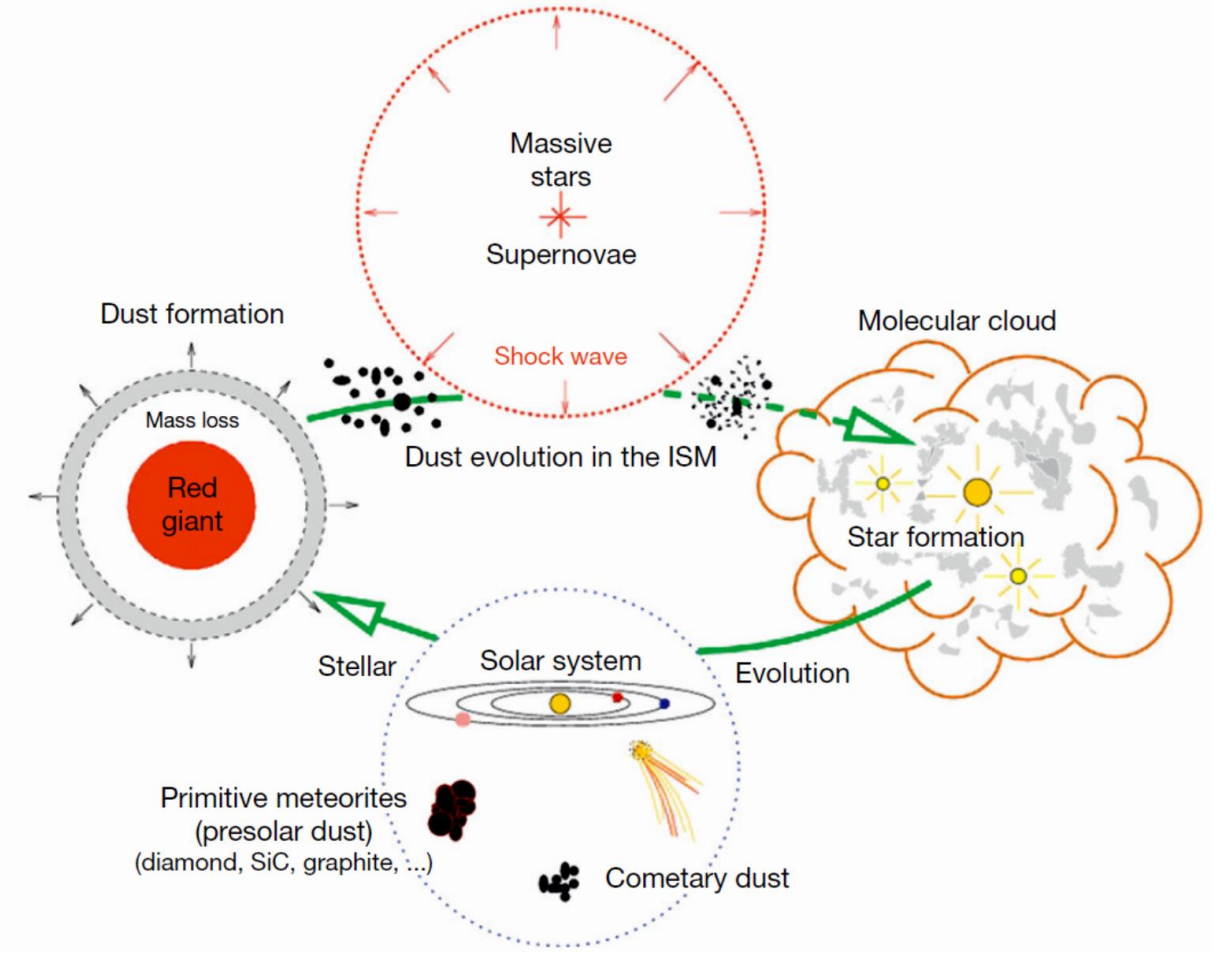

Fig. 1.3 The solar system put in context of the galactic chemical evolution. Red giants and supernovae produce new nuclides through their different nucleosynthetic reaction networks and pollute the interstellar medium (ISM) with freshly synthesized nuclides. Being part of the ISM, the dust is further processed by high-energetic particles, eventually forming molecular clouds. In those star factories, stellar systems like our solar system can form. Comets and primitive meteorites carry the witnesses of those processes with presolar grains. The Figure is taken from Jones (2004).

Refractory materials in meteorites, so called Ca-Al-rich inclusions (CAIs), bear evidence for different components in the early solar system. Nucleosynthetic anomalies in heavier elements are known in CAIs since the 1970s (McCulloch and Wasserburg, 1978a; McCulloch and Wasserburg, 1978b) and could be related to distinct nucleosynthetic processes (see Dauphas and Schauble, 2016 and references therein for recent review). Several theories exist about the origin of these isotope variations. To some extent, they might be an expression of an initial heterogeneity in the solar nebula during formation of earliest condensates (*e.g.*, Kööp *et al.,* 2016). A further model invokes the addition of material through a nearby supernova explosion or stellar winds by a massive star in the star-forming cluster from which our Sun has originated from, which might have triggered the collapse of the molecular cloud to form the solar system (Cameron and Truran, 1977; Gounelle and Meynet, 2012). A last model assumes initial physical homogeneity of presolar carrier phases in the molecular cloud, which then got processed in the early solar system to different extents, causing formation of isotopically distinct reservoirs that are necessary to explain large scale differences in meteorite parent bodies (Dauphas *et al.,* 2002; Trinquier *et al.,* 2009). In addition to nucleosynthetic anomalies, the presence of extinct ^{10}Be in CAIs hints to spallation reaction induced from proton-irradiation from the active proto-Sun (McKeegan, 2000). Presently, the influence of irradiation on heavier isotopes is debated (Gounelle *et al.,* 2001; Desch *et al.,* 2010), but odd-odd nuclides ^{50}V and ^{138}La were found to exhibit positive isotope anomalies in CAIs (Shen and Lee, 2003; Sossi *et al.* 2016).

Other heavy elements like Zr, Hf and W are known to exhibit nucleosynthetic anomalies in the earliest solar system (Burkhardt *et al.,* 2008; Sprung *et al.,* 2010; Akram *et al.,* 2013; Kruijer *et al.,* 2014; Peters *et al.*, 2016). In this context, it is likely to assume variations in Ta isotopes as well, which might be a valuable tool to trace exact nucleosynthetic contributions in connection with Hf and W isotope data. Furthermore, Ta isotopes might be a sensitive tracer of early irradiation in the solar system as ^{180}Ta would show significant ingrowth due to its low abundance.

1.4 Geochemistry of Tantalum

The localities of the first recognized occurrences of Ta ores in Sweden and Finland are prime examples for the geochemical affinity of Ta. Both ores stem from pegmatites and represent late-stage evolved granitic systems, where incompatible elements are concentrated in the last magmatic phase. This contrasts to meteorites, where the primitive chondrites have refractory element contents representing the solar abundance with Ta being the rarest element in the solar system. Earth, however, is a differentiated planet with core, mantle and crust, and constant recycling by plate tectonics, leading to significant re-distribution of Ta.

As a high-field strength element (HFSE), Ta is highly incompatible in most rocks and always tends to enter into a silicate melt. This results in a progressive depletion of the Earth's mantle in Ta and a concentration of Ta in the crust over geological time. The high charge combined with their small size renders Ta ions unable to fit into crystal lattices of most silicate minerals. Small concentrations of Ta can be incorporated in amphiboles or accessory oxide minerals in less evolved magmas like basalts or andesite (*e.g.*, Brenan *et al.,* 1994; Ionov and Hofmann, 1995). Tantalum generally becomes enriched in the most fractionated melts and crystallizes its own minerals. The mineralization of Tantalum cannot be discussed without mentioning Niobium as both elements are geochemical twins and are typically incorporated in the same minerals. Therefore, Ta and Nb form solid solution series in their own group of minerals. Typical Tantalum ore minerals are columbite [$(Mn,Fe)(Nb,Ta)_2O_6$] and tantalite [$(Mn,Fe)(Ta,Nb)_2O_6$] series, which are colloquially known as Coltan (Dill, 2010). Another important ore mineral is the microlite group [$(Na,Ca)_2Ta_2O_6(O,OH,F)$], which exhibits a solid solution with the Nb-rich pyrochlore group (Dill, 2010). Apart from the aforementioned minerals associated with granites and pegmatites, carbonatites are highly enriched in Nb and Ta (Chakhmouradian, 2006).

The elemental ratio between Nb and Ta is widely used as a tracer for geochemical processes acting at scales of magmatic systems, oceans, or planets (*e.g.*, Jochum *et al.*, 1986; Green and Pearson, 1987; Barth *et al.,* 2000; Münker *et al.,* 2003; Weyer *et al.,* 2003; Schmidt *et al.,* 2014). Offsets from the chondritic ratio of *ca.* 19.9 (Münker *et al.,* 2003) are the result of small geochemical fractionation between the two elements. However, the magnitude of fractionation is normally limited due to their extremely similar geochemical characteristics. Stable isotope fractionation of Ta in combination with characteristic Nb and Ta elemental concentrations might indicate distinct geological or cosmochemical processes being in operation. Measurements of rocks with various Nb/Ta ratios from different settings should provide endmember-constraints on potential Ta isotope fractionation on Earth and may offer new possibilities for application in geoscientific problems.

1.5 Chapter overview

This thesis gives an extensive overview on the isotopic inventory of Ta in materials from Earth and the early solar system. **Chapter II** focusses on the development of the mass spectrometric method and discusses the advantage of newly developed $10^{13}\Omega$ resistor Faraday detector amplifiers for high-precision measurements of small sample sizes as necessary for Ta isotope measurements in meteorites. Furthermore, after thorough assessment of systematic errors in Ta isotope measurements, the presently accepted natural Ta isotope abundances in standard materials are re-evaluated.

Chapter III introduces the chemical purification protocol essential for accurate and precise Ta isotope measurements of natural materials and challenges in Ta isotope measurements of natural samples are discussed. Progressive depletion and enrichment in Earth reservoirs, differences in complexation of Ta in melts or low-temperature elemental re-distribution could give rise to stable isotope fractionation. A suite of rocks from a range of geodynamic settings are therefore analyzed for their Ta isotope compositions. No Ta isotope variations were found on Earth. Furthermore, measurements of Ta isotopes in bulk meteorites revealed no larger scale isotope variability in the solar system. This information is necessary to interpret isotope anomalies in meteorite components.

In **Chapter IV**, Ta isotopes are tested as a new tool in cosmochemistry. Combined HFSE concentration and Hf-Ta-W isotope analyses are performed to elucidate the processing of CAIs in the early solar system. Tantalum isotope anomalies were identified in two CAIs. The differences in Ta isotopes are discussed in context with recent isotope data and astrophysical models. Nucleosynthetic isotope anomalies or early irradiation are inferred as possible reason of Ta isotope variations in early solar system materials.

Chapter II

Tantalum isotope ratio measurements and isotope abundances determined by MC-ICP-MS using amplifiers equipped with 10^{10}, 10^{12} and 10^{13} Ohm resistors

2.1 INTRODUCTION

Tantalum is the rarest chemical element in the solar system. It consists of two isotopes with the major isotope ^{181}Ta accounting for 99.98799(8) % of its molar abundance, according to current IUPAC recommendations (Meija *et al.*, 2016). In contrast, the reported relative abundance of ^{180}Ta equals only 0.01201(8) % (Meija *et al.*, 2016), making ^{180}Ta the rarest stable nuclide in the solar system, which is why ^{180}Ta was not discovered until 1955 (White *et al.*, 1955). Furthermore, ^{180}Ta is the only observationally stable isotope present as an excited nuclear isomer. In its ground state, ^{180}Ta decays to ^{180}Hf and ^{180}W with a half-life of only 8 hours (*e.g.*, de Laeter and Bukilic, 2005; Hult *et al.*, 2006). The extreme difference in isotope abundances of a factor of more than 8000 makes the precise and accurate determination of Ta isotope ratios by mass spectrometry challenging. Using a multi-collector ICP-MS system (MC-ICP-MS), we partially overcome the large difference in isotope abundances by collecting a large ion beam for ^{181}Ta in a Faraday cup with 10^{10} Ω resistor in the amplifier feedback loop (up to $5 \cdot 10^{-9}$ A, equivalent to 500 V if common 10^{11} Ω resistors would be applied), while collecting the low abundance isotope ^{180}Ta and isobaric interference monitors with Faraday amplifiers with high-Ohm resistors.

The isotope composition of Ta is of particular interest because it may vary in extraterrestrial materials. For many elements technical advances in mass spectrometry over the past 15 years (e.g., Wieser and Schwieters, 2005) made it possible to resolve small isotope anomalies at the sub-per mil level in solar system materials relative to Earth, *e.g.*, Zr (Schönbächler *et al.,* 2003), Mo (Dauphas *et al.,* 2002; Yin *et al.,* 2002), Ru (Dauphas *et al.,* 2004), Ba (Hidaka *et al.,* 2003), Nd (Boyet and Carlson, 2005; Andreasen and Sharma 2006) or Sm (Andreasen and Sharma 2006). These so-called nucleosynthetic isotope anomalies give testimony to the early evolution of the solar system, such as

thermal processing of presolar grains from other stars (*e.g.*, Huss *et al.,* 2003; Trinquier *et al.,* 2009) or later injection of material from nearby star explosions into the nascent solar system (Cameron and Truran, 1977). Additionally, the Ta isotope compositions of natural samples may show variations due to mass-dependent, nuclear volume dependent or kinetic stable isotope fractionation during geological processes. Hence, sufficiently precise measurements protocols for Ta isotopes in order to identify such effects are required.

Previous Ta isotope analyses by MC-ICP-MS and thermal ionisation mass spectrometry (TIMS) employed Faraday collectors with 10^{11} Ω resistors in the amplifier feedback loop. The electronic noise contribution from this conventional setup can be reduced by about a factor of three by the use of recently developed amplifiers with 10^{12} Ω resistors (Makishima and Nakamura, 2010; Koornneef et al. 2013). Amplifiers with 10^{12} Ω resistors are used in TIMS and MC-ICP-MS for three main purposes: 1) Measurement of small sample sizes (Makishima and Nakamura, 2010; Liu and Pearson, 2014; Sarkar *et al.,* 2015), 2) precise monitoring of interfering elements (Schiller *et al.,* 2012; Schulz *et al.,* 2013; Peters *et al.,* 2014; Peters *et al.,* 2014) and 3) combined application with 10^{10}, 10^{11}, and 10^{12} Ω resistors to account for largely different ion beam intensities of one element (Wielandt and Bizzarro, 2011; Naumenko *et al.,* 2013; Peters *et al.,* 2015). The advent of newly developed amplifiers equipped with 10^{13} Ω resistors further reduced physical limitations by, in theory, increasing the signal-to-noise ratio by a factor of √100 compared to an amplifier equipped with a 10^{11} Ω resistor (Koornneef *et al.,* 2014, Koornneef *et al.,* 2015, Klaver *et al.,* 2016). The precision of a $4 \cdot 10^{-14}$ A ion current (equivalent to 4 mV with 10^{11} Ω resistors) on ^{143}Nd was shown to improve by factors of 2 and 4 compared to 10^{12} and 10^{11} Ω amplifiers, respectively (Koornneef *et al.,* 2014). At count rates above $2 \cdot 10^{4}$ cps (= 0.32 mV), 10^{13} Ω resistors even proved to be superior to secondary electron multipliers (Koornneef *et al.,* 2014). Collectively, these technical improvements set the stage to search for small differences in Ta isotope ratios in geological and meteoritic materials.

So far, only Kimura *et al.* (2016) documented the applicability of amplifiers equipped with 10^{13} Ω resistors in MC-ICP-MS. Here, we also compare the performance of 10^{13} Ω resistors with that of 10^{12} amplifiers. We extend the application of 10^{13} Ω resistors to precise monitoring of strongly interfering elements and to measuring very low abundance isotopes that limit the precision of isotope ratio measurements. A protocol is presented here for high-precision Ta isotope ratio measurements, with an emphasis on the application to extraterrestrial samples of limited size. This protocol furthermore allows a re-evaluation of the terrestrial ^{180}Ta/^{181}Ta isotope ratio that is recommended by IUPAC (0.0001201(6); de Laeter and Bukilic, 2005) and by Weyer *et al.* (0.0001198(6); 2002). It was previously shown that abundance sensitivity plays a critical role in MC-ICP-MS for the determination of accurate isotope ratios for heavy elements (Thirlwall 2001). In fact, it was observed that ^{181}Ta can induce significant peak tailing over up to 3 u distance from the centre

(Thirlwall and Anczkiewicz 2004). The two studies that previously presented Ta isotope data discuss this abundance sensitivity effect. While de Laeter and Bukilic (2005) neglected tailing effects, Weyer *et al.* (2002) identified abundance sensitivity as the limiting factor for accurate Ta isotope ratio measurements. The latter study consequently suggested a lowermost value for $^{180}Ta/^{181}Ta$ = 0.000115. In the present study, we evaluate the effect of varying pressure at the high-vacuum end of the instrument on the abundance sensitivity and measured isotope ratios. We then present an offline tailing correction, suggesting that the tailing of ^{181}Ta on ^{180}Ta has been underestimated in the past. A significantly lower $^{180}Ta/^{181}Ta$ isotope ratio and, therefore, a lower absolute isotope abundance of ^{180}Ta are proposed.

2.2 EXPERIMENTAL

Measurements were conducted on a Thermo Scientific Neptune™ MC-ICP-MS instrument (upgraded with a Plus interface) at facilities at the joint Cologne-Bonn MC-ICP-MS laboratory, Germany, and on a Thermo Scientific Neptune Plus™ at Bremen, Germany, from February 2013 to March 2016. The data were obtained in 12 individual sessions consisting of 22 measurement sequences.

2.2.1 General set-up and data evaluation

Traditionally, many users of mass spectrometers discuss ion beam intensities in voltages measured across the resistor, rather than ion currents. However, measured voltages change with the resistor value according to Ohm's law. In order to compare the signal intensities we report voltages as V*, meaning the signal intensity as if a 10^{11} Ω resistor were in use, which is in the same manner as the instrument software reports ion beam signal intensities. Both instruments were operated with a Jet interface (Jet sampler cone, X-skimmer cone, and On-Tool booster pump) and a Cetac ARIDUS II™ desolvating system. The PFA nebulisers provide uptake rates of *ca.* 100 µl/min, using 0.56 M HNO_3/0.24 M HF as measurement solution. Typical operating conditions are given in Table 2.1 for the instruments at Cologne-Bonn and Bremen with a single analysis comprising of 120 cycles of 4.2 s integration time or 60 cycles of 8.4 s integration time to account for settling delays of the high-Ohm resistors.

Table 2.1 Typical MC-ICP-MS instrument operating conditions during Ta isotope ratio measurements

	Cologne-Bonn	Bremen
Operation power [W]	1300	1300
Sample gas flow rate [l/min]	0.9	0.6 – 0.8
Auxiliary gas flow rate [l/min]	0.7	0.8
Cooling gas flow rate [l/min]	15	16.3
Fore vacuum pressure [mbar]	$< 5 \cdot 10^{-3}$	$< 1.3 \cdot 10^{-3}$
High vacuum pressure [mbar]	$< 1.5 \cdot 10^{-7}$	$< 3 \cdot 10^{-7}$
Analyser pressure [mbar]	$0.8 – 3.6 \cdot 10^{-8}$	$1.2 – 2.4 \cdot 10^{-8}$
Nebuliser	100 µl/min MicroFlow PFA	100 µl/min MicroFlow PFA
ARIDUS II™ sweep gas flow rate [Ar, l/min]	5.2	4 – 5
ARIDUS II™ nitrogen gas flow rate [l/min]	0.05	0.05

Tantalum consumption for one measurement at Bremen was ~25 ng leading to a $4.5 \cdot 10^{-10}$ A ion current on ^{181}Ta for a 30 ng/g standard solution (corresponds to 45V*). At Cologne-Bonn, ion currents of around $2 \cdot 10^{-9}$ A were achieved for a 100 ng/g solutions, consuming ~90 ng Ta. This translates to 1600–1900 V* per µg/g Ta at both instruments. Mass bias correction was typically performed externally using doped Yb. For this purpose, the Alfa Aesar Specpure® plasma Yb standard solution (LOT 71-064667L) was admixed to the Ta solutions at a concentration of *ca.* 8 ng/g, resulting in an ion current of *ca.* $6 \cdot 10^{-11}$ A on the largest isotope ^{174}Yb (isotope abundance of ~32 %). External mass bias correction based on Re isotopes (Alfa Aesar Specpure® LOT 71-071361B) was also tested (chapter 2.2.2). The Ta standard solution that was predominantly used during this project had previously been prepared from AMES Ta-metal at Münster (Weyer *et al.*, 2002). Additionally, the Alfa Aesar Specpure® Ta plasma standard solution (LOT 15024103) and Merck Certipur® Ta ICP standard solution (LOT HC56783956) were measured for comparison and to test for potential stable isotope fractionation during the industrial Ta purification process.

Gain calibration for the Faraday amplifier was performed using the software operated standard procedure where a 33.3 fA reference current (equal to 3.33 V*) is consecutively applied to all amplifiers, except for those equipped with 10^{13} Ω resistors as those would saturate at signals >0.5 V*. The 10^{13} Ω amplifier cross-calibration was then conducted using a protocol comparable to that described by Kimura *et al*. (2016). In this case, separate 30-minute measurements were made with a

Nd solution (here: Merck Certipur® ICP standard solution LOT HC077146), first with the electronically calibrated 10^{11} Ω amplifiers with *ca.* 140 mV* on ^{148}Nd using a 10 ng/g solution in wet plasma. The amplifiers connected to the Faraday cups that collect ^{145}Nd, ^{148}Nd, and ^{150}Nd were then switched to 10^{13} Ω amplifiers, while keeping the ^{144}Nd ion beam in a Faraday cup connected to a gain calibrated 10^{11} Ω amplifier. The tuning parameters were kept unchanged during the 20 minutes baseline measurement and the subsequent repeated measurement of the Nd standard. The gains for the 10^{13} Ω amplifiers were calculated from the results from the two measurements and were manually entered in the executive table of the instrument software. Hence, no assumptions about true isotope ratios and accuracy of mass discrimination laws needed to be made during this gain calibration procedure, as the 10^{13} resistor amplifier gains are calculated from the ratios in comparison to the same isotope ratios previously measured with gain corrected 10^{11} Ω resistors. The three isotopes of Nd measured here are of comparable abundance and make Nd an ideal element for cross calibration of up to three 10^{13} Ω amplifiers. Kimura *et al.* (2016) applied an inter-calibration approach by cycling the attached amplifiers to each Nd isotope and calculate the gains on the amplifiers with a solver function in Excel (Kimura *et al.,* 2016). Our approach could be simplified as the normalising isotope ^{144}Nd was always measured with a previously gain corrected 10^{11} Ω resistor. Earlier work applied measurements of secondary standards to monitor the stability of the gain calibration. This is not necessary, as the amplifiers proved to be stable enough on timescales relevant for typical lengths of MC-ICP-MS analytical sessions (Koornneef *et al.,* 2014).

The typical repeatability (corresponds to internal precision in the geochemical literature) of the Nd measurements with 10^{13} Ω amplifiers is better than 80 ppm (2 S.E.) for ^{148}Nd/^{144}Nd. Repeated measurements using this protocol yield an intermediate precision (corresponds to external reproducibility in geochemical publications) of better than 82 ppm for ^{148}Nd/^{144}Nd (2 S.D., n = 10). The electronic cross calibration of the standard 10^{11} Ω amplifiers using a 33.3 fA reference current is typically reproducible to better than 16 ppm (2 S.D.), which results in a combined uncertainty of the cross calibration of *ca.* 1 ε (2 S.D.), in accord with previously reported gain precision for 10^{13}Ω amplifiers (Klaver *et al.*, 2016). This uncertainty cancels out for measurements relative to a standard.

The baseline was measured prior to each measurement session with a deflected ion beam over 1000 cycles of 1.05 s each. Baseline measurements were always performed more than 30 minutes after the gain calibration to allow settling of our early model 10^{12} Ω resistors towards baseline levels. Low intensity ^{180}Ta and the critical interference monitor ^{178}Hf were collected in Faraday cups attached to amplifiers with 10^{12} Ω resistors at Cologne-Bonn and to amplifiers with 10^{13} Ω resistors at Bremen (Table 2.2). In order to improve the counting statistics and the signal to noise ratio for the low-abundance isotope ^{180}Ta, large signals had to be measured for ^{181}Ta, using an amplifier with a 10^{10} Ω resistor at Cologne-Bonn. Additional ion beams were collected with amplifiers

with 10^{11} Ω resistors (Table 2.2). Typical signal voltages on ^{181}Ta were 45 V* at Bremen and 150 - 200 V* at Cologne-Bonn to achieve sufficient precision with *ca.* 5 and 20 mV* on ^{180}Ta, respectively.

Table 2.2 Collector set-ups and assigned amplifiers with indicated resistors. The element used for mass bias correction and the resulting amplifier configuration is given for each facility. Elemental isobaric interferences are shown in brackets. Resistors other than 10^{11} Ω are marked in bold.

Configuration	L4	L3	L2	L1	C	H1	H2	H3	H4
Yb-based mass bias correction	^{171}Yb	^{172}Yb	^{173}Yb	^{174}Yb (^{174}Hf)	^{178}Hf	^{179}Hf	**^{180}Ta** (^{180}Hf) (^{180}W)	**^{181}Ta**	^{183}W
Amplifier Cologne-Bonn	10^{11}	10^{11}	10^{11}	10^{11}	**10^{12}**	10^{11}	**10^{12}**	**10^{10}**	10^{11}
Amplifier Bremen	10^{11}	10^{11}	10^{11}	10^{11}	**10^{13}**	**10^{12}**	**10^{13}**	10^{11}	**10^{12}**
Re-based mass bias correction	^{178}Hf	^{179}Hf	**^{180}Ta** (^{180}Hf) (^{180}W)	**^{181}Ta**	^{183}W	^{184}W (^{184}Os)	^{185}Re	^{187}Re (^{187}Os)	^{189}Os
Amplifier Cologne Bonn	**10^{12}**	10^{11}	**10^{12}**	**10^{10}**	10^{11}	10^{11}	10^{11}	10^{11}	10^{11}

For comparison, all data were processed offline and online. Instrumental mass bias was corrected externally based on the measured isotope composition of Yb between masses 171 and 174, using the exponential law (also known as Russell's law; Russell et al., 1978) and the Yb ratios recommended by Albalat *et al.*, (2012) The latter data agreed better with our mass discrimination corrected data than the IUPAC recommended values from de Laeter and Bukilic (de Laeter and Bukilic, 2006). All Ta isotope data are reported relative either to ^{173}Yb/^{171}Yb = 1.12489 (Yb-based mass bias correction (Albalat *et al.*, 2012) or ^{187}Re/^{185}Re = 1.67394 (Re-based mass bias correction (Meija et al., 2016). Elemental isobaric interferences were corrected based on ^{180}Hf/^{178}Hf = 1.2863 and ^{180}W/^{183}W = 0.008304, which represent our long-term measured values (Peters *et al.*, 2015). In particular the very large isobaric interference from ^{180}Hf (relative abundance 35.08 %) on ^{180}Ta required careful correction, even in the case of the purest standard solutions. In terms of mass fractionation, elements of similar mass such as Yb, Hf, Ta, W, and Re transmitted through the mass spectrometer will be biased by very similar extents. Therefore, for the correction of ^{180}Hf and ^{180}W interferences on ^{180}Ta, the literature ^{180}Hf/^{178}Hf and ^{180}W/^{183}W ratios (Peters *et al.*, 2015) were artificially biased using the exponential law and the fractionation factor determined from ^{173}Yb/^{171}Yb

or $^{187}Re/^{185}Re$. Regular tests with Hf-doped Ta standard solutions confirmed the robustness of the interference correction over time. The measured $^{178}Hf/^{181}Ta$ of the pure standard solutions were $<1 \cdot 10^{-6}$, i.e., below the threshold of $^{178}Hf/^{181}Ta = 8 \cdot 10^{-6}$ at which the correction starts to introduce significant biases. The minor interference of ^{174}Hf (~0.16 %) on ^{174}Yb does not result in significant uncertainty propagation into the external mass bias correction, nor does it affect the absolute mass-bias corrected Ta isotope ratios, because Hf is virtually absent in the Ta standard solutions. The same applies for the interference of ^{187}Os on ^{187}Re if doped Re is used for external normalisation.

Measured data are partly presented as the deviation from a reference standard using the epsilon notation (parts per ten thousand):

$$\varepsilon^{180}Ta = \left[\frac{(^{180}Ta/^{181}Ta)_{individual\ standard}}{(^{180}Ta/^{181}Ta)_{reference\ standard}} - 1\right] \times 10^4 \quad (2.1)$$

This notation is commonly preferred over absolute values because relative measurements achieve better precision than absolute analyses. This is mainly due to changes in the abundance sensitivity of the instrument, which result in a drift of the measured isotope ratios that is specific to each analytical session. This drift can be corrected by bracketing measurements with the adjacent standards or by mathematical regression through the data. Henceforth, the quoted values for intermediate precision correspond to the 2 times standard deviation of the measured Ta isotope ratios relative to a linear or sometimes polynomial fit through the data for standards of an analytical session.

2.2.2 Correction of instrumental mass discrimination

In inductively coupled plasma mass spectrometry, heavy isotopes are preferentially transmitted. For heavy elements like Ta, this mass bias typically increases heavy over light isotopes by about 1% u^{-1} (*e.g.*, Maréchal *et al.*, 1999). Addition of another element of similar mass, e.g., Yb to the Ta solutions, allows monitoring of changes in mass bias during the measurement session (*e.g.*, Longerich *et al.*, 1987). This external mass discrimination correction often allows for more precise relative isotope ratio measurements and also improves the accuracy of the isotope ratio measurement. In detail, however, this correction depends on the accuracy of isotope composition assumed for the admixed element solution and suffers from differences in the mass bias behaviour between the two elements. These differences in mass bias behaviour between two elements depend on tuning parameters and cones and are commonly observed between measurement sessions (Maréchal *et al.*, 1999; Albarède *et al.*, 2004). Here, the Ta isotope ratio data were corrected for instrumental mass discrimination based on the concurrent measurement of Yb and in some cases Re isotope ratios. As Yb has more than two isotopes, its isotope composition enables assessment of

polyatomic interferences on specific isotopes. Furthermore, Yb-based mass bias correction allows the comparison of results that are calculated with different Yb isotope ratios.

The mass bias corrected $^{180}Ta/^{181}Ta$ based on different Yb ratios are indistinguishable within repeatability (2 S.E.). Neither, the use of conventional (as opposed to "Jet") sampling cones, nor variations in Yb/Ta of the measurement solution affected the mass fractionation corrected Ta isotope ratios significantly. Altogether, Yb isotopes therefore seem to be robust monitors for the instrumental mass bias drift of Ta isotopes. To verify the accuracy of Yb-normalised data, we also tested the correction for the instrumental mass bias by using admixed Re. Rhenium exhibits advantages as well as disadvantages over Yb as a doping element for mass bias correction. On the one hand, Re allows for better Hf interference correction for up to $5 \cdot 10^{-5}$ of $^{178}Hf/^{181}Ta$, more than five times higher than possible using the Yb-doping protocol. This was also evident from somewhat smaller repeatability of single Ta measurements which may be a result of similar sampling of Re, Hf, and Ta ions from the plasma, as they all exhibit more similar first ionisation potentials compared to Yb. On the other hand, we observed that Re sometimes fails to provide an accurate external mass bias correction. This is assumed to stem from occasional isotope fractionation effects of Re inside the Aridus desolvating system, where Re seems to get lost through the membrane at higher temperatures, which then results in outliers in the Ta standard solution data. Similar observations were made for tungsten stable isotope analyses when using Re for external mass bias correction (Breton and Quitté, 2014). With the exception of occasional outliers, the Re-normalised Ta isotope compositions overlap with the Yb-normalised data within intermediate precision (2.S.D.). As the behaviour of Yb during measurements was more reliable compared to Re and the measured Ta standard solutions are pure enough in Hf, we preferred using Yb-normalisation to correct for instrumental mass bias.

Notably, all mass bias corrected $^{180}Ta/^{181}Ta$ ratios are approximately 30 ε higher (corrected relative to $^{173}Yb/^{171}Yb$) if the recently proposed Yb isotope abundances by Wang *et al.* (2015) are considered for the mass bias correction. We prefer the Yb isotope abundances reported by Albalat *et al.* (2012), because use of the Yb isotope abundances by Wang *et al.* (2015) as a means for mass bias correction would lead to a mismatch between the Re- and Yb-normalised Ta isotope compositions (chapter 2.3.4). Furthermore, Albalat *et al.* (2012) give the Yb isotope composition of a plasma standard from Alfa Aesar, and we used a similar Yb standard solution in this study. Wang *et al.* (2015) compiled different standard solutions, which might display different isotope fractionation either by industrial processing or naturally, as there exists a stable Yb isotope variability of more than 0.5 per mil on Earth (Albalat *et al.,*(2012). A strong argument for the Albalat *et al.* (2012) data is consistency, yielding Ta ratios within 1 ε after mass bias correction with different Yb ratios. In contrast, when using the Wang *et al.* (2015) data, $^{180}Ta/^{181}Ta$ ratios of the same measurement deviate by up to 20 ε,

depending on the Yb ratio used for normalisation. Despite the inconsistency in published Yb isotope data, other factors than mass discrimination correction, e.g., the correction of the ^{180}Hf interference and especially the abundance sensitivity affect the accuracy of the Ta isotope ratio measured more prominently.

2.2.3 Abundance sensitivity in ^{180}Ta/^{181}Ta measurements

Accurate Ta isotope ratio measurements require an assessment of abundance sensitivity effects from ^{181}Ta on the far rarer ^{180}Ta (Weyer *et al.*, 2002; de Later and Bukilic, 2005). For the Neptune Plus MC-ICP-MS, the abundance sensitivity on ^{237}U in the presence of a strong ^{238}U beam is specified to be below 5 ppm (Thermo Fisher Scientific, 2010). The abundance sensitivity at one u below ^{181}Ta is typically between 1.9 to 3.1 ppm at both instruments at Cologne-Bonn and Bremen, which translates into an additional signal contribution onto ^{180}Ta of approximately 2 %. Tailing of ^{181}Ta on the low-mass side can also affect the signals on ^{179}Hf and ^{178}Hf. We observed that interference monitor ^{178}Hf was compromised at ion currents >2 · 10^{-9} A on ^{181}Ta (= 200 V*). An upper limit of 200 V* on ^{181}Ta was therefore set during the course of our study. Lower ^{181}Ta beam intensities used at Bremen (<45 V*) did not result in significant tailing effects on ^{178}Hf and potential error contributions on ^{180}Ta/^{181}Ta. Abundance sensitivity effects were also observed on the high-mass side of ^{181}Ta. The tail contribution from ^{181}Ta on the ^{180}W interference monitor ^{183}W is *ca.* 0.2 ppm and translates into an additional correction of 0.2 ε on the Ta isotope ratio, if compared to correction with non-influenced ^{184}W as interference monitor. This is well within the repeatability (2 S.E.) of ^{180}Ta/^{181}Ta ratios and negligible within the framework of our study.

In order to monitor the tail from ^{181}Ta on adjacent masses, the mass set in the centre cup was increased by 0.5 u immediately before and after each sequence of measurements. The peak centre routine was only executed before the measurements to avoid observed shifts of several ε in measured Ta isotope ratios during the sequence due to a shifted tail caused by a changed mass calibration. The intensities on masses 178.45, 179.45 and 180.45 during aspiration of a high concentrated standard solution were recorded with 60 cycles of 4.2 s each and an empirical equation was fitted for the mass region from 177 to 180.7 (Fig. 2.1) in order to evaluate the tailing effect on full masses at 177.944, 178.946 and 179.947 u:

$$S_{tail} = a_1 * e^{\frac{m-178.45}{a_2}} + a_3, \quad (2.2)$$

where S_{tail} equals the tail contribution to the signal in V* on mass m. The best-fit parameters a_1, a_2, a_3 were obtained from the data measured between the peaks at the beginning and end of every measurement session. A tailing ratio was calculated by dividing S_{tail} by the ^{181}Ta intensity

corresponding to the tail measurement, which then was subtracted from the measured mass 180/181 ratios of samples and standards during the sequence. Tail corrections were always calculated offline for each integration cycle before applying the mass bias correction. For the correction of our data, it was assumed that the drift in abundance sensitivity during a measurement sequence was linear between the two tailing measurements.

Typical values are $a_1 \approx 3.5 \cdot 10^{-6}$, $a_2 \approx 0.44$, and $a_3 \approx 1 \cdot 10^{-5}$ for abundance sensitivity measured at *ca.* 45 V on ^{181}Ta for both instruments. The same exponential fit was previously applied to correct tailing from ^{140}Ce on minor Ce isotopes in TIMS (Willbold 2007). The tailing of ^{181}Ta calculated from eq. 2.2 fits the measured tail extremely well (Fig. 2.1). Typical drift of abundance sensitivity at mass 180 was below 0.3 ppm throughout an analytical session, corresponding to a maximum shift of 25 ε in ^{180}Ta/^{181}Ta (discussed in chapter 2.3.3).

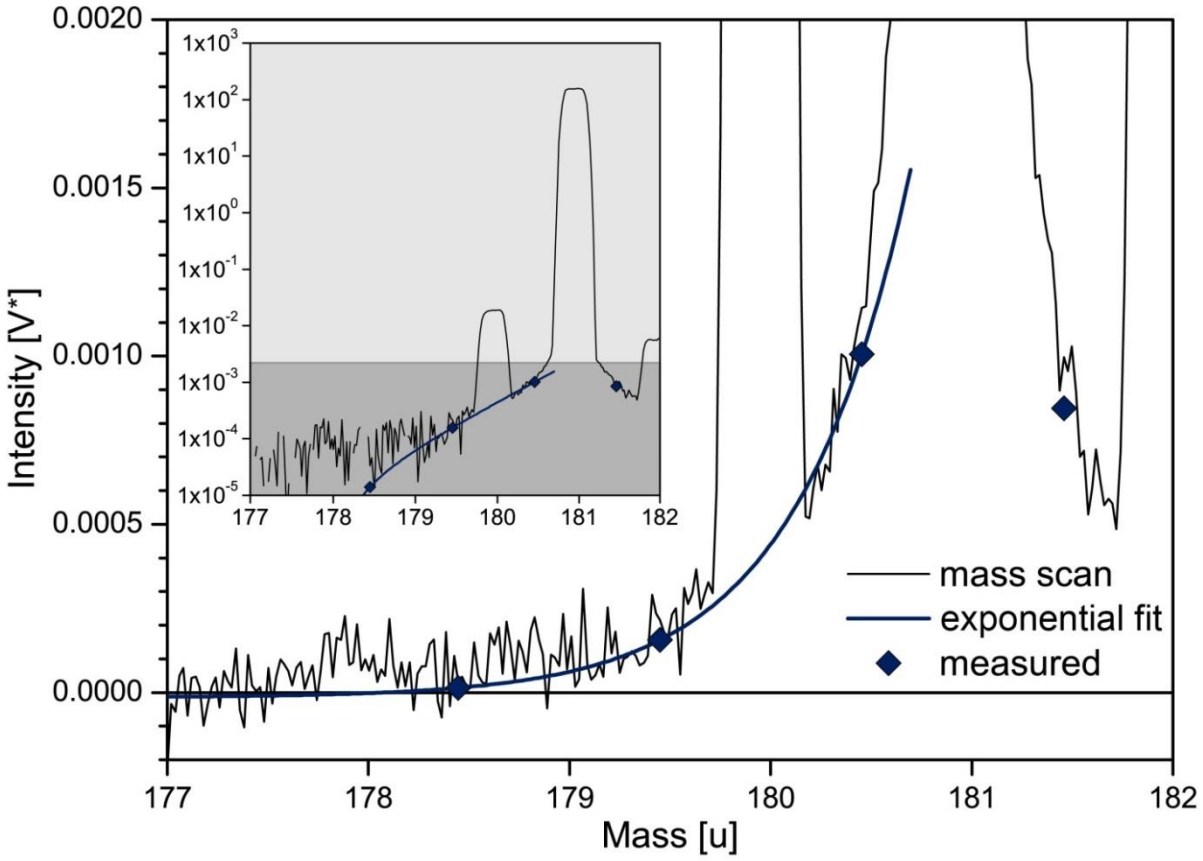

Fig. 2.1 Mass scan taken at an ^{181}Ta signal of *ca.* $1.5 \cdot 10^{-9}$ A (corresponding to 150 V*) at 0.02 u steps with 2 s integration time and using a 10^{10} Ω resistor. Diamonds correspond to half mass values taken for calculation of the exponential fit for tail correction. Repeatability (2 S.E.) is smaller than the symbol size. Resolvable peaks on ^{182}W and ^{178}Hf originate from Ta standard solution impurities (AMES Ta metal). The inset shows the full mass scan on a logarithmic scale. The darker shaded area in the inset illustrates the range of the expanded plot in linear space. Note that negative values around the baseline level are not shown on the logarithmic scale.

2.2.4 Terminology related to uncertainties

This study addresses two communities that use different vocabularies. In isotope geo- and cosmochemistry, data are usually presented relative to a standard, whereby it is commonly assumed that the standard measurements are affected by the same systematic biases as the sample measurements. The validity of the measurement is defined by variability observed in repeated measurements of standards or samples. The report of best estimates on absolute (true) isotope abundances requires a more thorough assessment of all random and systematic influences by applying the error approach in order to assign a realistic uncertainty to a measured quantity.

Here, we adopt the terminology recommended by the Joint Committee for Guides in Metrology and listed in the International Vocabulary of Metrology (VIM; Joint Committee for Guides in Metrology, 2012) but occasionally include terms in brackets that are used in the geochemical community. We follow the recommendations from the Guide to Expression of Uncertainty in Measurement (GUM) of ISO/BIPM (Joint Committee for Guides in Metrology, 2008) to present our best estimate of the absolute Ta isotope ratio and the corresponding isotope abundances in chapter 3.4. Type A (random) and Type B (evaluated by non-statistical means) uncertainties are discussed and propagated as the quadratic sums to obtain the measurement uncertainty. The expanded uncertainty includes a coverage factor (k=2).

The following terms are commonly used and accepted in geo- and cosmochemistry to report the validity of a measurement. The "(external) reproducibility" states the precision of a method reported as the relative variability of repeated standard (or sample) measurements, in standard deviations (usually with a coverage factor of k = 2). The appropriate term following VIM (Joint Committee for Guides in Metrology, 2012) is "intermediate precision", where the variability of repeated measurements is reported for the same instrument and method over an extended period of time. "Internal precision" as used in isotope geochemistry expresses the variability of a single measurement, e.g., 60 successive integrations for 8.4 s, usually as the experimental standard deviation of the mean ($S.D./N^{-0.5}$) with a coverage factor k = 2 (often called "2 standard error"), in which S.D. is the standard deviation and N is the number of successive integrations (60 in the example above). The closest equivalent in metrology, repeatability, includes replicate measurements on the same or similar objects over a short period of time.

Here, we use repeatability to state the uncertainty of single measurements corresponding to 2 S.E. (2 standard error = standard deviations of the mean with k = 2). Intermediate precision (external reproducibility), *i.e.*, the standard deviation of the observations with k = 2 is indicated as 2 S.D.

2.3 RESULTS AND DISCUSSION

Below, the intermediate precision (in geochemistry: external reproducibility) of our method is evaluated. The Ta isotope compositions of the three different standard materials are compared. Then, the results that are based on the newly developed amplifiers with 10^{13} Ω resistors are compared with those obtained using amplifiers with 10^{12} Ω resistors. After discussing the effect of abundance sensitivity on the $^{180}Ta/^{181}Ta$ ratio, we propose new best estimates of absolute Ta isotope abundances.

2.3.1 Intermediate precision and homogeneity of Ta standard solutions

The intermediate precision (external reproducibility) of Ta isotope ratios that were measured during an analytical session was calculated relative to a regression through the data of the respective session. The regression accounts for changes in abundance sensitivity of the instrument during a sequence (Fig. 2.2). Intermediate precision is reported as the variability of the standards in a session around the regression fit. Thus, it gives a minimum value from which a sample must deviate from the bracketing terrestrial standards to be resolved as anomalous. The typical intermediate precision (2 relative S.D.) for Yb corrected Ta isotope ratios at Bremen and Cologne-Bonn was ±4.4 ε and ±4.0 ε, respectively. The Re corrected data yielded an intermediate precision of ±4.1 ε but occasionally showed outliers (defined as >3 S.D. away from the mean of the data set, not included), making this procedure less reliable. The intermediate precision is typically a factor of *ca.* 1.5 to 2 higher than the typical repeatability (around ±2 to ±3.5 ε, 2 relative S.E.). One possible reason could be scatter of interfering element signals, particularly of the monitoring mass ^{178}Hf, that is not averaged out during a single measurement. The signal on ^{179}Hf is apparently more stable than the signal on ^{178}Hf, but this apparent stability reflects the larger tailing contribution from the ^{181}Ta signal to ^{179}Hf. Thus, when ^{179}Hf is used to correct for the interference of isobaric ^{180}Hf, the intermediate precision of $^{180}Ta/^{181}Ta$ is therefore worse, *i.e.*, *ca.* ±8 ε.

All Ta standard solutions were measured with external mass bias correction relative to both Yb and Re. Notably, the measured standard solutions have indistinguishable interference and mass bias corrected $^{180}Ta/^{181}Ta$ (Fig. 2.2). These particular standards can therefore be used interchangeably for bracketing of natural samples. The different standard solutions define a common intermediate precision of ±4.5 ε. We therefore suggest that the Ta isotope ratio that represents the natural one can be inferred from our suite of Ta standard solutions and that the Ta purification processes were not accompanied by resolvable isotope fractionation effects. The majority of this work is based on measurements of the AMES metal standard because it showed the lowest Hf impurity.

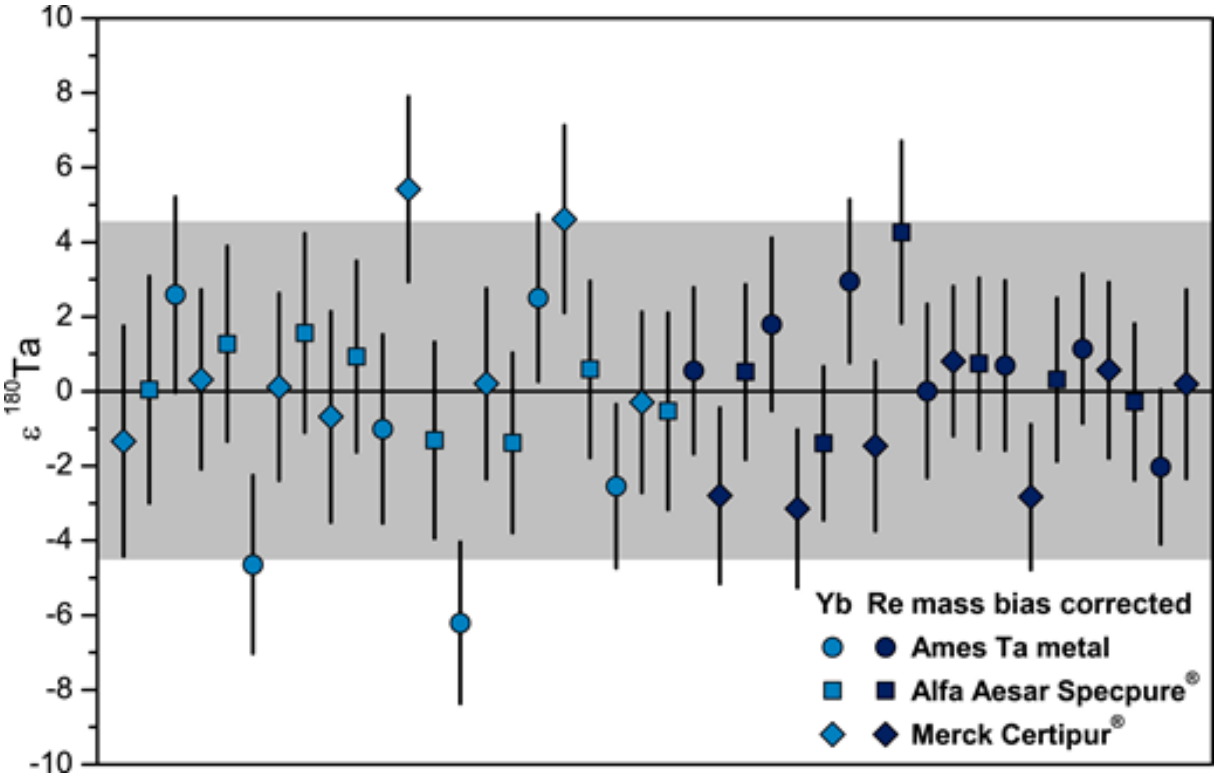

Fig. 2.2 Measured $^{180}Ta/^{181}Ta$ compositions for different Ta standard solutions, March 2016. To accommodate drift of abundance sensitivity, the data are shown relative to a linear and second order polynomial trend that was fitted through the sequence of Re- and Yb-based mass bias corrected data, respectively. Error bars are the 2 relative S.E. of the single runs and the shaded area represents the common intermediate precision (2 S.D.).

2.3.2 Low ion beam measurements using 10^{13} Ω resistor Faraday cup amplifiers

In order to evaluate the repeatability (internal precision in geochemistry) of the Ta isotope measurements with 10^{13} Ω resistors, we calculated the theoretically achievable in-run repeatability. The repeatability of measurements with Faraday cups is dependent on the sum of the shot noise, described by the Poisson distribution of ion detection, and the thermal Johnson-Nyquist noise of the amplifier resistor (Wieser and Schwieters, 2005). The shot noise describes the stochastic nature of impinging charged particles on the detector. The absolute uncertainty that is caused by the shot noise can be calculated as the inverse square root of the number of particles N at mass i that reach the detector, and 1 mV* being equivalent to 62,700 cps. This means that the relative contribution from shot noise is purely dependent on the intensity of the signal and decreases with higher intensity. The thermal noise of the amplifier that is coupled to the detector, in contrast, results from the agitation of charge carriers in an electrical circuit at non-zero temperature. This is the Johnson-Nyquist noise (ΔV) and is defined as

$$\Delta V = \sqrt{\frac{4k_B RT}{t_{int}}} \quad (2.3)$$

with k_B being the Boltzmann constant, R the resistivity, T the temperature, and t_{int} the integration time of the measurement. The Johnson-Nyquist noise is independent of the amount of collected particles and therefore induces a constant uncertainty. Consequently, the relative contribution of this thermal noise is most significant for very low ion beams.

Figure 2.3 shows the analytical repeatability of Ta isotope ratio data obtained with amplifiers with 10^{13} Ω resistors compared to the repeatability predicted by Poisson statistics combined with Johnson-Nyquist noise. Although there is an overall good agreement between the measured and calculated repeatability for the mass bias corrected isotope ratios, the isotope ratios that are additionally corrected for interfering ^{180}Hf show a systematically higher in-run repeatability than the predicted repeatability, particularly at low signal intensity. The higher in-run repeatability for the interference corrected isotope ratios likely reflects noise propagation from the amplifier that is used to collect the interference monitor at mass 178. Notably, the use of an amplifier with 10^{13} Ω resistor clearly improves the signal-to-noise ratio on mass 178 and therefore reduces the noise propagation compared to the use of a 10^{12} Ω resistor. This pattern becomes evident by the comparison of the repeatability in Hf corrected and uncorrected data obtained with 10^{12} and 10^{13} Ω amplifiers at mass 178, at *ca.* 40 V* for ^{181}Ta. While the correction for ^{180}Hf interference leads to an increase by 2 to 3 ε to about ±7 to ±8 ε when a 10^{12} Ω amplifier was used to collect ^{178}Hf (Cologne-Bonn), measurements at Bremen using the 10^{13} Ω amplifiers only yielded an increase in repeatability by *ca.* 1 ε or less, which results in a repeatability of ±3 to ±3.5 ε after interference corrections (2 relative SE). Together, the repeatability of Ta isotope measurements is thus limited by the noise contribution and counting statistics on both masses, 178 and 180, illustrating the advantage of the 10^{13} Ω amplifiers for precise Ta isotope ratio measurements.

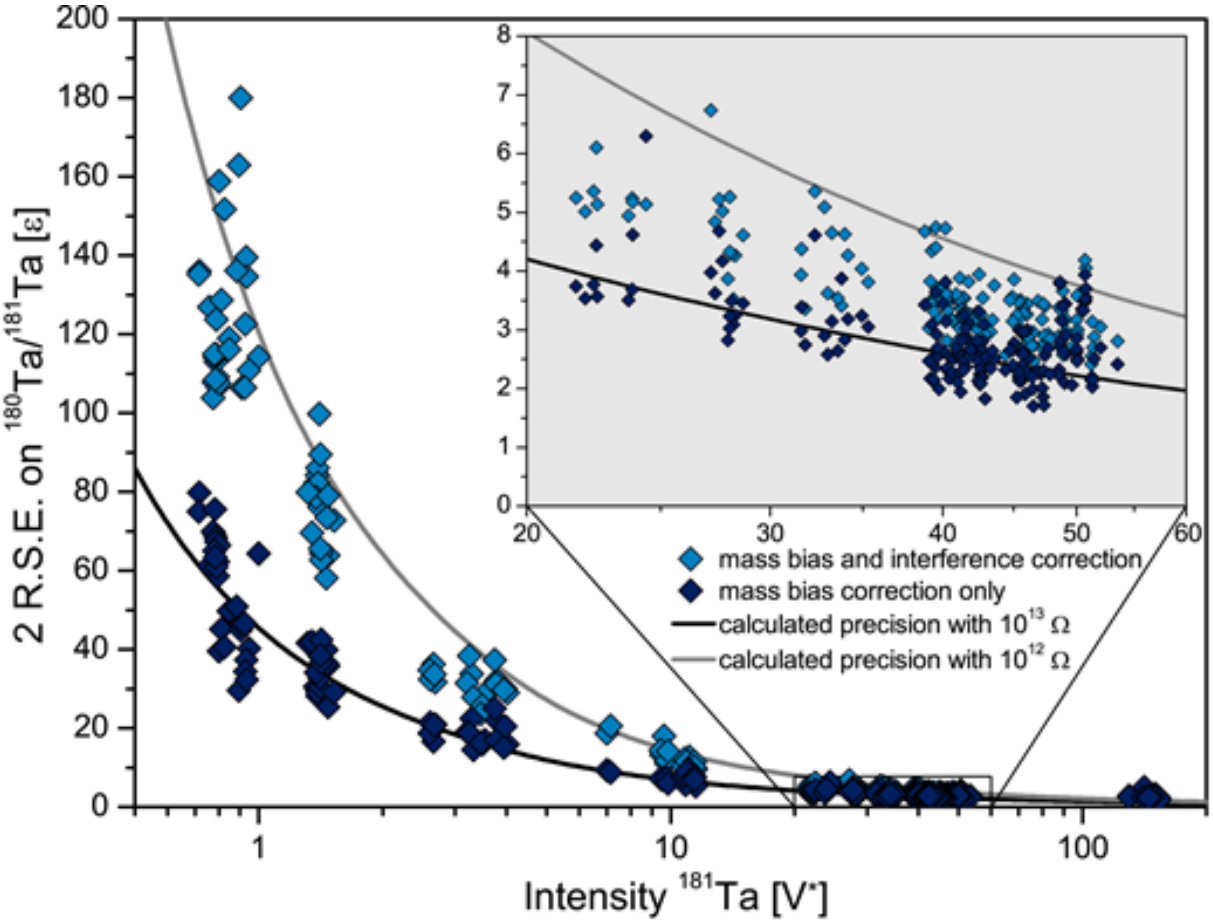

Fig. 2.3 Measured in-run repeatability (in geochemistry: internal precision) compared to theoretically predicted repeatability plotted against the voltage of ^{181}Ta. The data set comprises all measurements of standard solutions obtained with 10^{13} Ω resistors in Bremen. Curves show the theoretical repeatability for 10^{13} Ω and 10^{12} Ω resistors attached to the detector on mass 180 and are the sum of shot and Johnson-Nyquist noise at a given intensity. The repeatability calculated on mass 181 with a standard 10^{11} Ω resistor and the scatter from higher Ohm amplifiers on mass 180 were propagated. Dark blue diamonds show the repeatability obtained without correction of the ^{180}Hf interference, while the light blue diamonds illustrate the repeatability of the final results. The inset magnifies the range of intensity between 20 and 60 V* ^{181}Ta, where most measurements were conducted.

In Fig. 2.3, scatter around the theoretically predicted values likely arise from differences in the response delay times between the 10^{11} Ω amplifier that is used to collect ^{181}Ta and the 10^{13} Ω amplifiers. While 10^{11} Ω amplifiers process a signal within one second, higher resistivity amplifiers need around ten seconds to convert a detector signal into electronic readings. The same effect has previously been reported for signal drift with TIMS (Klaver *et al.*, 2016) and is prominent at timescales of transient signals in laser ablation-MC-ICP-MS (Kimura *et al.*, 2016). With solution MC-ICP-MS, a drop in intensity, due to, e.g., nebuliser fluctuations, is directly processed by 10^{11} Ω amplifiers for high-abundance masses, while it takes one or two integration cycles on the low-

abundance mass 180 with 10^{13} Ω amplifiers. On the cycle level, the measured data therefore may show spikes, followed by mirroring spikes in the opposite direction, when the signal is processed after the delay through the higher Ohm amplifiers. Higher integrations times of 16 s or more can minimise these effects or a correction might be applied as in laser ablation MC-ICP-MS (Kimura *et al.*, 2016). However, it is noteworthy that the intermediate precision is not affected, as long as the whole signal is integrated over a complete measurement run and no overall drift in signal intensities is present.

A major concern in TIMS work with new 10^{13} Ω amplifiers is the baseline stability over the course of an analytical session and during long-run measurements (Koornneef *et al.*, 2014; Liu and Pearson, 2014; Sarkar *et al.,* 2015). Generally, the stability of higher Ohm resistors was shown to be suitable for long-run TIMS measurements, also for the new 10^{13} Ω resistor Faraday amplifiers (Koornneef *et al.*, 2014). The baseline stability is of less concern for MC-ICP-MS measurements, as a run only takes 15 minutes including wash-out and uptake time. Any potential drift is therefore sufficiently covered by standard bracketing.

2.3.3 Effect of tailing on measured Ta ratios

The drift in Ta isotope ratios that was observed over several analytical sessions is related to the abundance sensitivity of the instrument. Changes in the instrumental vacuum directly translate into variable contributions of tailing effects on the measured intensity at mass 180, thus altering the measured $^{180}Ta/^{181}Ta$. This effect is evident when comparing the non-tailing corrected but mass-bias and interference corrected Ta isotope ratios with the ion getter pump (IGP) pressure for the two analytical sessions with the largest drift in vacuum readings (Fig. 2.4). The IGP pressure represents the vacuum condition in the back-end of the mass spectrometer, where the flight tube and the detectors of the instrument are located. A clear correlation between the measured $^{180}Ta/^{181}Ta$ and IGP pressure highlights the influence of ion collisions with residual gas on the actual abundance sensitivity. Notably, extrapolations of these trends to zero IGP pressure result in higher $^{180}Ta/^{181}Ta$ ratios than the proposed absolute tailing corrected value (Fig. 2.4). This indicates that the ^{181}Ta tail partially originates from collisions in the front part of the instrument. The drift in Ta isotope ratios relative to the IGP pressure is slightly less pronounced when ^{179}Hf is used to correct for ^{180}Hf interference than when ^{178}Hf is used, because of tailing from ^{181}Ta onto mass 179, which then additionally removes some of the tailing effect from ^{180}Ta.

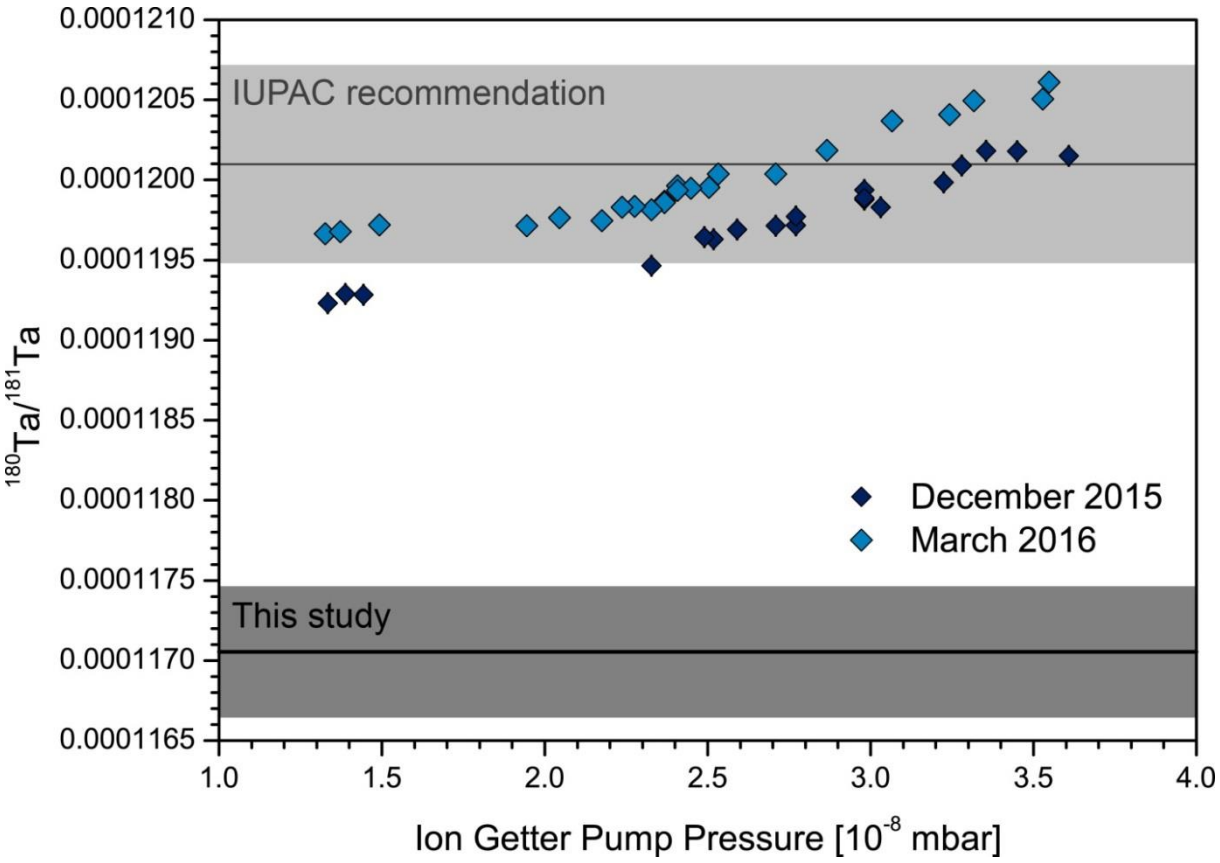

Fig. 2.4 Measured $^{180}Ta/^{181}Ta$ ratios plotted against the ion getter pump pressure in 10^{-8} mbar during the two sessions with the largest drift at the Cologne-Bonn facilities. The dark shaded area shows the Ta isotope ratio proposed in this study, the light shaded area represents the presently accepted value (de Laeter and Bukilic, 2005; Meija *et al.*, 2016). The individual in-run repeatability (2 S.E.) is smaller than or equal in size to the symbols. Ion getter pump data are taken from the individual log files of each measurement.

The analytical sessions that are illustrated in Fig. 2.4 show similar trends of increasing $^{180}Ta/^{181}Ta$ with IGP pressure, but also show an offset in $^{180}Ta/^{181}Ta$ relative to each other. This offset could be explained by different centre masses of the magnet or by different conditions in the low vacuum part of the mass spectrometer. To a smaller extent, pressure changes were also observed in earlier sessions but did not result in such a strong drift of measured $^{180}Ta/^{181}Ta$ ratios as exemplified in Fig. 2.4. During the two sessions at Cologne-Bonn illustrated in Fig. 2.4, a deteriorated skimmer cone was used that apparently caused a stronger pressure change in the analyser part of the instrument and consequently larger drift. In addition to the elevated maximum IGP pressure, the non-ideal cone geometry potentially changed the composition of the residual gas to a more argon-rich atmosphere. The larger mass of Ar atoms compared to, e.g., N_2, could then lead to a comparably stronger deflection of ions.

The dependence of tailing effects on different ion beam intensities was tested to verify the reliability of standard-sample bracketing at different intensities. The abundance sensitivity remained the same in both instruments for ion currents between $2 \cdot 10^{-10}$ and $2 \cdot 10^{-9}$ A for ^{181}Ta, corresponding to intensities from 20 to 200 V*. At such levels of ion currents, the tail contribution of ^{181}Ta on the ^{180}Ta signal displays a 1:1 correlation with the intensity of the ^{181}Ta signal. Consequently, even improperly concentration-matched standards therefore would not induce systematic biases in standard-sample bracketing methods. Furthermore, this stability in abundance sensitivity ensures the applicability of our tailing correction protocol with two tail measurements bracketing a sequence. Also the relative contribution of the ^{181}Ta tail on mass 179 with which the interference monitor ^{179}Hf is collected correlates linearly with the ^{181}Ta signal. At ion currents below $2 \cdot 10^{-10}$ A, in contrast, the relative contribution of the ^{181}Ta tail on lower masses is less pronounced, because it is within the scatter of the measured baseline. For such low intensities, the Ta concentrations of the bracketing standards need to closely match the concentration of the sample.

In another test, we investigated the influence of mass resolution on the abundance sensitivity of the instrument while keeping cup positions and the major tuning parameters constant. Tailing effects are strongest in low resolution (LR) and continually decrease from medium resolution (MR) to high resolution (HR). In MR and HR modes, the abundance sensitivity of the instrument was *ca.* 1 ppm at one u below ^{181}Ta compared to 2.5 ppm in LR. Hence, the measured mean Ta isotope ratio without tail correction decreases from 0.00012000(58) in LR to 0.00011845(4) in MR and to 0.00011838(3) in HR (uncertainty as intermediate precision in 2 S.D.). The decreasing tailing effects with increasing mass resolution at least in part relate to the much lower IGP pressure of 0.6 to $1 \cdot 10^{-8}$ mbar in MR and HR compared to 2 to $3.6 \cdot 10^{-8}$ mbar in LR. However, the difference in IGP pressure alone cannot fully explain the difference in Ta isotope ratios between the different mass resolution modes, because ^{180}Ta/^{181}Ta ratios in MR and HR are significantly lower than LR data from earlier sessions at comparable IGP pressures. Possibly, the improved abundance sensitivity in MR and HR can be explained by two physical and geometrical effects. First, the smaller slits produce a narrower beam. This results in a larger distance from the edge of the beam to the neighbouring cup, compared to a wider beam in LR. Consequently, even when the tail exhibits the same geometry in all resolution modes, the tail is shifted towards the centre of the cup by exactly the distance with which the beam edge is shifted towards the central mass of ^{181}Ta. Secondly, the smaller slit size in HR preferentially samples ions from an inner part of the ion beam. In the centre of the ion beam, the ion population is assumed to be more homogeneous in terms of its kinetic energy distribution. Therefore, ions with more dispersed kinetic energies in the outer section of the beam are blocked by the slit.

2.3.4 The absolute isotope composition of tantalum

The preparation of gravimetric solutions by mixtures of mono-isotopic tracers is considered as an approach to most accurately determine absolute isotope ratios (*e.g.*, Pritzkow et al., 2007). Such gravimetrically known isotope mixtures can be used to accurately correct for mass discrimination. In the case of Ta, however, a sufficiently pure ^{180}Ta tracer is commercially not available.

Only two recent studies have attempted to constrain the absolute isotope composition of Ta within the last 20 years (Weyer *et al.*, 2002; de Laeter and Bukilic, 2005) The values that are currently recommended by IUPAC are those by de Laeter and Bukilic (2005) who reported ^{180}Ta/^{181}Ta = 0.00012012(62) based on TIMS measurements. Weyer *et al.* (2002), in contrast, reported ^{180}Ta/^{181}Ta = 0.00011980(60) based on MC-ICP-MS measurements (intermediate precision reported as 2 S.D.). Both studies discuss the effects of abundance sensitivity on the measured ^{180}Ta/^{181}Ta ratios on the basis of a mass scan. However, in linear space, the tailing effect from ^{181}Ta on ^{180}Ta is difficult to detect. For this reason, de Laeter and Bukilic (2005) assumed that the accuracy of their measured ^{180}Ta/^{181}Ta ratios is unaffected by abundance sensitivity. In contrast, Weyer *et al.* (2002) expected tailing effects on ^{180}Ta based on the observed peak tailing of a ^{238}U beam. Based on this observation, after applying a baseline correction, they suggest the presence of a residual ^{181}Ta tail of approximately 5 ppm on ^{180}Ta, resulting in a ~4% lower ^{180}Ta/^{181}Ta ratio than their measured value, *i.e.*, by about 0.000115. Nevertheless, neither of these studies obtained precise measurements between the peaks to better quantify the exact tail contribution. Our half mass measurements reveal a ^{181}Ta tail contribution of around 2.5 % in the Neptune MC-ICP-MS at Bonn and Bremen on the ^{180}Ta signal (Fig. 2.1). Consequently, the Ta isotope ratio of 0.00012012 on which the current IUPAC recommended isotope composition of Ta is based, is most likely an overestimation.

The importance of the tail correction in establishing the best estimate on the Ta isotope ratio is furthermore illustrated by the improvement in intermediate precision that is seen when data are corrected for abundance sensitivity effects. Our mean values of standard measurements that are mass-bias and interference corrected, but not abundance sensitivity corrected ^{180}Ta/^{181}Ta in 22 LR sequences range from 0.00011933(10) to 0.00012023(8), *i.e.*, corresponding to 75 ε difference (experimental standard deviations, k = 2). This range is substantially worse than the intermediate precision of ^{180}Ta/^{181}Ta measurements within the individual analytical sessions, which is typically <4.5 ε after interference, mass-bias, and drift correction. If ^{180}Ta/^{181}Ta ratios are also corrected for abundance sensitivity, both the variability within sequences (by about 1 ε) and the maximum spread in mean values of the individual sequences is reduced (in case of the two sequences with the most extreme Ta ratios before tailing correction to only 5 ε).

Based on an improved determination of the tail contribution on ^{180}Ta, we propose here a new best estimate of the absolute ^{180}Ta/^{181}Ta isotope ratio of 0.00011705(41) (Fig. 2.4; 2.5), which is equal to a ^{181}Ta/^{180}Ta of 8543(30) with expanded measurement uncertainty of k = 2. This value represents the mean of 12 analytical sessions over a 28 months period from two laboratories (Table 2.3), with 430 single measurements forming the basis of the data set. The arithmetic mean of the individual sessions is considered most appropriate for the determination of the absolute ^{180}Ta/^{181}Ta ratio. Different methods (*i.e.*, Re and Yb based mass discrimination correction, different mass resolutions) and standard solutions were used in the same sessions for direct comparison. As no differences were resolved between different methods and Ta standard solutions the data were combined into mean values. The data selected were limited to measurements with a signal of more than 25 V* on ^{181}Ta at Bremen and Cologne-Bonn, providing sufficient counting statistics and a stable tail contribution on ^{180}Ta. One of 22 sequences obtained during the individual 12 sessions was rejected for the final evaluation due to an exceptionally large non-linear drift during the sequence, leading to values up to 5 standard deviations above the mean of the data set. Of the remaining 430 measurements, 16 measurements were rejected using a 2-sigma outlier criterion. These data have typically been obtained during sessions with relatively large drift that has possibly been insufficiently corrected with our linear offline tailing correction. The mean of the remaining single measurements is 0.00011709(36) and overlaps with the mean of the remaining sessions of 0.00011705(27) within the experimental standard deviation and k = 2 (in geochemistry 2S.D.). Importantly, the abundance sensitivity corrected data from all reported measurement sessions at Cologne-Bonn and Bremen overlap within their 2 standard deviation (Table 2.3; Fig. 2.5). Also the use of different elements (Yb, Re) for mass bias correction results in absolute Ta isotope ratios that are indistinguishable from each other (Table 2.4).

The large number of data obtained with different methods and standards allows calculating the respective standard deviation of the mean for ^{180}Ta/^{181}Ta, which will then allow evaluating possible systematic effects between different methods (Table 2.4). The ^{180}Ta/^{181}Ta ratios measured in MR and HR (0.00011744(2), n = 8 and 0.00011739(2), n =8) are outside the standard deviations of the mean (k = 2) of all data (^{180}Ta/^{181}Ta = 0.00011709(2), n = 414). It remains ambiguous whether these apparently higher ^{180}Ta/^{181}Ta ratios reflect the relatively small number of data that were obtained in MR and HR mode or relate to inaccuracies of tailing determinations in MR and HR mode, where the improved abundance sensitivity reduces the counting statistics and hence repeatability for the half mass measurements and impedes an sufficiently accurate empirical fit. Likewise, Re-based mass bias corrected Ta isotope ratios on average are slightly higher (^{180}Ta/^{181}Ta = 0.00011716(2), n = 58) than the mean of the Yb-based mass discrimination corrected data (^{180}Ta/^{181}Ta = 0.00011708(2), n = 356). This apparently high ^{180}Ta/^{181}Ta may also be an expression of the limited number of Re-corrected

data, which were obtained over two analytical sessions at Cologne-Bonn only. The full variability seen in the rest of the Yb-corrected data over the course of the project is not represented by the Re values, thus confirming this assertion. However, slight systematic differences between the Yb and Re normalised data that were related to insufficient correction for the instrumental mass bias cannot be excluded. All other data obtained with different standards and methods are indistinguishable within their standard deviation of the mean (k = 2; 2 S.E. in geochemistry). This indicates that differences in cup efficiency, gain correction between different sessions, and differences in isotope compositions of the standards (see chapter 2.3.1) are negligible within the uncertainty of our measurements.

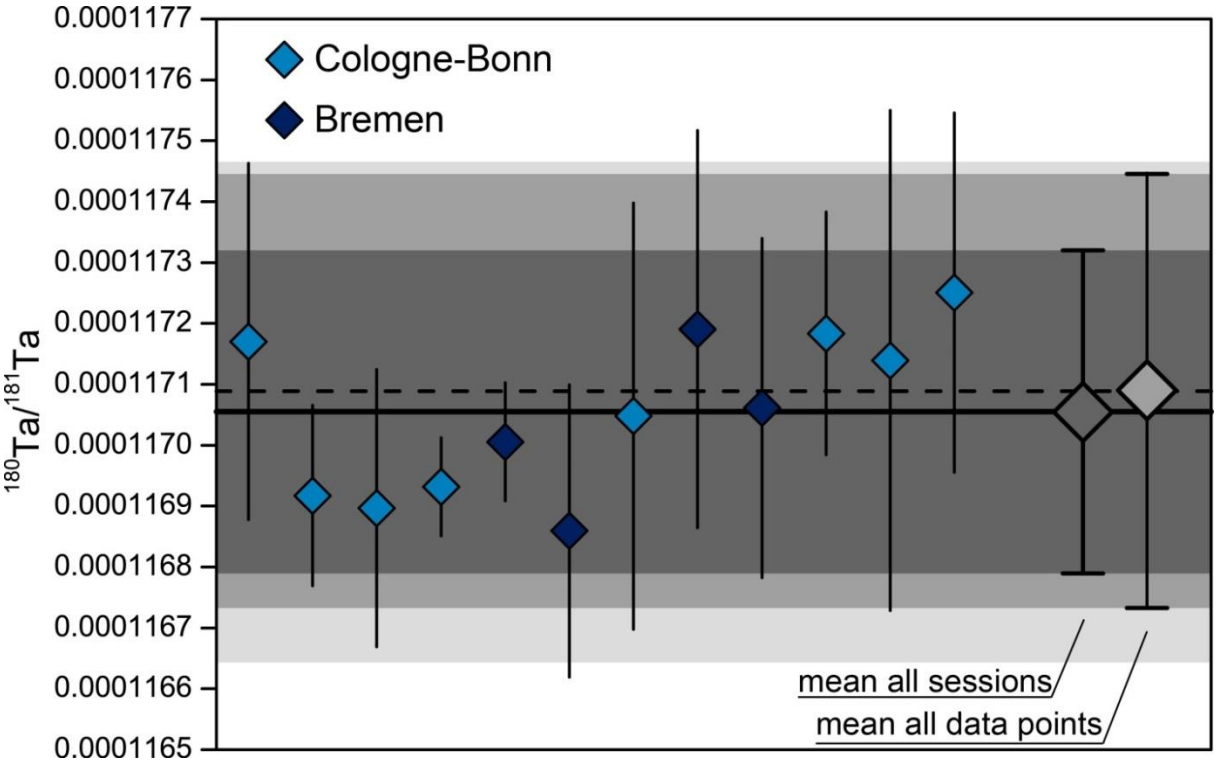

Fig. 2.5 Abundance sensitivity, interference, and mass bias corrected $^{180}Ta/^{181}Ta$ data obtained in 12 sessions from 2013 to 2016 with dark blue symbols for Bremen and light blue symbols for Cologne-Bonn data. Error bars refer to the experimental standard deviation of the respective session with coverage factor k = 2. The dark shaded area marks the standard deviation (k = 2) of all sessions (solid line). The grey field represents the variability (standard deviation, k = 2) of all 414 data points left after a 2 sigma outlier test and their mean as the dashed line. The light grey field underneath indicates the expanded measurement uncertainty relative to the solid line. Data with Re-based mass bias correction, obtained in September 2015 and March 2016, were merged with the Yb-based data from the same sessions.

Table 2.3 Abundance sensitivity corrected Ta isotope ratios measured in individual analytical sessions used to calculate the estimate of the absolute Ta isotope ratio. Tantalum standard solutions and the element used for mass bias correction are indicated. MB corr. refers to the element used for external mass bias correction of data in the respective session. AA abbreviates Alfa Aesar. Uncertainties are given as experimental standard deviation.

Session date	Facility	N	$^{180}Ta/^{181}Ta$		$^{181}Ta/^{180}Ta$		MB corr.	Standards
			Mean	Uncertainty	Mean	Uncertainty		
27.10.2013	Cologne-Bonn	25	0.000 117 17	0.000 000 15	8534.6	10.7	Yb	AA
21.12.2013	Cologne-Bonn	16	0.000 116 92	0.000 000 07	8553.0	5.4	Yb	AA
08.01.2014	Cologne-Bonn	23	0.000 116 90	0.000 000 11	8554.6	8.3	Yb	AA
10.05.2014	Cologne-Bonn	24	0.000 116 93	0.000 000 04	8552.0	2.9	Yb	Ames
05.06.2014	Bremen	20	0.000 117 01	0.000 000 05	8546.6	3.5	Yb	Ames
28.-30.07.2014	Bremen	30	0.000 116 86	0.000 000 12	8557.3	8.8	Yb	Ames
12.09.2014	Cologne-Bonn	22	0.000 117 05	0.000 000 17	8543.5	12.8	Yb	Ames
16.-19.03.2015	Bremen	72	0.000 117 19	0.000 000 16	8533.1	11.9	Yb	Ames
22.-24.06.2015	Bremen	67	0.000 117 06	0.000 000 14	8542.5	10.2	Yb	Ames
15.-16.09.2015	Cologne-Bonn	60	0.000 117 18	0.000 000 10	8533.6	7.3	Yb, Re	Ames
14.12.2015	Cologne-Bonn	18	0.000 117 14	0.000 000 21	8536.8	15.0	Yb	AA, Ames
29.02.-02.03.2016[a]	Cologne-Bonn	40	0.000 117 25	0.000 000 15	8528.7	10.7	Yb, Re	AA, Ames, Merck

a: This session includes the MR and HR data. One Yb-based mass bias corrected sequence was rejected from the dataset because of unusual large drift in abundance sensitivity during this session (see text).

Table 2.4 Estimates of the absolute Ta isotope ratio including abundance sensitivity corrected Ta isotope ratios compiled after different instruments, standard solutions, and methods for comparison. All data were measured in low resolution if not stated otherwise.

	$^{180}Ta/^{181}Ta$	Standard deviation	N	2 Standard deviation of the mean
This study				
Mean sessions[a,b]	**0.000 117 05**	0.000 000 13	12	0.000 000 08
Mean all data[a,b]	0.000 117 09	0.000 000 18	414	0.000 000 02
Mean data Bremen[c]	0.000 117 08	0.000 000 18	181	0.000 000 03
Mean data Cologne-Bonn[a,b]	0.000 117 10	0.000 000 18	233	0.000 000 02
Alfa Aesar Specpure®[,a]	0.000 117 07	0.000 000 22	89	0.000 000 05
Ames pure metal[a]	0.000 117 10	0.000 000 16	314	0.000 000 02
Merck Certipur®[,a]	0.000 117 13	0.000 000 05	8	0.000 000 03
Re mass bias corrected[b]	0.000 117 16	0.000 000 08	58	0.000 000 02
Yb mass bias corrected[b]	0.000 117 08	0.000 000 19	356	0.000 000 02
Medium resolution[c]	0.000 117 44	0.000 000 02	8	0.000 000 02
High resolution[c]	0.000 117 39	0.000 000 02	8	0.000 000 02

Estimates of the absolute Ta isotope ratio[d]	$^{180}Ta/^{181}Ta$		$^{181}Ta/^{180}Ta$	
	Mean	Uncertainty	Mean	Uncertainty
This study	**0.000 117 05**	**0.000 000 41**	**8543**	**30**
Weyer *et al.* 2002[30]	0.000 119 80	0.000 000 60	8347	42
de Laeter and Bukilic 2005[3]	0.000 120 12	0.000 000 62	8325	43

a: compiled from Re- and Yb-based mass bias correction
b: compiled from all three Ta Std solutions
c: Yb-based mass bias correction applied to AMES and Alfa Aesar Ta standards
d: Uncertainty as expanded measurement uncertainty or as stated in previous publications (k = 2)

These minor potential systematic effects describe above could indicate that the overall data set is not purely statistically controlled. While the MR and HR offset most likely is attributed to inaccuracies in the empirical tailing fit, the accuracy of the mass discrimination correction and the input is further considered. Nonetheless, the small absolute difference in Yb and Re normalised Ta isotope ratios of only 0.00000008 is well within the expanded measurement uncertainty (±0.00000041). If the recently proposed Yb isotope abundances by Wang *et al.* (2016) rather than those by Albalat *et al.* (2012) are used for correction of the instrumental mass bias, the mean $^{180}Ta/^{181}Ta$ of the Yb-corrected data shifts further downwards by approximately 25 to 30 ε (0.25 -

0.3%), which is similar to the random measurement uncertainty (k = 2) of the $^{180}Ta/^{181}Ta$ ratio. The Re isotope composition used in this work and recommended by IUPAC is based on a publication by Gramlich *et al.* (1973) ($^{187}Re/^{185}Re$ = 1.6739). However, a $^{187}Re/^{185}Re$ = 1.6755 was proposed by Suzuki *et al.* (2004). Using this value, Re-based mass bias corrected data are lowered by about 5 ε, which is indistinguishable from the Yb-based mass bias corrected value within its standard deviation of the mean. The typical mass bias for heavier masses around 1% per u (Maréchal *et al.*, 1999) is reduced through the high sensitivity interface as more lighter ions are transmitted relative to heavier ones (Newman, 2012). The observed mass bias in this study ranges from 0.5 – 0.7 % u^{-1} (in case of Re-based correction) to 0.7 – 1 % u^{-1} for Yb (after Albalat *et al.*, 2012). The somewhat lower mass discrimination of Re compared to Yb may relate to the higher average mass of Re. On the contrary, mass discrimination calculated relative to Yb ratios of Wang *et al.* (2016) scatters more and often yields unusual low values (0.3 – 0.8 % u^{-1}), calling the applicability of their Yb composition for mass bias correction on our instrument into question.

A strong indication that our mass discrimination correction works sufficiently accurate is the consistency between Re- and Yb-normalised Ta isotope compositions (Yb after Albalat *et al.*, 2012; Table 2.4). The difference in mass discrimination correction due to different reference Yb and Re isotope ratios amounts to 0.3 % shift in $^{180}Ta/^{181}Ta$, while tailing effects reduce the Ta isotope ratio by 2.5 %. Therefore, in this study, mass discrimination effects are regarded as minor with respect to the uncertainty of the proposed absolute Ta isotope ratio. The use of two different elements to correct for instrumental mass discrimination is an advantage over earlier studies. The use of two different instruments and methods also corroborates the consistency of our results by inter-laboratory comparison. Therefore, potential systematic contributions arising from the use of only one instrument, one method of mass bias correction and inaccuracies in the tailing correction should be, at least in part, reflected by the random measurement uncertainty of the large amount of data obtained with different instruments and methods.

Potential additional sources of uncertainty are evaluated separately and are included in the combined uncertainty. Individual components of uncertainty that contribute to the final measurement uncertainty of the Ta isotope ratio are listed in Table 2.5. The combined Type A random uncertainty associated with our measurement are calculated as the mean of the individual measurement uncertainties propagated with the standard deviation of the mean of all independent sessions (Tables 2.3; 2.5). We further evaluated the influence of Type B uncertainties on the estimate of the Ta isotope ratio. The tailing correction typically lowers the measured $^{180}Ta/^{181}Ta$ ratio by 0.00000250. This value scatters with a standard deviation of 0.00000040, depending on the particular vacuum quality encountered in the respective session. This approach would be an overestimation of tailing-induced uncertainty on the Ta isotope ratio, because the tailing correction

Table 2.5 Statistical (Type A) and non-statistical (Type B) uncertainty components and their propagation.

	$^{180}Ta/^{181}Ta$		$^{181}Ta/^{180}Ta$	
Type A random uncertainty components				
mean of individual uncertainties of independent sessions	0.000 000 12		9.0	
standard deviation of independent sessions	0.000 000 13		9.7	
number of independent sessions	12		12	
standard deviation of the mean of independent sessions	0.000 000 04		2.8	
Type B uncertainty components				
mass discrimination correction	0.000 000 10		7.3	
tailing correction	0.000 000 13		9.1	
Combined measurement uncertainty	Type A	**Type A and B**	Type A	**Type A and B**
combined measurement uncertainty	0.000 000 13	**0.000 000 21**	9.4	**15.0**
expanded measurement uncertainty (k=2)	0.000 000 26	**0.000 000 41**	18.8	**30.0**
% relative expanded measurement uncertainty (k = 2)	0.22	**0.35**	0.22	**0.35**

reduces the overall variability in the data set present prior to application of the correction. Thus, uncertainty caused by the correction is to a large extent already covered in the standard deviation from the individual sessions. Because the empirical fit describes the tailing correctly (Fig. 2.1), we assume an additional source of uncertainty deriving from inaccuracies of our empirical tailing estimation to be less than 5 % of the correction value. This additional uncertainty component added to the mean value is of comparable magnitude as the combined random measurement uncertainty (Table 2.5). With this additional uncertainty contribution, all individual session means (combined uncertainty, k = 2) are in agreement with the arithmetic mean of the sessions. The mass discrimination correction is always less than the tailing correction. The accuracy of the correction and the extent to which differences in instrumental mass discrimination are already covered in the random uncertainty of the session is not known. We estimate a 10 % uncertainty on the typical correction of 0.00000100, which roughly corresponds to the experimental standard deviation of this correction observed in independent sessions. Systematic offsets due to the use of the exponential mass discrimination law (also known as Russell's law) might exist but are considered as being negligible, as our applied correction is of the expected magnitude (Maréchal *et al.*, 1999). The uncertainty from isobaric corrections is already propagated in the measured ratio, as illustrated in Fig. 2.3, and the accuracy of this correction is ensured by the doping tests. The gain correction of the

amplifiers, especially of the 10^{13} Ω resistor equipped amplifiers, exhibits an intermediate precision of the calibration of 0.01 % (1 ε), which is negligible with respect to other sources of uncertainty. The expanded measurement uncertainty on $^{180}Ta/^{181}Ta$ of 0.00000041 is given as the propagated Type A and B combined standard measurement uncertainty and a coverage factor of k = 2 (Table 2.5).

Our best estimate of the $^{180}Ta/^{181}Ta$ isotope ratio of 0.00011705(41) equals a recalculated $^{181}Ta/^{180}Ta$ ratio of 8543(30). This translates to absolute isotope abundances of 0.011704(41) % for ^{180}Ta and 99.988296(41) % for ^{181}Ta (Table 2.6). Using the Ta isotope masses with their reported uncertainties of 179.9474648(48) u and 180.9479958(38) u (Wang *et al.*, 2012), the absolute atomic weight of Ta is 180.9478787(38) u (propagated uncertainty with k = 2 and Monte Carlo approach; Sprung *et al.*, 2010). This atomic weight is in good agreement with the value proposed by de Laeter and Bukilic (2005) of 180.9478780(20) u. The reason for the somewhat better precision stated in the previous work is not reconciled, as the total uncertainty mainly depends on the uncertainty on the mass of ^{181}Ta.

Table 2.6 Proposed absolute Ta isotope abundances and new atomic mass of Ta presented with expanded uncertainties with k = 2.

	unit	value	uncertainty
Abundance of ^{180}Ta	%	0.011708	0.000041
Abundance of ^{181}Ta	%	99.988292	0.000041
Atomic mass	u	180.9478787	0.0000038

2.4 CONCLUSIONS

We developed a high-precision method to measure $^{180}Ta/^{181}Ta$ isotope ratios, targeted for measurements of extraterrestrial samples with low concentrations of Ta. Our analytical method yields an intermediate precision (geochemistry: external reproducibility) of *ca.* ±4 ε for measurements relative to a standard, which appears to be sufficient to resolve isotope anomalies in early solar system materials (see chapter 4). The very low abundance of ^{180}Ta and the substantial isobaric interference by ^{180}Hf have previously hampered high-precision measurements. Newly developed 10^{13} Ω resistor Faraday cup amplifiers were tested for the first time in solution MC-ICP-MS and demonstrated to be of paramount importance for applications of Ta isotopes systematics in small sample sizes, as is the case for extraterrestrial materials. This claim is underlined by comparable intermediate precision for measurements of ~100 ng with 10^{12} Ω resistors in relation to 25 ng with 10^{13} Ω resistors. To obtain precise Ta stable isotope data from bulk meteorites (typically

having Ta contents of approximately 20ng/g; Münker *et al.*, 2003), only ~1.2 g compared to ~4 g (with 10^{12} Ω amplifiers) are now required. Three terrestrial standard materials were measured and their stable isotope composition proved to be indistinguishable.

Abundance sensitivity is shown to be a very important issue for accurate Ta isotope ratio measurements. Changes in vacuum conditions of the mass-spectrometer can exert a strong influence on the measured $^{180}Ta/^{181}Ta$ ratios. Therefore, a tail measurement routine was performed at the beginning and end of each sequence 0.5 u away from the peak masses. An empirical fit plotted through these half mass data allowed the accurate correction of tail contributions from ^{181}Ta onto ^{180}Ta. Data acquisition in medium and high resolution is less prone to these tailing effects than data acquisition in low resolution and results in more robust data for a trade-off in sensitivity. Furthermore, it is shown that the tailing contribution is correlated with the IGP pressure but, in part, also derives from the front part of the instrument.

Considering the importance of tailing effects, the IUPAC recommended Ta isotope ratio was re-evaluated and abundance sensitivity issues appear to have been underestimated in the past, leading to an overestimation of the previously proposed ^{180}Ta isotope abundance by *ca.* 2.5 %. Errors imparted from possibly inaccurate Yb and Re isotope ratios reported in the literature or inaccurate mass discrimination correction are less significant than the effects of other uncertainties such as tail correction or counting statistics. For the first time, we present Ta isotope data that include a robust tail correction. Employing this tail correction, consistent Ta isotope data were obtained with different methods and instruments. The newly proposed $^{180}Ta/^{181}Ta$ ratio of 0.00011705(41) translates to isotope abundances of 0.011704(41) % for ^{180}Ta and 99.988296(41) % for ^{181}Ta, and an absolute atomic weight of 180.9478787(38) u for Tantalum (combined uncertainties with coverage factor of k = 2).

Chapter III

High precision Tantalum isotope ratio measurements of terrestrial samples and meteorites: evaluation of potential Ta isotope fractionation during Earth's formation and differentiation

3.1 INTRODUCTION

Tantalum has the atomic number 73 and consists of two isotopes with masses 180 and 181. The large spread in isotope abundances of 99.988295% for ^{181}Ta and only 0.011705% for the minor isotope ^{180}Ta poses a challenge to attain high-precision data (chapter 2). Primitive meteorites contain less than 30ng/g Ta (Münker *et al.,* 2003), making Ta the rarest element and ^{180}Ta the rarest stable nuclide in the solar system. Interestingly, ^{180}Ta is the only observationally stable isotope in an excited nuclear state. Tantalum is a high-field-strength-element (HFSE) with low ionic radius and an ionic charge of +5 in all silicate rock reservoirs on Earth. As a highly incompatible trace element, it is enriched to 0.7µg/g in the crust (Rudnick and Gao, 2014), with an overall range of concentrations in rocks and minerals from a lower-ng/g level in depleted mantle rocks (Weyer *et al.,* 2003) to several weight per cent in ore minerals such as the tantalite or tapiolite series [$(Mn,Fe)(Ta,Nb)_2O_6$]. The low concentration in many terrestrial and all extraterrestrial materials, in addition to the extreme isotope ratio, so far hindered an assessment of potential Ta isotope fractionation.

Possible Ta isotope fractionation effects in elemental redistribution during geological processing have not been investigated yet. Melting of mantle rocks leads to large depletions in the residuum and subsequent re-fertilization can strongly influence the Ta content of depleted mantle rocks (*e.g.*, Weyer *et al.,* 2003). Rock-forming-minerals, such as rutile or amphibole, are able to fractionate Ta from a melt or an aqueous fluid in subduction zones and other hydrated settings (e.g. Brenan *et al.,* 1994; Ionov and Hofmann, 1995; Foley *et al.,* 2000; Tiepolo *et al.,* 2000). In addition, sub-solidus to hydrothermal mobilization in fluxed pegmatite systems fractionates elements like Ta and other HFSEs during ore formation (Linnen *et al.,* 2012). Despite the potential of elemental

fractionation, the degree of Ta stable isotope fractionation is theoretically limited with a relative mass difference between the two isotopes of only 0.55%. Equilibrium isotope fractionation changes with $1/T^2$, thus only smallest isotope fractionation can be expected in high temperature systems. However, the nuclear field shift effect was shown to be dominant for isotope fractionation of heavier elements (Bigeleisen, 1996). Charge distribution in an atomic nucleus is altered by the number of accompanying neutrons and results in an impact on the electron shell. This gives rise to isotope effects in different bonding environments for heavy elements (Schauble, 2007). Nuclear volume effects are most prominent in redox-change related distribution between different phases, as the electron orbitals are occupied differently and the electron density is changed near the nucleus. These changes in electron configuration can cause isotope effects larger than those expected from molecular vibrations, thus allowing to use heavy element stable isotope fractionation for geological applications such as paleoredox proxies, e.g. Tl (Rehkämper *et al.,* 2002), U (Weyer *et al.,* 2008), or Re (Miller *et al.,* 2015).

Tantalum, however, does not show redox changes in the accessible silicate Earth, but for other elements there is evidence for nuclear field shift induced fractionation taking place between isotopes of the same valence, depending on different bonding environments, e.g. for Hg^{2+} (Schauble, 2007). Measurements of isotope shifts in optical spectra of ^{180}Ta suggest a prominent shift for single s-electron transitions, which is comparable to other elements expected to show nuclear field shift effects (Guthöhrlein *et al.,* 1994). The nuclear volume of ^{180}Ta is not given in any available nuclear data sets, as the minor ^{180}Ta is not present in its nuclear ground state (Angeli and Marinova, 2013), and ^{180}Ta is known to be a deformed nucleus (Soloviev, 1998). Both the size and shape of a nucleus influence the extent of the nuclear field shift effect (Bigeleisen, 1996). The extent of possible fractionation is thus not easy to constrain for Ta, which may give room for unexpectedly large isotope effects, even for non-redox involved reactions. Especially environments with progressive Rayleigh type melt depletion or low temperature environments are candidate test sites for potential Ta isotope fractionation on Earth. Solar system materials, in contrast, show a large range of oxygen fugacities down to values as low as ΔIW -6. Enstatite chondrites are sufficiently reduced that Ta^{3+} may be present and, hence, the nuclear field shift effect becomes significant for isotope fractionation during physical redistribution of Ta between different phases. Recent experiments argued that conditions on reduced meteorite parent bodies such as those of enstatite chondrites are sufficiently reduced for the presence of Ta^{3+} (Cartier *et al.,* 2014; Cartier *et al.,* 2015), in contrast to other publications that argue for Ta^{5+} at such conditions (Burnham *et al.,* 2012; Fonseca *et al.,* 2014). Hence, the relevance of reduced Ta^{3+} in natural samples is yet to be tested and may be solved with high-precision Ta isotope measurements.

Apart from mass dependent isotope fractionation, extraterrestrial materials are known to show further effects. Tantalum in meteorite samples may show more pronounced isotope anomalies as meteorites represent pristine material of the early solar system and did not suffer planetary-scale homogenization like rocks on Earth. Nucleosynthetic anomalies as stellar vestiges preceding the solar system have been identified in a number of extraterrestrial materials and can be used to constrain physical and chemical processes active in the protoplanetary disk and to trace possible building blocks of the terrestrial planets (see Dauphas and Schauble, 2016, and references therein for a recent review). The exact fractions of ^{180}Ta present in the solar system derived from slow neutron capture (branched s-process) as well as from neutrino reactions (ν-process, a distinct p-process) during nucleosynthesis are still discussed in the astrophysics community (e.g. Mohr *et al.,* 2007; Travaglio *et al.,* 2011; Rauscher *et al.,* 2013). Identification of Tantalum nucleosynthetic anomalies and their correlation with other nucleosynthetic isotope anomalies may allow testing the different astrophysical models of ^{180}Ta production. The unique properties of ^{180}Ta make it also a useful tracer to probe the irradiation environment around the young active sun. First, gamma radiation is able to induce a de-excitation of isomeric ^{180}Ta to the ground state with a subsequent decay to ^{180}Hf and ^{180}W with a half-life of 8.1 hours (Collins *et al.,* 1988). Secondly, the young sun accelerated protons which might have induced nuclear reactions on nuclides at the inner edge of the protoplanetary disk (Lee *et al.,* 1998; Gounelle *et al.,* 2001). Indeed, ^{10}Be was identified as an in-situ spallation product in the early solar system (McKeegan, 2000). Furthermore, there is a discrepancy between the V isotope compositions of meteorites and terrestrial rocks, which was associated with an early irradiation of material not present in Earth but in chondrites (Nielsen *et al.,* 2014). Tantalum-180, as a minor isotope and an odd-odd nuclide like ^{50}V, is similarly prone to nuclear ingrowth and may give some new insights into the V problem.

This work presents the first Tantalum isotope data for representative terrestrial and extraterrestrial samples, measured with multicollector-inductively coupled-mass spectrometry (MC-ICP-MS). Faraday detectors equipped with newly developed 10^{13} Ω amplifier resistors are a key development in measuring the low abundance ^{180}Ta and ^{180}Hf as interference monitor in small extraterrestrial samples at sufficient precision (chapter 2.3.2). A purification protocol for silicate samples is presented here and challenges in high-precision measurements are addressed in detail. Terrestrial materials were analyzed for their Ta isotope compositions to assess possible applications of the new high precision method and to investigate the terrestrial Ta inventory for possible isotope fractionation between different rock reservoirs. We expand our survey to bulk meteorite samples and show the applicability of our method to small-sized extra-terrestrial samples by presenting the first Ta isotope data for early solar system material.

3.2 METHODS

The low abundance of Tantalum and the extremely low ratio of $^{180}Ta/^{181}Ta$ require very clean elemental separation of Ta. Insufficiently purified Ta samples may suffer from inappropriate mass bias correction and molecular interference related issues. Especially an isobaric interference from the most abundant Hf isotope ^{180}Hf requires ultra-clean elemental separation protocols for Ta. Furthermore, the accuracy and precision of Ta isotope ratio measurements of silicate samples was carefully evaluated.

3.2.1 Sample description

To investigate many of the terrestrial reservoirs where stable Ta isotope fractionation may take place, a set of samples from diverse tectonic settings, different degrees of incompatible element depletion and different ages were evaluated, including certified standard materials. The solar system inventory is assessed by six bulk meteorites to look for larger scale heterogeneity.

Mid-ocean-ridge basalts (MORBs) are depleted to different extents and our set of samples originates from the southern Atlantic ridge near Ascension Island and were collected during a cruise of the German science vessel “FS Meteor” (Möller, 2002). The lower mantle is investigated by ocean-island basalts (OIBs) and a large-igneous-province basalt (LIP) with samples from La Palma (LP basalts, Spain; Kuhlmann, 2011), Hawaii, Columbia river (BHVO-2, BCR-2; both USA), an intracontinental basalt is from the Leinetal graben near Göttingen (BB46; Germany). Upper crustal rocks are represented by an arc andesite (JA-1, Japan), a hercynian granite (G1RF, Germany), a pegmatite (MA-N, France), a greywacke and a shale (GD, TW; Germany). To constrain Ta behavior in deep time, a 3.45 Ga old granitic gneiss (AGC 351) from the Ancient Gneiss Complex, Swaziland, was also included (Kröner *et al.,* 2014). Two ore samples of the Columbite-Tantalite series were investigated that crystallized from pegmatite systems (Coltan-1, Africa; Coltan-2, Portugal). Note that LP2 Residue 1 is not a bulk sample but a La Palma basalt leached in 6N HCl prior to full digestion.

The meteorites analyzed comprise a selection of different chondrites and an achondrite from different heliocentric distances. Iron meteorites were not investigated because Ta behaves highly lithophile and is not present in sufficient amounts to be measured. The most primitive meteorites of the solar System investigated in this study belong to carbonaceous chondrite groups CV3 (Allende, NWA 3118) and CO3.2 (Kainsaz). Equilibrated ordinary chondrites are represented by the H5 El Hammami and L6 Wagon Mound. Furthermore, Howardite NWA 1914, a differentiated basaltic achondrite, presumably from asteroid Vesta, was included.

3.2.2 Reagents and sample digestion

Chemical separations were performed in the clean lab facilities at Cologne-Bonn. All reagents used were of ultrapure grade. Stocks of nitric (HNO_3), hydrochloric (HCl) and hydrofluoric acid (HF) were purified by sub-boiling distillation. The procedure was repeated for hydrofluoric and hydrochloric acids to reduce blank levels in Ta and W that can be released from the Teflon distill and storage material (Kleine *et al.,* 2004). Perchloric acid and hydrogen-peroxide used in smaller amounts were of Suprapur level. Teflon Savillex™ vials were used throughout the whole chemistry. Deionized water with ~ 18.2MΩ · cm used for acid dilution was produced by a Merck Millipore™ Milli-Q system. The chemical separation of Ta was done by AG 1-X8 anion exchange resin from Biorad®. Beforehand, the resin beads were cleaned repeatedly in deionized water and 6N HCl for several days. Columns and frits used for chemical separation consisted of polyethylene and were leached in acid before use.

All digestions were carried out in Teflon Savillex™ beakers. To ensure that beakers were free of contamination, pre-cleaning was done with 10% nitric acid, dilute inverse aqua regia, concentrated HF, and 1mM diethylene triamine pentaacetetic acid (DTPA) dissolved in 1M HCl, which complexes high field strength elements. All cleaning steps were carried out for at least 24 hours at 120 °C. Teflon beakers used for high-pressure digestion were additionally heated with DTPA in the steel-jacketed Parr™ bomb vessels prior to digestion. Digestion of powders from basaltic samples and equilibrated meteorites was conducted with a 1:1 mixture of concentrated nitric and hydrofluoric acid at 120°C for 24 to 48 hours. Samples with higher concentrations of SiO_2 were dissolved in mixtures of up to 3 parts 24M HF to one part 14M HNO_3. Primitive meteorites (carbonaceous chondrites) and terrestrial samples containing refractory minerals (e.g. zircons in granites) were put in Parr bomb vessels for up to three days at high pressure and 180 °C. This treatment shall lead to dissolution of highly refractory presolar phases that can carry extremely anomalous isotope signatures for heavy elements (Ávila *et al.,* 2012), even though elevated concentrations of Ta have not yet been reported in presolar grains. However, full digestion of silicon carbides, nanodiamonds and graphites cannot be guaranteed using this protocol. Precipitated secondary fluorides were dissolved by repeated drying in concentrated HNO_3. In case of Ca- and Mg-rich samples, $HClO_4$ was used for complete fluoride dissolution. Leftover perchloric acid was driven off by repeated drying down in HCl. Subsequently, the samples were transformed in chloride form and brought into solution in 1M HCl prior to of the chemical separation.

Sample sizes varied with measured or estimated Ta contents of the samples. Only a few mg were necessary for ore minerals and the MA-N pegmatite standard. *Ca.* 100-200mg of OIBs, intraplate basalts and felsic rocks generally were weighed in. MORBs, an arc andesite, and the bulk meteorites contained the lowest Ta concentrations and were digested in larger amounts of 1 to 2g.

For measurements, an Ames Laboratory pure metal standard prepared in 1999 at Münster (Weyer *et al.,* 2002) was used as the terrestrial in-house reference solution. Furthermore, an Alfa Aesar Specpure® plasma standard solution (LOT 15024103) of Ta was also used as reference in the beginning of the study. Ytterbium and Re doping for external mass bias correction was performed with Alfa Aesar Specpure® plasma standard solutions (LOT 71-064667L for Yb, 71-071361B for Re).

3.2.3 Elemental separation

The chemical treatment to purify Ta from the remaining rock matrix is based on the separation scheme published by Münker *et al.* (2001) and Weyer *et al.* (2002). The separation is done in two steps with 4ml and 1ml of AG 1-X8 anion exchange resin (Table 3.1). In case of samples with very low abundances, the resin volume of the second stage was further reduced to 0.25ml and the acid volumes were adjusted accordingly in order to reduce acid blanks of Hf and elution of organics from the resin. The resin in both stages was cleaned with four resin volumes (rv) each of DTPA, 3M HNO_3, 6M HNO_3/ 0.2M HF and 6M HNO_3/ 0.2M HF/ 1% H_2O_2 before use. At the beginning of the project, the samples were taken up in 1M HCl/ 0.5M HF before the first stage, which caused secondary precipitation of fluorides. The solution could be loaded after centrifuging. Rinsing of the fluorides in a second loading step took up remnants of Ta in interstitial solution. Co-precipitation of Ta with the fluorides was not observed, consistent with results from Tanaka *et al.* (2003).

The changes compared to the published protocols were the reduction in resin and acid amounts in the clean-up step, as well as reduced acid strengths. This is necessary to further decrease the blank of isobarically interfering Hf, which by then was mainly controlled by the acid purity. The clean-up was sometimes repeated for meteorite samples. Our anion exchange chromatography procedure is able to efficiently separate interfering Hf and W from Ta. Larger samples were split to about 400 to 500mg to prevent overloading of the resin. In case of gram-sized samples, the HFSE were first eluted as anionic complexes in 1M HCl/ 0.1M HF from cation resin (Biorad® AG 50W, 100-200 mesh) to allow separation from major elements (Patchett and Tatsumoto, 1981; Elfers *et al.*, in review). The continued HFSE separation on the anion resin was conducted as described above. An advantage of the additional cation resin step is the prevention of secondary fluoride formation before loading on stage 1, as Ca and Mg are not present anymore.

After stage 1, Ta cuts were dried down at 120°C and re-evaporated up to five times in 9:1 14M HNO_3 : 30% H_2O_2. A further peroxide step was repeated prior to measurement with a small amount of nitric acid and H_2O_2 added. This step reduced residual organics from both the (meteorite) matrices and ion exchange resins, which can cause unspecified isobaric molecules during mass spectrometry (see chapter 3.2.4.3). The final separate was taken up in 0.56M HNO_3/ 0.24M HF for

measurements. Fractionation on the column was not observed because almost all Ta quantitatively elutes with yields of more than 95% with our protocol.

Table 3.1 Ta separation scheme. Volumes of acids are given in resin volumes (rv). Stage 2 was reduced to a resin volume of 0.25ml for samples of low abundance. Resin cleaning was performed with 4 rv each of DTPA, 3M HNO_3, 6N HNO_3/ 0.2M HF and 6M HNO_3/ 0.2N HF/ 1% H_2O_2 before and after chemistry.

Step	Reagent	Resin volumes
Stage 1 (4ml) anion exchange resin, Biorad AG 1-X8 (100-200 mesh)		
Equilibrate	0.5M HCl/ 0.5M HF	~ 2rv
Load I	1M HCl/ 0.5M HF	1.25rv
Load II	0.5M HCl/ 0.5M HF	1.25rv (fluoride precipitate rinse solution)
Rinse I	0.5M HCl/ 0.5M HF	2.5rv
Rinse II	0.5mM HCl/ 0.5mM HF	3x 0.75rv
HFSE (Ti, Zr, Nb, Mo, Hf, W)	6M HNO_3/ 0.2M HF	2x 1.75rv
Ta	6M HNO_3/ 0.2M HF/ 1% H_2O_2	2x 1.75rv
Stage 2 (1ml) anion exchange resin, Biorad AG 1-X8 (100-200 mesh)		
Equilibrate	2M HF	~ 2rv
Load	2M HF	0.5rv
Rinse HFSE	3M HNO_3/ 0.2M HF	4x 1rv
Ta	3M HNO_3/ 0.2M HF/ 1% H_2O_2	3x 1rv

Blank levels in Ta ranged from 35 to 200pg with a mean of 100pg measured in different sessions at both instruments. This is slightly higher than expected from Münker *et al.* (2001). The probable cause is the use of perchloric acid to dissolve fluorides after digestion of larger sample volumes and the digestion of larger sample amounts in general. Perchloric acid can show elevated HFSE concentrations and was not further purified by sub-boiling distillation. Nonetheless, sample isotope ratios were close to values of the standard solutions, so that moderate blank levels with terrestrial isotope composition do not compromise sample measurements having more than 100 times the blank concentration, making any blank corrections unnecessary.

3.2.4 Mass spectrometry

Data were obtained using a Thermo Scientific Neptune^{TM} equipped with a Plus interface at the joint Cologne-Bonn facilitiy and at a Neptune Plus^{TM} at Thermo Scientific, Bremen. Thirteen individual sessions were run between December 2013 and June 2016 with five sessions using the 10^{13} Ω Faraday amplifiers taking place in Bremen in from June 2014 to June 2016.

3.2.4.1 Measurement protocol

For highest sensitivity, a high transmission interface was used with X-skimmer and Jet sample cones in combination with a Cetac Aridus^{TM} desolvation system. Solutions were aspired in 0.56M HNO_3/ 0.24M HF using MicroFlow PFA nebulizers at uptake rates of 100µl/min. Tantalum-180 and ^{181}Ta signals were collected for 120 x 4.2s with 10^{12}Ω and 10^{10}Ω amplifier resistors at Cologne-Bonn and for 60 x 8.4s with 10^{13}Ω and 10^{11}Ω amplifier resistors at Bremen, respectively. For monitoring of the crucial ^{180}Hf interference, the ^{178}Hf signal was also collected with a second 10^{12}Ω amplifier at Cologne-Bonn or a 10^{13}Ω amplifier at Bremen. Further interference monitors ^{179}Hf and ^{183}W, and the Yb isotopes between masses 171 and 174 were measured with standard 10^{11}Ω amplifier resistors. An Alfa Aesar Specpure® Yb solution was admixed to the Ta standard and sample solutions for external mass bias correction using the exponential law (Russell *et al.,* 1978). Rhenium was tested as a means for correction of mass discrimination and used for some sample measurements but was finally rejected due to inaccuracies in corrections evident from offsets in single standard measurements. Tantalum isotope ratios were calculated relative to ^{173}Yb/^{171}Yb = 1.12489 given by Albalat *et al.* (2012). The protocol for mass-spectrometry is described in detail in chapter 2.2.1.

The ^{180}Ta/^{181}Ta data are reported as ε-values, that is $\varepsilon^{180}Ta = (R_{sample}/R_{standard}) - 1) \times 10^4$ where R denotes the measured ^{180}Ta/^{181}Ta ratio of the sample and the bracketing standards. An AMES pure metal standard is used (Weyer *et al.,* 2002) as a reference solution, which is indistinguishable from Alfa Aesar and Merck standard solutions (chapter 2.3.1). In contrast to many other stable isotope studies, ^{180}Ta is put in the numerator, opposite to common notation with the lighter isotope being in the denominator. The exceptional properties of ^{180}Ta and assumed preference for mass-independent effects (higher neutron capture cross section, susceptibility to irradiation destruction, and exceptional nucleosynthesis) rather suggest a focus on this isotope, whereas stable isotope fractionation is inferred to be limited.

The tailing contribution from large ^{181}Ta on low abundance ^{180}Ta is about 2.5% and mostly depends on the analyzer vacuum in the detector part of the instrument (see chapter 2.3.3). During measurements, detector vacuum conditions are not completely stable and induce a drift in measured

absolute Ta ratios. However, this shift is small over typical measurement intervals, allowing correcting for it over the course of a session. Thus, bracketing of samples by standards is sufficient to obtain reliable results and external reproducibility is given as the deviations of standards relative to a linear or polynomial fit through the dataset of the session.

3.2.4.2 Correction of isobaric interferences

The minor isotope ^{180}Ta is superimposed by atomic interferences from ^{180}Hf (relative molar abundance 35.08%; Berglund and Wieser, 2011) and ^{180}W (relative abundance 0.119 %; Peters *et al.,* 2015). Hafnium-180 is the most abundant Hf isotope and even tiniest Hf contamination results in pronounced corrections in the percent range on the measured ^{180}Ta/^{181}Ta ratio. In our study, isobaric interferences on ^{180}Ta were corrected using ^{180}Hf/^{178}Hf = 1.2863, ^{180}Hf/^{179}Hf = 2.5753, and ^{180}W/^{183}W = 0.008304, which are based on long-term measured isotope compositions in-house (Peters *et al.,* 2015). Regular verifications of the correction values with Hf-doped standards did not reveal any shift over time. The raw interference correction ratios for Hf and W were artificially biased with the exponential law and the fractionation factor determined from ^{171}Yb/^{173}Yb or ^{187}Re/^{185}Re in the same measurement cycle and then subtracted from the raw mass 180 to mass 181 ratio before applying the mass bias correction to Ta. Notably, the use of both Yb and Re admixed to the Ta measurement solution does result in erroneous Re-corrected data as ^{171}Yb^{16}O molecules are interfering on ^{187}Re. Thus, an approach using both elements for correction to overcome either different mass bias behaviors or glitches in single measurements is not possible. The very small interference from ^{174}Hf on ^{174}Yb was negligible and resulted in indistinguishable Ta isotope ratios compared to other Yb ratios used for mass bias correction. The same holds true for the interference from ^{187}Os on ^{187}Re in the method with Re external normalization.

To test the Ta protocol for tolerance against W and Hf contamination, Ta standard solutions were artificially doped with increasing amounts of W and Hf and were measured for their Ta isotope compositions (Fig. 3.1). Measurement protocols at Bremen as well as Cologne-Bonn could cope with up to $8 \cdot 10^{-6}$ of ^{178}Hf/^{181}Ta at 40V on ^{181}Ta (*i.e.*, an intensity of $4 \cdot 10^{-10}$A). Generally, samples measured at lower intensity and, therefore, lower precision could deal with higher relative Hf/Ta contaminations. Overall, contaminations of up to 0.5fg/g Hf were able to be corrected for, independently of the Ta being available in the sample solutions. However, some samples with low Ta concentrations and uncommon matrices (meteorites), did fail the threshold of $8 \cdot 10^{-6}$ of ^{178}Hf/^{181}Ta. Sessions with meteorite samples were accompanied by Hf doped standards, for which the negative deviation in resulting ^{180}Ta/^{181}Ta is linearly correlated with the monitoring ratio ^{178}Hf/^{181}Ta. This correlation is used to subtract the overcorrection of Hf within the bounds of the doped standards up

to $3 \cdot 10^{-5}$ of $^{178}Hf/^{181}Ta$. In those cases, internal precision of the sample was propagated with the uncertainty of the linear fit of the Hf-doped standards.

Test measurements with admixed Re used for the mass bias correction could cope with higher $^{178}Hf/^{181}Ta$ ratios of up to $8 \cdot 10^{-5}$, which presumably is due to a more similar instrumental mass bias behavior of Re and Hf compared to Yb and Hf (Fig. 3.1). In all measurements, the isobaric interference from much less abundant ^{180}W did not pose larger difficulties and could be corrected for more than 0.003 of $^{183}W/^{181}Ta$. Usually, $^{183}W/^{181}Ta$ were below $5 \cdot 10^{-5}$ after ion exchange separation. Potential nucleosynthetic anomalies in meteorites were of no concern for interference corrections as, firstly, all other elements were separated from Ta and contaminations were mostly due to terrestrial acid blanks, and, secondly, the precision achieved on monitoring ratios was much lower than any possible anomaly.

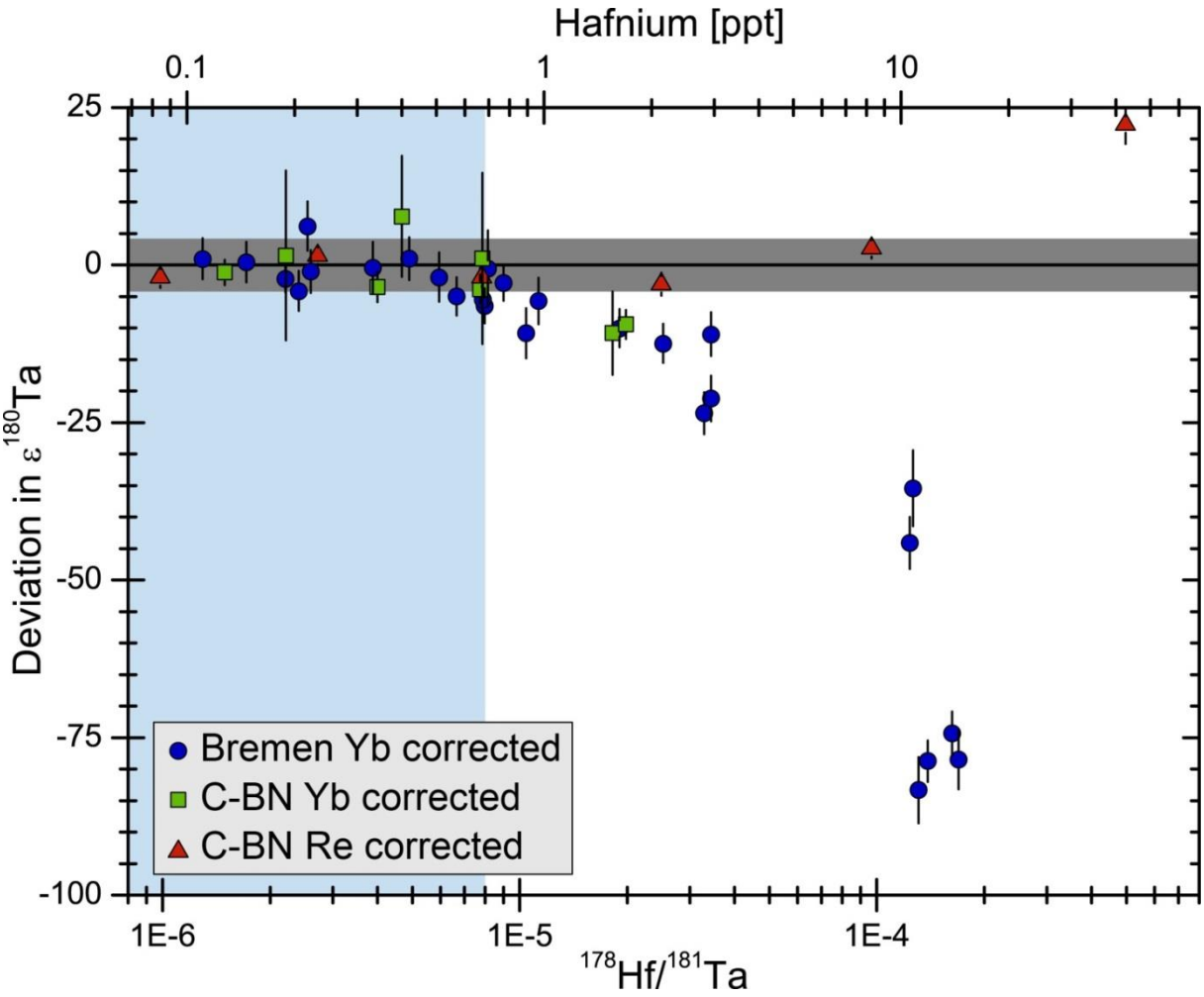

Fig. 3.1 $\varepsilon^{180}Ta$ against $^{178}Hf/^{181}Ta$ ratio of doped standards. Data for Hf-doped standard solutions were collected in several sessions both at Bremen (blue circles) and Cologne-Bonn (C-BN, green squares) using Yb as a means to correct for mass discrimination. Red triangles indicate the data using Re for mass bias correction obtained at Cologne-Bonn. The upper scale bar denotes the Hafnium concentration in solutions measured at Bremen under typical conditions. The grey bar indicates the typical external reproducibility at Bremen. Hafnium

isobaric contamination can be corrected up to $8 \cdot 10^{-6}$ of $^{178}Hf/^{181}Ta$ using admixed Yb for mass bias correction, as indicated by the blue field. The correction with admixed Re works until $8 \cdot 10^{-5}$ of $^{178}Hf/^{181}Ta$. Deviation off the expected value at higher Hf follows a linear trend in a session. Note the logarithmic scale for $^{178}Hf/^{181}Ta$ and Hf concentration.

3.2.4.3 Evaluation of matrix effects, fractionation and molecular interferences

There are several effects beside isobaric elemental interferences that can potentially affect the accuracy and precision of measurements in MC-ICP-MS. Unknown molecular interferences can pose a difficulty, especially on low-intensity ion beams like the monitoring masses of Hf and W. Another problem might arise from lower mass elements that were insufficiently separated by the chemistry, leading to different mass bias behavior of the element to be analyzed (*e.g.*, Zr in Hf measurements; Peters *et al.,* 2015). To test for such effects, Ta standard solutions were measured with 100ng/g of doped Titanium, Zr, Nb, or Mo (yielding a 1:1 Ta: element ratio). No deviations in their Ta isotope ratios were visible. Furthermore, a purified Ta cut from a terrestrial basalt did only contain residual elements at negligibly low concentration below the pg/g level. The robustness of the separation protocol was further corroborated by the Nb-rich Columbite ore minerals, which were purified to Nb/Ta element ratios of less than $3 \cdot 10^{-5}$.

An important issue is the presence of organics, either from meteorite matrices or residues from the organic ion exchange resin (Holst *et al.,* 2015). Especially the large correction of the Hf interference amplifies residual signals on mass 178. A molecular, presumably organic species was observed for some low concentrated samples on mass 178 by comparing the two Hf monitors. To illustrate the necessity of accurate corrections, the effect of a molecular interference on ^{178}Hf is calculated here. An additional signal of only 1µV on mass 178 during a run with 42V on ^{181}Ta causes an effect of *ca.* -2.5ε in the Ta isotope ratio due to an inappropriate interference correction. To identify runs with erroneous Hf signal, the theoretical $^{178}Hf/^{181}Ta$ monitoring ratio was calculated from $^{179}Hf/^{181}Ta$ by applying the accepted value of 2.003 (Berglund and Wieser, 2011). By comparing the measured from the theoretical $^{178}Hf/^{181}Ta$, a resolvable positive deviation in measured $^{178}Hf/^{181}Ta$ offset to standards was interpreted as an additional species on mass 178. This effect is independent of tailing or mass bias correction. Most of the terrestrial samples do not show any effects of molecular interferences, as Ta isotope ratios calculated from both Hf interference monitors agree within error. Importantly, erroneous $\varepsilon^{180}Ta$ calculated with ^{179}Hf as interference monitor were not observed, in cases where the ^{178}Hf monitor failed. Initial tests identified minor interferences on mass 180 after elution from anion resin at the beginning of the project. Positive deviations on mass 180 could be overcome by reduced nitric acid strengths in the eluting step (3N HNO_3 instead of 6N HNO_3).

Therefore, we exclude effects of molecular interferences on mass 179 and 180 and use ^{179}Hf as a monitor in those cases where 178 fails.

Some evidence for molecular interferences originating from the Biorad® AG 50W cation resin also arose from tests for artificial isotope fractionation during chemical separation, where *ca.* 50mg Ta were loaded on both cation and anion resins (Fig. 3.2). Tantalum was eluted in 1 ml steps, dried down and was directly transferred into measurement solution without any peroxide treatment to remove organics. Data corrected with the ^{179}Hf monitor did not show any deviation in Ta isotope ratios. Some of the ^{178}Hf corrected data, however, yielded negative ε^{180}Ta, *i.e.*, an overcorrection due to an artificial Hf interference. This effect was especially visible on cation resin, where the least concentrated last steps were only little diluted prior to measurement. Thus, a correlation between organics from the resin and the apparent Hf interference is evident that may influence measurements of small sample sizes. Importantly, artificial stable isotope fractionation on cation and anion resins is insignificant, which excludes the resin as a potential source of artefacts. Resin organics affecting Ta isotope measurements, however, can be identified by negative deviations in ^{178}Hf-corrected data. In these cases, the ^{179}Hf interference monitor can be reliably used for Hf interference corrections. Reprocessing and repeated dry downs in a nitric acid-peroxide mixture of the leftover cuts significantly reduced the effects of organics. The chemical separation protocol was therefore adjusted accordingly, with more rigorous drying in concentrated HNO_3 and H_2O_2 before the clean-up. The final elution prior to measurements was then done with smaller resin volumes for critical samples. The last dry-down step with nitric acid-peroxide solution prior to measurement was only performed once to avoid elevated Hf blanks. Additionally, measurement vials were leached prior to measurements with dilute HF/ HNO_3 to avoid release of organics after loading with sample solutions.

In an approach to track down possible interfering molecular species, a full Ta separation was run with blanks only and different final dry down protocols. The solutions were measured with an ELEMENT XR SF-IC-MS instrument in Bonn for their count rates in the mass range from 177 to 183. Apparent Hf ratios were compared to the measured ratios from a 1ng/g AMES Hf solution. Even though low concentrated solutions did not yield good counting statistics, the better consistency with natural Hf values was achieved with higher amounts of oxidizing agents used after separation like concentrated nitric acid mixed with hydrogen peroxide (9:1) or perchloric acid. Tests with the same solutions in high resolution mode did not result in sufficient count rates to identify low intensity molecular species.

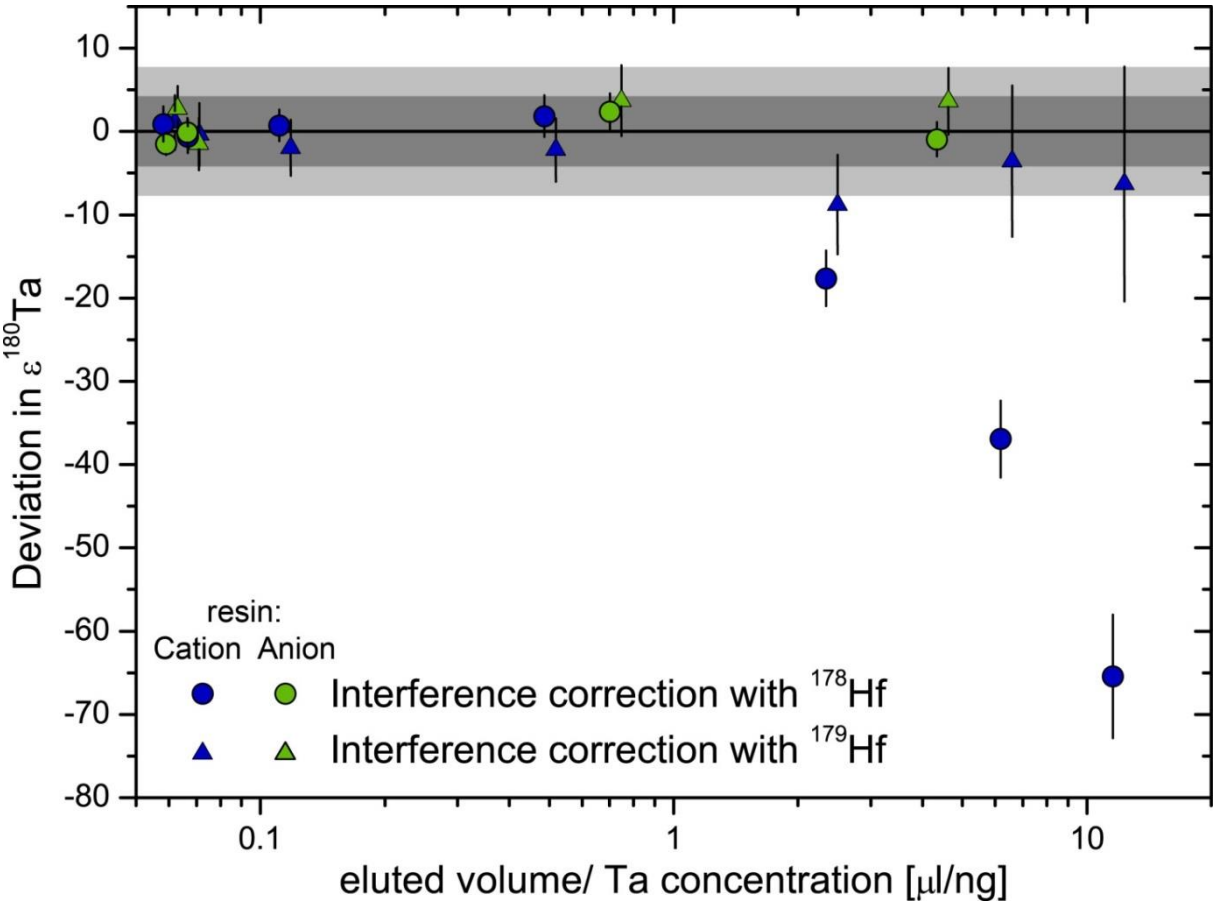

Fig. 3.2 Results of an **e**xperiment to constrain effects of stable isotope fractionation on ion exchange resin and influence of eluted organics. The ε^{180}Ta of the prior unfractionated Ta standard loaded on the resin is plotted against the eluted volume normalized to its Ta content Shown are the ^{178}Hf and ^{179}Hf interference corrected data obtained in the same run. The ratio from the eluted acid volume from the resin divided by the amount of Ta in the respective cut is used as a measure of the relative content of organics. The dark grey bar indicates the external reproducibility for correction with ^{178}Hf whereas the light grey bar shows the somewhat worse reproducibility for ^{179}Hf. The lower the content of Ta in the eluent, the stronger is the influence of a molecular interference on mass 178, leading to an overcorrection for apparent Hf. Data corrected with the ^{179}Hf monitor are unaffected but lack the superior precision of the mass ^{178}Hf corrected data. The effect was only observed after use of cation resin, whereas the anion resin method with reduced acid strengths to 3M HNO_3/ 0.2M HF is reliable. Note that symbols of ^{179}Hf corrected data are shifted to the right for clarity.

Means to avoid molecular interferences in mass 180 range were previously discussed (Holst *et al.,* 2015) but these are not directly applicable for Ta isotope measurements Repeated treatment of the final eluent with concentrated HNO_3/ H_2O_2 or use of $HClO_4$ as suggested by Holst *et al.* (2015) is not an option after the clean-up step, because this would introduce too much Hf from acid blanks. Use of the mass spectrometer's high resolution mode to circumvent possible interferences, as proposed by Holst *et al.* (2015), or the use of normal cones is also not desirable, as the signal intensity would be too low in particular for extraterrestrial samples. For higher concentrated critical

terrestrial samples like organic-rich shales, however, use of the medium resolution mode is of advantage for two reasons. Firstly, measuring on the low-mass side of the peak should avoid some of the potential influence of organic molecules having slightly higher masses and, secondly, the tail and vacuum drift are significantly reduced, leading to more stable measurement conditions and better reproducibility (see chapter 2.3.3).

Of further importance are the cleanliness of the Aridus^{TM} desolvator and the mass spectrometer. A properly back-washed nebulizer, a spray chamber rinsed with dilute HF-HNO_3, reasonable wash-out times, and a Ta separation with reduced resin and acid volumes are needed to keep the Hf background below the relatively low threshold and to avoid matrix effects. Additionally, the membrane of the Aridus^{TM} and the instrument should be conditioned with the measurement solution for some days, especially when not regularly exposed to dilute HF. Unexpected mobilization of elements from the sample introduction system, also due to slightly different compositions of sample solutions, might cause changing backgrounds in the mass spectrometer, including relative differences in mass bias behavior of elements or changing contributions of (organic) molecular interferences. To summarize, the chemical treatment and absolute purity of sample solutions increasingly becomes the limiting factor for sufficiently precise isotope measurements.

3.3 RESULTS

The typical external reproducibility obtained with Ta standard solutions is 4.2ε for ~25ng and 4.0ε for ~100ng at Bremen and Cologne-Bonn, respectively. The external reproducibility represents two standard deviations of the standards relative to neighboring standards of same intensity in a session or the deviation to the linear fit used to accommodate drift. To test the reliability including the chemical separation, terrestrial basalts from La Palma and a Ta ore mineral from Portugal were measured in every session. The average composition and long term reproducibility (2σ) obtained were ε^{180}Ta = +1.7±5.5ε for LP1, +1.8±4.6ε for LP2 Res 1 and -1.8±5.9ε for Coltan-2 (weighted mean with 2 SD; n = 10, 16 and 12, respectively; Fig. 3; Table 3.2). Some data reported with an interference correction via the ^{179}Hf monitor yielded an external reproducibility of only ±7.8ε. The reason for the comparatively lower reproducibility is the use of an amplifier with a 10^{11} Ω resistor at Cologne-Bonn and a 10^{12} Ω resistor at Bremen on mass 179, which does not provide sufficient precision for obtaining highest quality data.

Tantalum isotope ratios in all geological samples and bulk meteorites are indistinguishable from our terrestrial AMES pure metal Ta standard (Figs. 3.3, 3.4; Tables 3.2, 3.3). The terrestrial samples do not show systematic groupings corresponding to tectonic settings or major element

chemistry. Notably, Ta sampled from the deeper Earth by mantle plumes or from deep time by Archean rocks is indistinguishable from younger crustal rocks within our precision achieved. Several meteorite groups from more primitive carbonaceous, over ordinary chondrites to a differentiated achondrite also agree within error with the terrestrial standard, resulting in a bulk solar system value of ε^{180}Ta = -2.2±7.4. Generally, the meteorites are not as precisely measured as the terrestrial rocks, because of (i) the scarcity of material, (ii) the use of ^{179}Hf as interference monitor, and (iii) lacking repeated measurements.

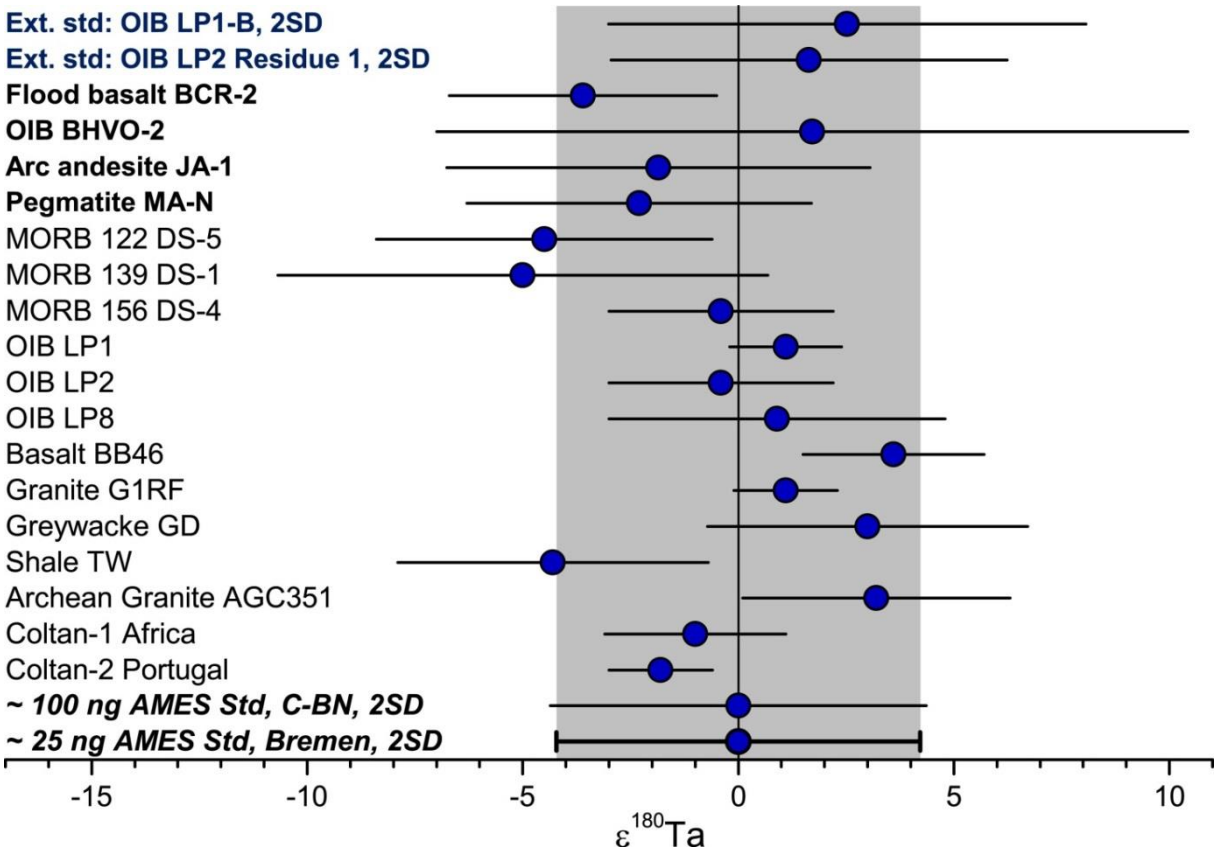

Fig. 3.3 Weighted means of all terrestrial materials. Error bars are 95% confidence intervals for more than three measurements calculated with IsoPlot 4.11 (Ludwig 2003). Fewer measurements per sample are mirrored by somewhat poorer external reproducibility. The shaded area represents the typical external reproducibility for measurements of *ca.* 25ng Ta at Bremen. No terrestrial material is resolvable from the Ta AMES metal standard. LP1-B and LP2 Res 1 leaching residue (see above) were used as in-house external standards to test the long-term reproducibility and are shown with 2SD uncertainty.

Some terrestrial data scatter slightly outside the external reproducibility, as evident from a higher 2 S.D. for repeated measurement than stated for the standards. This is caused by non-ideal measurement conditions during some sessions, where the instrument was not sufficiently clean for highest-precision applications. In some cases, the cones used were so eroded that vacuum drift was

not fully accounted for by the standard bracketing approach, or the sample was not concentrated enough to achieve best counting statistics. Thus, the weighted mean is generally reported for samples with repeated measurements and used further below to account for measurements with lower internal precision obtained under non-ideal conditions.

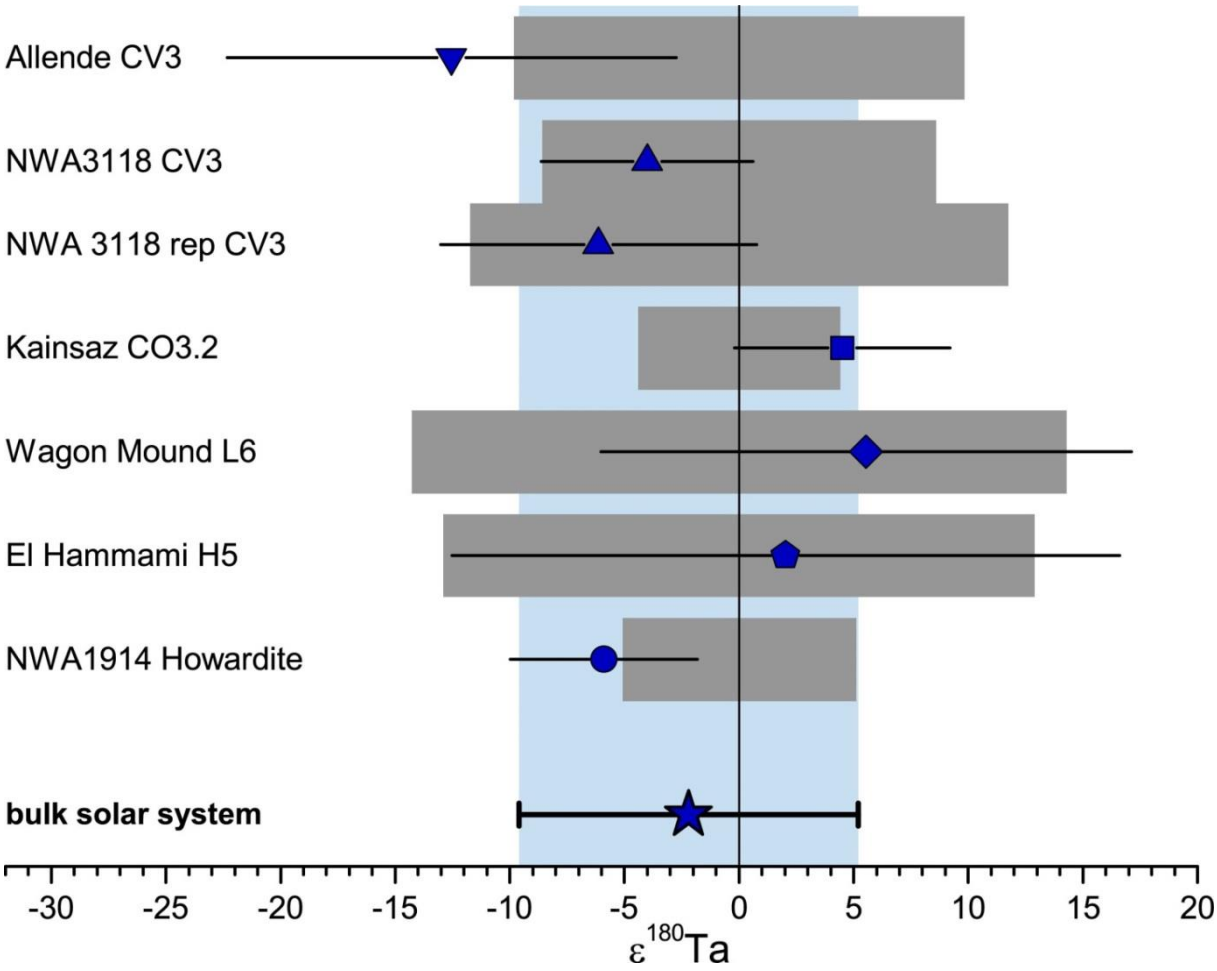

Fig. 3.4 ε^{180}Ta of bulk meteorites. Error bars give the two times relative standard error from the mean of a single measurement. The grey bars indicate the empirical external reproducibility calculated from the internal reproducibility of the measurement. A second measurement of a sample cut is indicated by "rep". All other measurements are single digestions. The calculated weighted mean of the solar system is underlain as the light blue field.

Table 3.2 Tantalum isotope data obtained the measured terrestrial and extraterrestrial samples. Shown are the means of repeated measurements as ε^{180}Ta of a sample, including the weighted means. Errors are reported as the 2 S.D. from the mean and the 95% conf. interval for samples with more than 3 measurements. Samples with only one measurement are displayed as the mean and the associated external reproducibility of the single measurement. Confidence intervals were calculated with IsoPlot 4.11. Concentration data are taken from the literature and data repositories: BCR-2, BHVO-2, JA-1, MA-N are preferred or compiled values from GeoRem (Jochum *et al.,* 2005); BB46, GD, and TW are in-house standards from the Institute of Geology, Göttingen (Münker, pers. comm.); LP1 and LP8 were part of a Bachelor thesis (Kuhlmann 2011); the MORBs were investigated after a research cruise (Möller, 2002; König *et al.,* 2011); and the Archean granite is part of a data set from Kröner *et al.* 2014.

Sample	Rock type	Locality	Ta conc.	Mean	Weighted mean	Number	2 SD of means or 2 RSE	95% conf. int.
			µg/g	ε^{180}Ta	ε^{180}Ta	N	± ε	± ε
Terrestrials								
LP1-B extStd	Ocean island basalt	La Palma, Spain		2.5	1.7	10	5.5	
LP2 Res 1 extStd	Leached ocean island basalt	La Palma, Spain		1.6	1.8	16	4.6	
BCR-2	Continental flood basalt	Oregon, USA	0.785	-3.8	-3.6	5	5.1	3.1
BHVO-2	Ocean island basalt	Hawaii, USA	1.154	1.7		1	8.7	
JA-1	Arc andesite	Japan	0.098	-1.9		1	4.9	
MA-N	Pegmatite	France	290	-2.0	-2.3	6	8.0	4.0
MORB 122 DS-5	Mid-ocean ridge basalt	South Atlantic	0.196	-4.5	-4.5	2	3.9	2.0
MORB 139 DS-1	Mid-ocean ridge basalt	South Atlantic	0.21	-5.9	-5.0	2	5.7	2.8
MORB 156 DS-4	Mid-ocean ridge basalt	South Atlantic	0.23	-1.8	-0.4	4	4.4	2.6
LP1 all	Ocean island basalt	La Palma, Spain	5.764	1.8	1.1	15	5.1	1.3
LP2	Ocean island basalt	La Palma, Spain		-0.6	-0.4	4	3.5	2.6
LP8	Ocean island basalt	La Palma, Spain	4.83	1.0	0.9	6	9.2	3.9
BB46	Intraplate basalt	Leine-Graben, Germany	3.7	4.9	3.6	7	5.7	2.1
G1RF	Granite	Harz, Germany		0.8	1.1	5	2.8	1.2
GD	Greywacke	Harz, Germany	0.6	2.7	3.0	2	3.7	14.0
TW	Shale	Harz, Germany	1.2	-4.5	-4.3	7	9.0	3.6
AGC351	Archean granite	Swaziland	1.263	3.3	3.2	4	3.6	3.1
Coltan-1	Columbite-Tantalite mineral	Africa	~ wt.%	-1.0	-1.0	7	4.4	2.1
Coltan-2	Columbite-Tantalite mineral	Portugal	~ wt.%	-0.6	-1.8	12	5.9	1.2

Table 3.3 Tantalum isotope data for bulk meteorites measured in this study. Meteorites were just measured once due to the scarcity of sample material. In case of NWA 3118, a replicate is marked with "rep". The uncertainty of individual measurements is given as the 2 standard error and the external reproducibility is calculated empirically from the respective internal precision. The solar system mean was calculated with IsoPlot 4.11 as the weighted mean from the 5 individual meteorite groups measured in this study. For comparison, the mean with associated 2SD uncertainty is also given.

Sample	Meteorite group	Mean	Uncertainty	External rep.
		ε^{180}Ta	± ε	± ε
Meteorites				
Allende	CV3	-12.5	9.8	9.8
NWA 3118	CV3	-4.0	8.3	8.6
NWA 3118 rep	CV3	-6.1	12.4	12.4
Kainsaz	CO3.2	4.5	4.7	5.9
Wagon Mound	L6	5.5	11.6	14.3
El Hammami	H5	2.0	14.6	14.6
NWA 1914	Howardite	-5.9	4.1	4.9
Weighted mean meteorite groups		-2.2	7.4	
Mean meteorite groups		-0.2	12.0	

3.4 DISCUSSION

The Ta isotope compositions of a comprehensive set of terrestrial and extraterrestrial materials were measured for the first time. In the following, we assess the possibility of the new method for application to problems in geo- and cosmochemistry.

3.4.1 Potential of stable isotope fractionation in igneous systems

Tantalum isotope fractionation in natural materials is not resolvable from standard solutions at the current level of precision (Table 3.2; Fig. 3.3). The data set comprising diverse terrestrial settings is particular aimed at reporting Ta isotope compositions of internationally accepted reference materials and to identify potential isotope fractionation in environments where distinct geological processes have operated to redistribute HFSE in general and Ta in particular. Thus, by identifying the extent of Ta isotope fractionation on the Earth allows putting upper limits on mass dependent isotope effects, which also apply to early solar system materials, in addition to potential nucleosynthetic or irradiation-induced isotope anomalies.

The MORB samples of our study were selected from one specific region (Mid Atlantic Ridge) where different degrees of mantle source depletions are present, as expressed by Zr/Nb ratios from 13 to 29 (Möller, 2002; König *et al.,* 2011). Zirconium is less incompatible during mantle melting than Nb, the geochemical twin of Ta (Weyer *et al.,* 2003). Thus, samples with highest Zr/Nb ratios should sample the most depleted MORB mantle source and could reveal progressive Ta isotope fractionation. However, no such trend in the MORB data is visible (Fig. 3.5). Basalts with higher degrees of melt depletion would have been desirable, but such high Zr/Nb samples were lacking the sufficient amounts of Ta necessary for precise isotope measurements. Arc settings associated with subduction zones are characterized by negative elemental anomalies in Nb and Ta trace element patterns, which is not yet fully understood. Sequestering in rutile (Brenan *et al.,* 1994) or amphibole (Ionov and Hofmann, 1995) in the subducting slab or the sub-arc mantle are possible explanations beside the intrinsically low solubility of Nb and Ta in aqueous fluids (McCulloch and Gamble, 1991; Pearce and Peate, 1995). The Ta isotope compositions of our arc samples measured do not vary and, thus, there is no evidence for Ta isotope fractionation during sub-arc processes. Ocean island basalts and LIP samples are thought to tap deeper compartments of the mantle and also indicate a relatively homogeneous lower mantle composition in terms of Ta isotope ratios. The Archean gneiss AGC 351 (3.45Ga old; Kröner *et al.,* 2014) indicates no significant fractionation of Ta isotopes on Earth in the crust-mantle system over geologic time scales. The absence of resolvable differences in Ta stable isotope compositions between the mantle and the oceanic crust seem reasonable, as Ta is efficiently transferred into the melt during partial melting and is to a large part recycled back into the mantle by subduction. These observations are generally in accord with expectations of limited stable isotope fractionation in high temperature magmatic environments (Urey 1947).

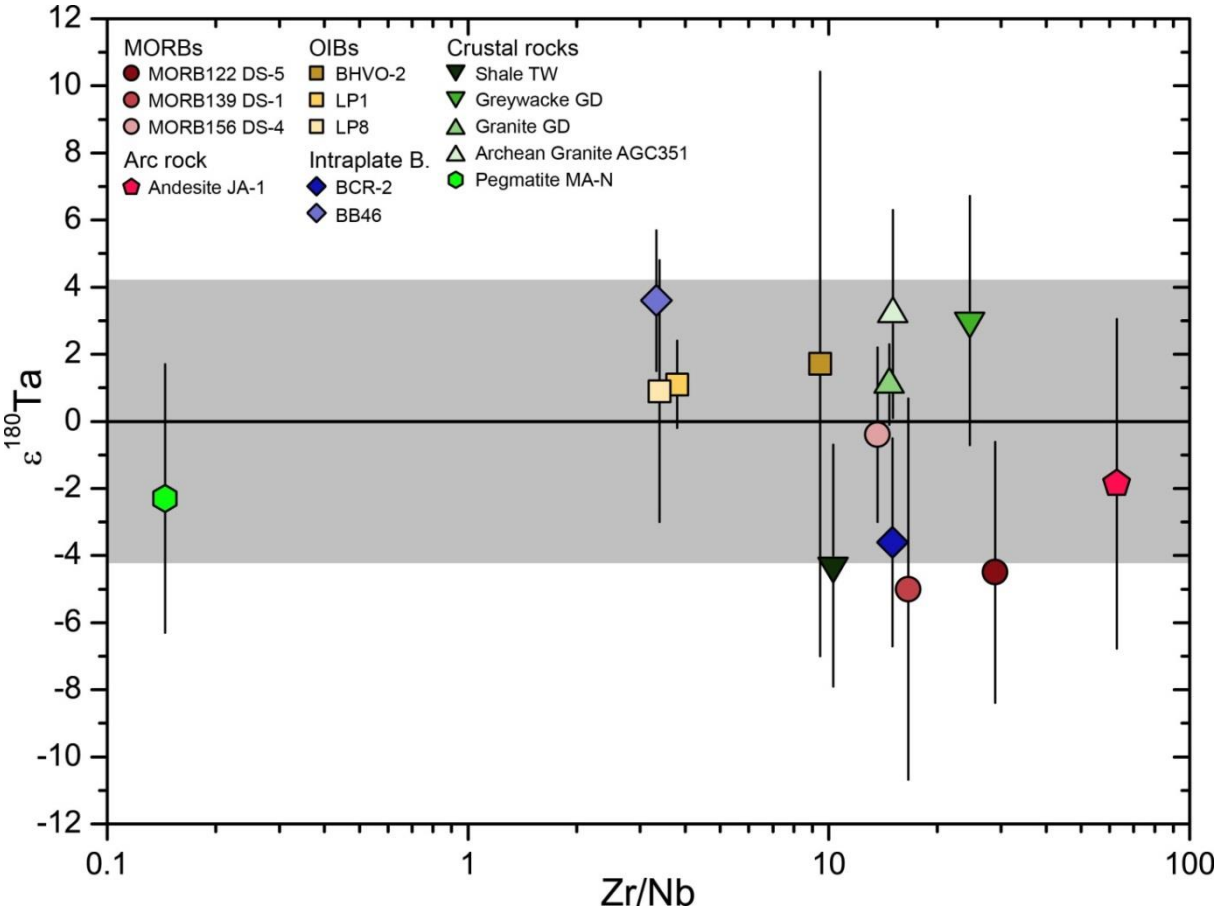

Fig. 3.5 ε^{180}Ta versus Zr/Nb ratios of terrestrial rocks. The errors are given as the 95% confidence interval and the grey band indicates the typical external reproducibility. The Zr and Nb trace element data references are given in the caption of Table 3.1.

Investigation of rocks and minerals from evolved magmatic system are suited to obtain an estimate on igneous Ta isotope fractionation at lower temperature. In general, pegmatites can show the largest mass dependent isotope fractionation in magmatic systems due to their highly evolved chemistry and their relatively low temperatures of formation. A typical example is the light element B, which exhibits differences of more than 8 per mil in a single pegmatite (Siegel *et al.*, 2016). Tantalum is concentrated in fluxed granitic melts and undergoes fractional crystallization in latest pegmatite stages (Linnen *et al.,* 2012). This is, for instance, seen in Nb/Ta fractionation during crystallization of Columbite-Tantalite (Fe, Mn)(Nb, Ta)$_2$O$_6$ series minerals inside pegmatite bodies, where Nb is less soluble than Ta and crystallizes first (Bartels *et al.,* 2010). Tantalum-rich mineral crystallization can be controlled by the availability of divalent cations (Ca, Mn, Fe) needed to form such minerals (Linnen *et al.,* 2012). This results in intergrowths of microlite ([Ca,Na)$_2$Ta$_2$O$_6$[O,OH,F]), wodginite (MnSnTa$_2$O$_8$) and Columbite-Tantalite and this assemblage might be a potential source for fractionation between crystallizing minerals and residual Ta in the corresponding melts or fluids. A more important pathway for possible isotope fractionation in late-stage magmatic systems is the

difference in bonding environment of Ta^{5+} ions between the fluxed melt and the minerals. While the Ta-bearing minerals are all oxides, the most important complexing agent of Ta is assumed to be fluorine. When F^- is bound in micas, the melts may get supersaturated in Ta and start to precipitate Ta ore minerals (Demartis *et al.,* 2014). Late magmatic Ta isotope fractionation, however, is not identified in our limited data set with only one pegmatite and two less evolved Ta-poor Columbite minerals, while the crystallization sequence of a pegmatite can cover the full spectrum from almost pure Columbite to Tantalite within a single ore body.

Even though we are not able to resolve any differences between terrestrial samples from the bracketing standards, there is a slight co-variation between the Ta isotope ratios (95% confidence interval of the samples) and the Ta concentrations in the data set, disregarding fractionated crustal materials (Fig. 3.6). The same trend is present in ε^{180}Ta against Zr/Nb (Fig. 3.5). One explanation is potential artefacts, which only become important in measurements close to the present limit of precision, and lead to lower isotope ratios at lower Ta concentrations. This means that the less Ta is present in the sample cuts, the more important are contributions from potential artefacts during sample processing and measurements, as was identified above for the use of cation resin (chapter 3.2.4.3). Arguments against such increasing interferences are the Ta isotope variations in Fig. 3.6 in both positive and negative directions. Furthermore, the co-variation between isotope and concentration data is present in both the ^{178}Hf and ^{179}Hf interference corrected data, which argues against an artefact affecting the Hf interference corrections. Nonetheless, smallest degrees of fractionation during the chemical separation may also have caused positive and negative stable isotope effects, independent of the interference correction, although it is not clear why this should correlate with the sample's Ta concentrations. Hence, a likely option is a true trend in our data set that would point towards progressive Ta fractionation with melting in the Earth's rock reservoirs, especially in the depleted upper mantle reservoir. When comparing stable Ta isotope fractionation with those of elements of similar mass, Yb and W were previously shown to exhibit stable isotope fractionation of a few ε-units in magmatic system, though these effects have been assumed to reflect changes in the element's redox state (Albalat *et al.,* 2012; Breton and Quitté, 2014; Abraham *et al.,* 2015). Stable isotope fractionation of Re even ranges up to 9 ε-units difference, but this effect has been attributed to redox variation and complexation in organic matter at low temperatures (Miller *et al.,* 2015). Thus, we speculate that repeated melt extraction in the MORB mantle source might be a fractionation pathway for Ta, which could lead to progressive enrichment of heavier Ta in the depleted upper mantle (*i.e.*, negative ε^{180}Ta), as shown by the MORBs and the measured arc andesite. In this regard, Ta might be a prime example for heavy element isotope fractionation during melt depletion in the upper mantle, as it is highly incompatible and likely not controlled by dispersed accessory phases in the mantle, as it is the case for chalcophile elements. Furthermore, re-

fertilization through fluids should not influence the Ta content of the mantle, because Ta does not partition into fluids (McCulloch and Gamble, 1991; Pearce and Peate, 1995).

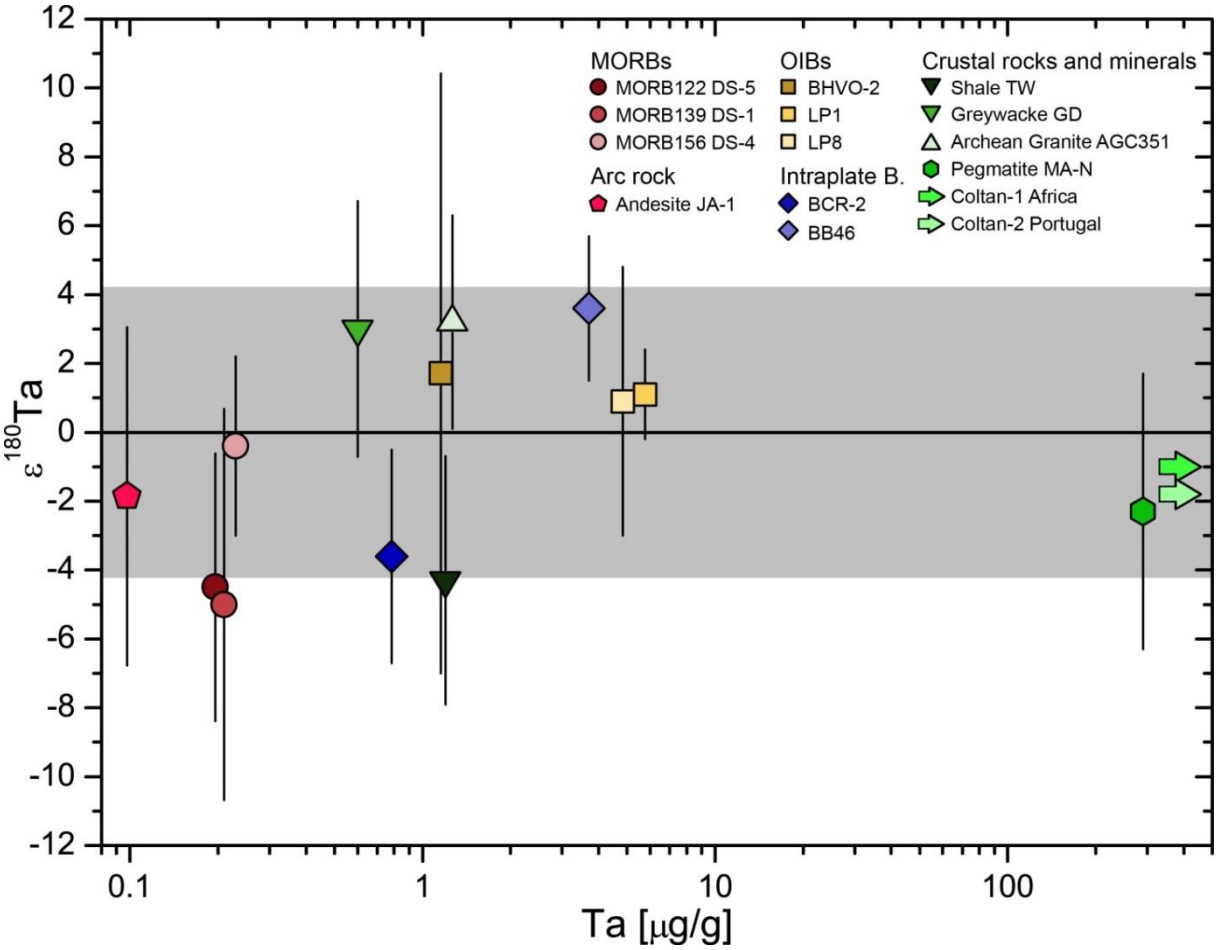

Fig. 3.6 Measured ε^{180}Ta versus Ta concentrations of terrestrial rocks. The errors are given as the 95% confidence interval and the grey band indicates the typical external reproducibility. The Ta concentration of Columbite-Tantalite minerals is not known but can be assumed from mineral stoichiometry to be at the wt% level (indicated by arrows).

In line with somewhat lower ε^{180}Ta in depleted mantle rocks, upper crustal rocks might show slightly lighter Ta isotope signatures (*i.e.*, elevated ε^{180}Ta). A possible mechanism to account for crustal effects might be splitting of the 5d orbitals of Ta in hydrous melts. It was shown by X-ray absorption near-edge spectroscopy (XANES) that the octahedral oxygen atom structure around Ta^{5+} ions becomes increasingly distorted with increasing water in peraluminous melts, changing the electronic structure of the Ta ions (Mayanovic *et al.,* 2013). This might induce nuclear field shift effects between a silicate melt and ordered mineral structures, giving rise to higher than expected stable isotope fractionation of Ta. The columbite minerals and the pegmatite rock standard do not follow the proposed trend but they might record more localized events inside the pegmatite melts

samples (Fig. 3.6). In conclusion, the extent of possible Ta isotope fractionation is hard to constrain from a nuclear physics point of view. However, stable Ta isotope fractionation might be present in terrestrial systems, but it is not yet fully resolvable at the current level of analytical precision.

3.4.2 Constraints from Ta isotopes on processes in the early solar system

The observation that Ta isotopes are homogeneous on the bulk meteorite scale allows inferences on the meteorite parent body formation region, particularly the irradiation environment in the protoplanetary disk (Table 3.3; Fig. 3.4). The bulk solar system value of ε^{180}Ta = -2.2±7.4 is indistinguishable from the terrestrial Ta isotope composition, leading to the assumption that the Ta hosted by the Earth accreted has not experienced a very different history than the Ta sequestered into meteorite parent bodies. The ordinary chondrites (here studied: H5 El Hammami and L6 Wagon Mound) are formed in the inner solar system, while carbonaceous chondrites (CV3.6 Allende, CV3 NWA 3118, CO3.2 Kainsaz) derive from the asteroid belt or beyond. In lighter elements like O, Ti, and Cr, a dichotomy was observed between carbonaceous (outer solar system) and non-carbonaceous (inner solar system) meteorites (Warren, 2011). Unfortunately, the low concentration of Ta in meteorites hampered measurements as precise as achieved for terrestrial rocks, leaving the possibility that Ta isotope variability in solar system objects might have not been resolved. In the following we discuss different processes acting in the early solar system and how they might have affected the Ta isotope inventory.

Tantalum-180 has neutron capture cross sections of *ca.* 560 barns in the thermal and a resonance integral of *ca.* 1350 barns in the epithermal energy range, whereas ^{181}Ta has capture cross sections of only 20 barns in both energy ranges (Mughabghab, 2003). Burnout effects of ^{180}Ta over ^{181}Ta can be expected in some solar system materials. In case of the Moon, burnout of ^{181}Ta is significant, where produced ^{182}Ta rapidly reacts through β-decay to ^{182}W. This effect causes artificial anomalies in radiogenic ^{182}W, which is used to constrain core formation timing of the Moon, origin of the Moon-forming giant impactor and its compositional relation to Earth (e.g. Leya *et al.,* 2003; Kleine *et al.,* 2009; Touboul *et al.*, 2015). Neutron capture effects are either not present or very low in our sample set as evident from Hf isotopes available for many of our samples (Sprung *et al.,* 2010; Peters *et al.,* 2015; Elfers *et al.*, in review). Several Hf isotopes have higher neutron capture cross sections, which do not deviate in most silicate meteorite samples. However, other solar system materials like lunar samples exposed for longer time to cosmic ray irradiation are expected to show negative anomalies of ^{180}Ta.

A recent discussion in cosmochemistry has raised the possibility of accelerated decay of excited ^{176}Lu to explain inconsistencies in the apparent ^{176}Lu decay constant (Albarède *et al.,* 2006).

This model was invoked to explain meteorite isochrons that yield significantly older apparent ages as obtained from other chronometers (Scherer *et al.*, 2001; Bizzarro *et al.*, 2003; Soderlund *et al.,* 2004). In detail, this discrepancy has been explained by early γ-irradiation event in the protosolar disc and excitation of ^{176}Lu to an intermediate nuclear state of 839 keV (Albarède *et al.,* 2006). From this excited state, the Lu can decay via lower energy isomeric levels to ^{176}Hf with a half-life of only 3.7 hours. Potential sources of irradiation would have been the active young sun or a nearby supernova. The intermediate nuclear levels of ^{176}Lu are necessary to overcome the large difference in nuclear spin between isomers. A comparable mechanism is possible for the observationally stable excited ^{180m}Ta nuclide to decay over its ground state to ^{180}Hf and ^{180}W. Intermediate states of ^{180m}Ta are present at energies 1010keV above the stable isomeric state, leading to the ground state, which then decays with a $T_{1/2}$ of 8.2 hours to ^{180}W and ^{180}Hf (Hayakawa *et al.,* 2010). Thus, ^{180}Ta/^{181}Ta may give additional constraints on the irradiation environment in the early solar system. Recent high-precision measurements of the ^{176}Lu/^{175}Lu isotope ratio in eucrites (Wimpenny *et al.,* 2013) showed that ^{176}Lu has not been depleted by early γ-irradiation. Bast *et al.* (2017) finally concluded that the discrepancy in meteorite isochrons can simply be explained by terrestrial contamination of separated mineral fractions or weathering effects. Our Ta isotope data give additional support against large-scale high-energy photon irradiation in the early solar system, at least at a magnitude sufficiently large to induce measurable isotope effects.

Another source of irradiation in the early solar system may have been higher energetic protons from the pre-T-Tauri stage sun. During accretion, strong magnetic fields are able to accelerate protons to energies sufficiently high to undergo nuclear reactions (Gounelle *et al.,* 2001), which has been proved by extant ^{10}Be that was produced by spallation in refractory calcium-aluminum-rich inclusions (CAIs; McKeegan, 2000). Bulk chondrites are not expected to have been influenced as they have formed far away from the sun shielded by the protoplanetary nebula, and after the phase of strongest accretion and heaviest solar wind. However, Vanadium isotopes show a ^{50}V excess of 8ε in chondrites relative to terrestrial materials which cannot be explained by fractionation processes like core formation. This feature was attributed to early irradiation and dispersal in inner solar system objects (Nielsen *et al.,* 2014). Tantalum-180 might be a tool to test this hypothesis as it is placed in a position of the chart of nuclides, which should not be occupied by a stable nuclide after the Mattauch isobar rule. Thus, ^{180}Ta can be produced by a proton-neutron reaction from the stable and abundant parent isotope ^{180}Hf, and it does not decay back to its parent nuclide. Additionally, ^{180}Ta is much less abundant as ^{181}Ta, making it sensitive for nucleogenic ingrowth. In contrast to the ^{50}V data, however, ^{180}Ta abundances in meteorites are not resolved from Earth. This can be interpreted in different ways. First, a different process may have operated to cause the ^{50}V overabundance on Earth or, secondly, material irradiated early in the solar system was

processed such that V isotope difference survived while Ta was homogenized again, e.g., by condensation of irradiated Ta in less resistant phases than V. Alternatively, the physical production pathways for ^{50}V and ^{180}Ta differ in some way (necessity to cross certain isomeric levels, proton reaction cross sections) that they did not effectively produce ^{180}Ta at sufficient amounts required to resolve anomalies within our measurement uncertainty.

Apart from irradiation effects, Ta can be isotopically fractionated by processes not operating on Earth. Refractory inclusions and some enstatite chondrites exhibit very low oxygen fugacities (Keil, 1968; Simon *et al.,* 2005). In those solar system materials the conditions could have been sufficiently reducing that Ta is present in a 3+ oxidation state (Cartier *et al.,* 2014). In case of redox chemical fractionation between phases, stable isotope fractionation and nuclear field shift effects may have become more pronounced and might be analytically resolvable at our level of precision, as it is observed for other high mass elements like Yb and W (Albalat *et al.,* 2012; Breton and Quitté, 2014; Abraham *et al.,* 2015). According to nuclear field shift theory, the heavier isotopes preferentially get enriched in the species with lower electron density at the nucleus, *i.e.*, fewer s-electrons (Schauble, 2007). In case of Ta, Ta^{3+} exhibits two outer-electrons (electronic configuration of [Xe] $4f^{14}$ $6s^2$), whereas Ta^{5+} has no outer s-electrons ([Xe] $4f^{14}$), which should lead to a heavier isotope composition (lower ε^{180}Ta) in the oxidized species.

Bulk meteorites are not expected to show stable isotope fractionation in Ta but components in enstatite chondrites of higher petrologic type and low oxygen fugacities below ΔIW -5 might display Ta fractionation between metal or sulfide and co-existing silicates (Cartier *et al.,* 2015). Beside the very low oxygen fugacity required for Ta redox transitions, a physical process has to operate to remove part of the Ta from the isotopically unfractionated reservoir. The easiest way is melting of the sample to separate Ta from possible Ta-bearing phases like metal or pyroxene, but enstatite chondrites did not melt as evident from unfractionated refractory element patterns (Barrat *et al.,* 2014). However, there are achondrite equivalents of enstatite chondrites, but their material available on Earth is limited. Elemental concentrations obtained from leached enstatite chondrites, showed that Nb (the geo- and cosmochemical twin of Ta) is increasingly concentrated in a sulfide phase (Barrat *et al.,* 2014). If this behavior was also applicable to Ta, this would indicate elemental redistribution of Ta already achieved during parent body metamorphism. Another open question is the exact redox state of Ta in reduced samples. Work with enstatite chrondrite-like melts led to a reduced state of Ta at low oxygen fugacity (Cartier *et al.,* 2014; Cartier *et al.,* 2015), while other studies report a prevalence of Ta^{5+} throughout the experiments but increasing chalcophile behavior at very reducing conditions (Burnham *et al.,* 2012; Fonseca *et al.,* 2014). The disparity is not yet resolved but might depend on the exact compositions of the experimental starting materials. The discussion of reduced or chalcophile behavior of Nb and Ta is of paramount importance for the cause

of the Earth's Nb-Ta paradox, *i.e.*, Earth has a lower Nb/Ta as chondrites (*e.g.*, Münker *et al.*, 2003; Münker, pers. comm.). The exact process for likely sequestering of Nb into Earth's core is not yet unequivocally identified. Tantalum stable isotope data might give further constraints on possible redox transition.

Meteorite components, especially CAIs, are interesting objects for further investigations. So far, our data show that nucleosynthetic anomalies for Ta can be ruled out on the bulk meteorite scale, which is in accord with data for neighboring elements like Hf and W (*e.g.*, Sprung *et al.,* 2010; Schulz *et al.*, 2013; Elfers *et al.*, in review). Calcium-aluminum-rich inclusions, however, give testimony to the earliest solar system evolution and inherit nucleosynthetic variability in heavy mass elements like Hf and W, which might be resolvable within the typical uncertainties achieved (e.g. Burkhardt *et al.,* 2008; Akram *et al.,* 2013; Kruijer *et al.,* 2014; Peters *et al.* 2016). Furthermore, CAIs show mass-dependent isotope fractionation in refractory elements like Ca or Ti, illustrating their complex history, including evaporation and (re-)condensation at high temperatures (*e.g.*, Niederer and Papanastassiou, 1984; Niemeyer and Lugmair, 1984; Niederer *et al.,* 1985). If Tantalum indeed exhibited any nucleosynthetic or irradiation related anomalies in early solar system materials, it would be resolvable in CAIs.

3.5 CONCLUSIONS

We developed a method for high-precision Ta isotope measurements to analyze geological and extraterrestrial samples with a 2σ uncertainty of *ca.* ±4ε. The challenge to identify and overcome potential artefacts is illustrated by our assessment of matrix effects and interference corrections on ^{180}Ta. Especially the destruction of molecular interferences resulting from organics coming off the ion exchange resin or inherited from the sample matrix, and a well-conditioned and cleaned instrument are crucial for accurate measurements.

We are not yet able to resolve possible differences in terrestrial and extraterrestrial bulk rock samples. This is probably due to the generally very low expected magnitude of Ta isotope fractionation and might indicate insignificant nuclear field shift effects for Ta that was never evaluated on a theoretical basis. In context with this work (chapter 2.3.4), we show that commercially available Ta standard materials were not fractionated relative to the terrestrial during the industrial purification process. Because the terrestrial sample set from a large range of geological settings does not show any resolvable differences from the Ta standard solution used, the absolute ^{180}Ta/^{181}Ta ratio of 0.00011705(41) determined from the same standard solutions can be seen

equivalent to the bulk silicate Earth value and even to the bulk solar system reference Ta isotope ratio (chapter 2.3.4).

Even though there is no isotopic variability outside uncertainty, further terrestrial environments like low temperature marine chemical precipitates with Fe-Mn-crusts are interesting objects to be studied to constrain a maximum range of Ta isotope fractionation. Tantalum is fractionated from Niobium during the precipitation of the ferromanganese crusts from seawater (Schmidt *et al.,* 2014). This might hint to kinetically controlled sorption/ desorption reactions onto manganese-oxides, which could also produce sufficiently large isotope fractionation to be analytically resolvable. Furthermore, the tentative co-variation between Ta isotope composition and Ta concentrations in basalts needs to be assessed at higher analytical precision. Better control on possible organic artefacts and measurements in medium resolution mode to reduce tailing effects should improve the analytical requirements to unequivocally identify potential Ta isotope variability within the Earth system

The absence of Ta isotope variability in terrestrial materials makes it plausible that potential Ta anomalies in meteorite components may originate from processes distinct from igneous silicate fractionation. Large scale differences in irradiation environments of the parent body formation regions of our meteorite sample set can be excluded due to indistinguishable Ta isotope compositions from the terrestrial value. The influence of redox states on the redistribution of Nb and Ta between silicates and metal or sulfides at low oxygen fugacity is not yet understood, as are the effects on Ta isotope fractionation. Experiments with combined measurements of trace elements and Ta isotopes in reduced phases might solve the question how redox change affects Ta geochemistry. Such strong Ta isotope effects between silicate material and sulfides or metal should not have been of importance during accretion of reduced bodies to the early Earth, if the accreting bodies equilibrated directly with the Earth's mantle.

In conclusion, there seems to be some tentative isotope variability in our data set that is not yet resolvable at the level of precision achieved. Specific issues like the role of possibly reduced Ta in some solar system objects and the Nb-Ta paradox on Earth are interesting to be complemented by Ta isotope measurements.

Chapter IV

Repeated processing and irradiation of Ca-Al-rich inclusions: evidence from combined high field strength element concentrations and Hf, Ta, and W isotope measurements

4.1 INTRODUCTION

Calcium-Aluminum-rich inclusions (CAIs) are the earliest condensates from the solar nebula and record the building material and processes at the beginning of the solar system (*e.g.*, Grossman, 1972; Ireland and Fegley, 2000). In contrast to bulk meteorites and terrestrial materials, CAIs exhibit anomalies in stable isotopes of heavier elements up to the per mil level, which are only barely resolvable in bulk meteorites and are completely lacking for masses higher than Nd (see Dauphas and Schauble, 2016, and references therein for a recent review). Generally, these mass-independent anomalies are attributed to nucleosynthetic anomalies in the isotope compositions of, e.g., Zr, Mo, Ru, Ba, Nd, Sm, Hf, and W (McCulloch and Wasserburg, 1978a; McCulloch and Wasserburg, 1978b; Schönbächler *et al.,* 2003; Burkhardt *et al.,* 2008; Chen *et al.,* 2010; Sprung *et al.,* 2010; Burkhardt *et al.,* 2011; Akram *et al.,* 2013; Kruijer *et al.,* 2014; Peters *et al.*, 2016). These isotope anomalies are a direct vestige of elemental production in different stellar sites and preservation of distinct carrier phases in the solar system (e.g., McCulloch and Wasserburg, 1978a; Rotaru *et al.,* 1992). As such, all elements so far analyzed in CAIs show contrasting excesses and depletions in nucleosynthetic components, in case of Zr and Hf even for the same element in different CAIs (Akram *et al.,* 2013; Peters *et al.*, 2016). Thus, a simple model with admixing of material with a distinct isotope pattern during earliest stages of solar system formation does not explain the overall complexity observed (*e.g.*, Cameron and Truran, 1977; Brennecka *et al.,* 2013).

In addition to nucleosynthetic anomalies, irradiation from the proto-Sun has been inferred to alter the isotope compositions of refractory elements in a mass-independent way at the inner edge of the protosolar envelope (Shu, 1997; Gounelle *et al.,* 2001). The discovery of extinct ^{10}Be in CAIs was interpreted as evidence for nuclide production in the solar nebula (McKeegan, 2000). This

finding was further supported by excess in rare ^{50}V correlated with ^{10}Be in refractory inclusions (Sossi et al., 2016). However, the excess of isotope produced possibly by irradiation could also be explained by a nucleosynthetic origin (in case for ^{50}V), and as inherited radioactivity from galactic cosmic ray production in the interstellar medium with regard to ^{10}Be (Desch *et al.,* 2010).

Trace element concentrations, particularly those of the rare Earth elements (REE), allow constraining the condensation conditions of individual CAIs (Martin and Mason, 1974; Davis and Grossman, 1979). We acquired high-precision trace element data on high field strength element concentrations (HFSE) to compare their patterns with the REE data and to constrain possible secondary processes after initial condensation. The condensation model is generally accepted and tested against refractory element concentration data (Kornacki and Fegley, 1986). However, old data sets lack sufficient precision, with errors of more than ten percent on old measurements, especially of low concentrated high-mass elements like Ta, Th, and U. Isotope dilution enables characterization of trace element concentrations of better than 1% for all elements of the periodic table with more than one isotopes (Münker *et al.,* 2003; Stracke *et al.*, 2014). This improved precision allows a detailed inspection of the presently accepted models of condensation of elements from a hot solar nebula. Particularly, the combination of isotope and concentration data gives information on processes controlling isotope heterogeneities like dilution, mixing and elemental redistribution.

Tantalum-180 is one of the most peculiar isotopes in the chart of nuclides and displays properties that are interesting for astrophysical and cosmochemical questions. The relative abundance of ^{180}Ta yields only 0.0117% with the remaining Ta being present as the large isotope ^{181}Ta (chapter 2.3.4). Interestingly, ^{180}Ta is the only known isotope in an excited nuclear state without observed de-excitation, whereas in its ground state it undergoes decay to ^{180}Hf and ^{180}W with a half-life of 8.1h (Hult *et al.,* 2006). The large difference in isotope abundances and the low concentrations of Ta compared to the neighboring element Hf is ideal to investigate potential ingrowth on ^{180}Ta by nuclear reactions on surrounding nuclides. Until now, the large difference in isotope abundances and the fact of Ta being the rarest element in the solar system hindered high-precision isotope ratio measurements of Ta in meteorites and their components.

The low abundance of ^{180}Ta and its presence in an isomeric state was a long-standing puzzle to account for its production under stellar conditions. Two nucleosynthetic pathways in different stellar environments have been discussed for production of ^{180}Ta. The neutrino-process (ν-process) is one of the production pathways included in the term p-process (summarizing the p-rich nuclides away from the main s-process path) and takes place in core-collapse supernovae type II (cc SNe II), where the large neutrino flux induces the necessary particle reactions (*e.g.*, Woosley *et al.,* 1990; Travaglio *et al.,* 2011; Rauscher *et al.,* 2013). The second process is a diversion from the well

understood main s-process path typical for medium-sized stars during their asymptotic giant branch (AGB) stage (*e.g.*, Beer and Ward, 1981; Yokoi and Takahashi, 1983; Käppeler *et al.,* 2004). Recent astrophysics literature converges towards a predominant production of ^{180}Ta by the s-process, leaving only minor amounts of ^{180}Ta necessary to be produced by the ν-process (Bisterzo *et al.,* 2014). Solar ^{181}Ta abundances are easily reconciled by comparable amounts of s- and r-process derived nuclides (Bisterzo *et al.,* 2014). In case of identification of nucleosynthetic anomalies, Ta isotopes in meteorites could give independent constraints on the validity of astrophysical models for ^{180}Ta. In this regard, isotope anomalies of Ta need to be compared to p-process anomalies in other heavy elements to constrain their origin, making Ta a potential sensitive tracer of uncommon nucleosynthetic components.

The source of different nucleosynthetic components and the extent of irradiation-induced reactions on heavier isotopes in the beginning of the solar system are only poorly constrained. Together with Ta isotope data, we present for the first time high-precision isotope dilution data for the extended HFSE (Zr, Nb, Hf, Ta, W) and Th-U that overcome limitations in uncertainties of earlier studies. High-precision Ta isotope measurements were performed using multicollector-inductively coupled plasma-mass spectrometry (MC-ICP-MS) in leachates of carbonaceous chondrites and CAIs to search for possible isotope heterogeneities. The exceptional physical properties of ^{180}Ta might provide additional constraints to decipher the earliest history of our solar system by analyzing CAIs for evaluating the role of nucleosynthetic components or early irradiation.

4.2 METHODS

4.2.1 Sample description and preparation

A total of ten samples were investigated for HFSE concentrations and Hf-Ta-W isotope compositions, comprising seven CAI separates from Allende and NWA 3095, a CAI-enriched Allende powder (Stracke *et al.*, 2012) as well as three meteorite pieces (CM2 Murchison, CV3.6 Allende, and CV3 NWA 3118).

Five CAIs were separated from CV3 carbonaceous chondrites Allende and NWA 3095 (CAI_C-BN_1,2,3 from Allende; CAI_C-BN_4,5 from NWA 3095). The large Allende sample (~200g) comprised a fusion crust and was not exposed to terrestrial alteration, while NWA 3095 (cut as a ~5g plate) is classified as weathered (W2). The weathering grade is of subordinate importance for this study as most HFSEs except W are considered immobile in aqueous solutions (König *et al.*, 2008, and references therein). Hence, any potential nucleosynthetic anomaly is only diluted by a terrestrial component (by definition isotopically “normal”). To avoid direct contamination from the steel tool,

the fine drill tool was only used to excavate the inclusions. Subsequently, the CAI pieces were carefully broken out with a spatula. The samples were then rinsed with ethanol in an ultrasonic bath to remove drill powder, matrix material, and fine grained weathered material in the case of NWA3095. Subsequently, the cleaned CAI pieces were handpicked to remove larger pieces of leftover matrix. Smaller grains of each CAI (~200µm) were collected for preparation of thin section mounts for electron microprobe (EMP) analyses. The picked CAI material was crushed in an agate mortar. Note that remaining matrix particles are left in the cuts for the sake of full CAI material recovery required for high precision isotope measurements. Notably, even 10wt.% of matrix material would not influence the HFSE and REE content in the measured cuts, as CAIs are commonly enriched by more than an order of magnitude in these elements. All CAIs belong to the coarse grained CAI group. This means they were affected by igneous processing, likely including evaporation, as they are not direct products of condensation (*e.g.*, Grossman *et al.,* 2002). A disadvantage of this sampling approach is that we might miss the largest isotope variability being present in common fine-grained CAIs (e.g., Kruijer *et al.,* 2014).

Sample CAI_C-BN_6 is an Allende powder enriched in CAI material, previously analyzed as Allende C4 in Stracke et al. (2012) and re-measured for its HFSE in this study. For the benefit of readability, the samples names (CAI_C-BN_#) were shortened in the text to CAI-#. Calcium-Aluminum-rich inclusions A33 and A44 were large samples originally separated by Herbert Palme and are described elsewhere (Floss *et al.*, 1992; Jacobsen *et al.,* 2008).

For leaching experiments, meteorite pieces of CM2 Murchison, CV3.6 Allende, and CV3 NWA 3118 were obtained. Murchison and Allende have been investigated extensively for nucleosynthetic anomalies in the past and are primitive enough with low petrologic types to inherit presolar carriers (Huss *et al.,* 2003). The meteorites were ground to bulk meteorite powders in an agate mill from ethanol-rinsed, gram-sized pieces.

4.2.2 Digestion and chemical separation

The chemical treatment was performed in the joint Cologne-Bonn clean lab facilities with ultrapure acids produced in sub-boiling distillation. De-ionized water conductivity was always at 18.2 MΩ and perchloric acid has been certified as Suprapur grade. Weights of the samples are reported in Table 4.1. The digestion was carried out in a 1:1 mixture of concentrated HF and HNO_3 for two days at 120°C. After a dry-down step, fluoride precipitates and organics from remaining matrix material were attacked with perchloric acid and repeatedly drying in concentrated HNO_3. All dissolution steps were repeated once to reach full digestion. Calcium-Aluminum-rich inclusions are not known to contain presolar grains and were not digested in high-pressure vessels. The samples were dissolved

in 6M HCl/ 0.06M HF from which two aliquots were taken. A 10% aliquot for high-precision trace elements measurements was spiked with a set of in-house solutions enriched in single isotopes of the elements to be analyzed, while the second 5% cut was used to obtain general trace element concentration data.

The isotope dilution method for Zr, Nb, Lu, Hf, Ta, and W is based on the chemical separation and measurement protocols developed by Münker *et al.* (2001), Weyer *et al.* (2002), and Kleine *et al.* (2004). The mixed spike solutions with enriched ^{236}U, ^{229}Th, ^{183}W, ^{180}Ta, ^{180}Hf, ^{176}Lu, and ^{94}Zr tracers were calibrated against >99.9% AMES pure metal standards. After spike-sample equilibration overnight in 6M HCl/ 0.06M HF at 120°C, the HFSE were separated in a three-step ion exchange protocol involving Eichrom™ LnSpec resin and Biorad® AG-1 X8 anion resin (Münker *et al.,* 2001). The first step allowed collection of the HREE cut (including Lu) and separation of the HFSE from the matrix. Tungsten and Ta were then isolated on anion resin from the remaining HFSE-cut, whose left-over Ti, Zr, and Hf could then individually be separated in a third step on the column filled with LnSpec. An additional step with Eichrom™ TRUSpec resin allowed the separation of Th and U from the remaining matrix cut (Luo *et al.,* 1997).

Leaching experiments were conducted with *ca.* 1.5g of meteorite powder after the protocol by Elfers *et al.* (in review). The first step was carried out with hydrochloric acid and 0.06M HF (to keep dissolved HFSE in solution) and to attack metals and sulfides. The next step containing 24M HF attacked main silicates including serpentine, pyroxene, and olivine. The residue was subsequently digested for three days in high-pressure Parr™ bombs at 180°C to bring refractory grains into solution. The leaching was limited to two steps to obtain sufficient material for measurements of low abundance isotopes of Hf, Ta, and W.

Tantalum was purified after the one stage protocol described in chapter 3.2.3 (modified after Münker *et al.,* 2001) and employing an additional clean-up using Biorad® AG-1 X8 anion resin. The rock matrix is first eluted with a low molarity HCl/ HF mixture, while the HFSE stick as negative fluoride complexes on the resin. A clean cut containing all HFSE except Ta can then be collected in 6M HNO_3/ 0.2M HF, while Ta is eluted with additional 6M HNO_3/ 0.2M HF-1% H_2O_2. The Ta clean-up contains reduced acid strengths of 3M HNO_3/ 0.2M HF and smaller resin amounts of 1ml to reduce blanks of isobarically interfering Hf in measurements. The HFSE were further processed with TEVA resin to obtain a clean W cut (Peters *et al.,* 2015). Remaining Ti and Zr, and Hf were loaded on Eichrom™ LnSpec resin to collect Hf after the protocol from Bast *et al.* (2015). All spiked and unspiked element cuts were dried down, treated with hydrogen peroxide, and dissolved in 0.56 M HNO_3/ 0.24M HF prior to mass-spectrometric measurements.

4.2.3 Data acquisition

4.2.3.1 Electron microprobe analysis

Compositional data of the CAI phases were acquired using a JEOL 8900RL electron microprobe, equipped with 5 wavelength dispersive spectrometers (WDS). The accelerating voltage was set to 15 kV and the beam current to 20 nA. Element data wer gained for typical major elements in meteorites and CAIs (Na, Mg, Al, Si, Ca, Ti, Cr, Mn, Fe, Ni) with WDS and was corrected with the built-in ZAF-algorithm. Iron was only present in silicates/oxides and calculated as FeO. Titanium, however, is also present as Ti^{3+} in CAIs that are highly reduced. The amount of Ti^{3+} in Ti-bearing pyroxenes was calculated from the oxygen excess (or cation deficit) of the pyroxene compositions calculated with assumed TiO_2 after the method from Simon *et al.* (2005). The recalculated pyroxene compositions are considered as stoichiometric with exactly two cations in the tetrahedral site and one octahedral *Ca.* The lack of a well calibrated secondary standard and low Ti contents in some samples prevented the calculation of oxygen fugacity, however, the Ti^{3+}/Ti^{total} is considered as an appropriate proxy for the prevalent oxygen fugacity during pyroxene crystallization. The petrography and mineral relations of the analyzed CAI pieces are attained from combination of BSE pictures and single mineral analyses.

4.2.3.2 Trace element and HFSE concentration data of the CAIs

Trace element concentrations of CAIs 1 to 6 were obtained by solution ICP-MS using a 5% aliquot of the fully digested samples. Additionally, Nb-Ta-Zr-Hf-Lu-W-U-Th concentrations were determined by isotope dilution and MC-ICP-MS measurements. The trace element aliquots were dissolved in 2ml of 2% nitric acid and measured using an Agilent 7500cs quadrupole ICP-MS at the Christian-Albrechts-University Kiel, Germany. Internal normalization was applied by addition of In and Re in the sample solutions. Accuracy is derived from comparison with suggested values from international reference materials BIR-1 and BCR-2 and is constrained to be better than ±5% for most lithophile elements and better than ±3% for the REE. Details of the applied method are given in Garbe-Schönberg (1993).

Concentrations for Nb, Zr, Lu, Hf, Ta, W, Th, and U were determined by isotope-dilution using the Thermo Scientific Neptune™ MC-ICP-MS in the Cologne-Bonn facilities, including the $^{176}Hf/^{177}Hf$ isotope composition in the Hf cut. The analytical protocol for the HFSE is described in Weyer *et al.* (2002), Münker *et al.* (2001), and Kleine *et al.* (2004). The protocol for Lu measurements follows Lagos *et al.* (2007). Uranium isotope dilution measurements were performed by normalizing to $^{233}U/^{236}U$ of 1.01906 (Richter *et al.*, 2010) and measured $^{229}Th/^{232}Th$ were normalized to $^{235}U/^{238}U$ of

doped CRM 112A. Measured $^{176}Hf/^{177}Hf$ isotope compositions were normalized to $^{179}Hf/^{177}Hf$ of 0.7325 using the exponential mass fractionation law. Hafnium isotope compositions were corrected from the spiked data and are given relative to 0.282160 of JMC-475. The HFSE were corrected for mass discrimination using doped Sr (for Zr and Nb measurements), Yb (Lu), Re (Ta, W) or doped U (see above). Niobium, as a mono-isotopic element, was measured relative to Zr/Nb standard solutions. External reproducibility is typically better than ±1% for all analyzed elements except Nb (*ca.* ±4%). Procedural blanks for all elements analyzed are typically below 50pg except for Zr, which yielded blanks of *ca.* 1ng.

4.2.3.3 Hafnium, Ta, and W isotope measurements

Hafnium-Ta-W isotope composition measurements were performed using the Neptune™ MC-ICP-MS at the joint Cologne-Bonn facilities, whereas parts of the Ta isotope measurements were also carried out at the Neptune Plus™ at Thermo Scientific in Bremen, Germany. All elements were measured with a high-transmission interface using X-skimmer cones in combination with a Cetac Aridus™ desolvation system. Tantalum isotope measurements further required a Jet sampler cone for high sensitivity of small sample sizes (*ca.* 1600-1900 V per µg/g of solution). Solutions were introduced with a MicroFlow PFA nebulizer at uptake rates of 100µl/min. Correction of the instrumental mass bias is always performed with the exponential law. All isotope data are reported as ε- or µ-values that is $\varepsilon^{y}X = (R_{sample}/R_{Earth}) - 1) \times 10^{4}$ and $\mu^{y}X = (R_{sample}/R_{Earth}) - 1) \times 10^{6}$, with ^{y}X indicating the isotope y of element X and R_{sample} the isotope ratio of the samples relative to the respective isotope composition of Earth R_{Earth}, with all standard solutions having been prepared from pure metal standards from AMES laboratories (Weyer *et al.,* 2002). The Hf and W isotope compositions for the CAI data were previously published in Peters *et al.* (2016).

For $^{180}Ta/^{181}Ta$ analyses, instrumental mass discrimination was corrected by doping of the Ta solutions with Yb and normalization of the measured Ta isotope data to $^{173}Yb/^{171}Yb = 1.12489$. Isobaric interferences on minor ^{180}Ta were monitored on ^{178}Hf, ^{179}Hf and ^{183}W. Low abundance ^{180}Ta and the interference correction from large ^{180}Hf necessitated the use of $10^{12}\Omega$ feedback resistors for Faraday cup amplifiers at Cologne-Bonn and $10^{13}\Omega$ resistors at Bremen for sufficiently precise isotope ratio measurements. Isotope ratios of $^{180}Hf/^{178}Hf = 1.2863$, $^{180}Hf/^{179}Hf = 2.5753$, and $^{180}W/^{183}W = 0.008304$ used for interference correction were artificially biased with the fractionation factor derived from Yb ratio measurements. Due to the large interference correction, some samples failed the threshold for accurate interference correction of $8 \cdot 10^{-6}$ $^{178}Hf/^{181}Ta$. Hafnium-doped Ta standard solutions were measured in each session and followed a linear trend away from $\varepsilon^{180}Ta$ with increasing $^{178}Hf/^{181}Ta$, which was used as a mean to correct for impure samples within the bounds of

the doped standards. Uncertainties of this trend were propagated into the final uncertainty of the measurement. The CAI data were obtained in Bremen, where newly developed $10^{13}\Omega$ resistors were available. In some cases, ^{178}Hf corrected data were erroneous due to an unidentified molecular species on mass 178, which required use of ^{179}Hf as an interference monitor. Full details on the mass spectrometric protocol and sample measurements were presented in chapters 2.2.1 and 3.2.4.

For Hf isotope measurements, all isotopes (^{174}Hf, ^{176}Hf, ^{177}Hf, ^{178}Hf, ^{179}Hf, ^{180}Hf) were collected together with interference monitors on ^{172}Yb, ^{175}Lu, and ^{182}W. Two $10^{12}\Omega$ resistor amplifiers were attached to the cups for ^{172}Yb and ^{174}Hf. The Hf data have been calculated as ^{17x}Hf/^{177}Hf and the instrumental mass bias was corrected by normalizing to ^{177}Hf/^{179}Hf = 0.7325. Tantalum concentrations were tested to be sufficiently low in sample solutions and Yb/Hf (element ratio) were typically < 10^{-5}, such that isobaric ^{174}Yb can be accurately corrected for (Peters *et al.,* 2015). External precision for ^{174}Hf/^{177}Hf ratios were typically <±70 ppm.

Measurement uncertainties for Hf are given either as 2 S.D. of the mean composition of the standard throughout an analytical session (n >10 standards per analytical session), or as the within-run variation of the sample (2 S.E.), whichever is larger. Tantalum isotope data are presented in Table 4.3 as the in-run variation of the sample (2 S.E.) and are presented in the Fig. 4.3 together with the external reproducibility of the respective sample size, derived from standards of same concentration. External Ta isotope reproducibility at Bremen and Cologne-Bonn (at ion currents of $4.5\cdot10^{-10}$ A and $2\cdot10^{-9}$ A, respectively) was typically around ±4ε ^{178}Hf and ±8ε for ^{179}Hf corrected data, respectively.

4.3 RESULTS

4.3.1 Mineralogy and classification of CAIs

The CAIs investigated in this study contain the typical mineralogy of melilite (a solid solution of $Ca_2Al_2SiO_7$ and $Ca_2MgSi_2O_7$), spinel, and fassaite (Ti-Al-diopside). Anorthite ($CaAl_2Si_2O_8$) and perovskite ($CaTiO_3$) were present as minor phases. These phases can be considered as primary, i.e., having been condensed and re-melted in the H_2-rich stages of the early solar nebula (Grossman *et al.,* 2002). Earliest condensates like hibonite or grossite were not identified. In addition, secondary phases like grossular ($Ca_3Al_2Si_3O_{12}$), Al-diopside, and anorthite were present, which can be related to processes on the parent body (Brearley and Krot, 2013). Although our set of samples is limited, we sampled both Type A and Type B CAIs, as inferred from their melilite compositions, while forsterite-bearing inclusions were not present. Table 4.1 gives an overview of the weight, classification, and mineralogy of all analyzed CAIs. Data on A33 and A44 are reproduced from Jacobsen et al. 2008. The CAIs classified as type A have a maximum of 36 mol.% of Åkermanite (Mg-rich endmember) in their

melilite solid solutions and, if present, up to 16 wt.% TiO_2 in the fassaite. The high Ti concentration in fassaite did allow estimates on the possible fraction of reduced Ti. Our data set seems to contain minerals from 0.00 to 0.76 in Ti^{3+}/Ti^{total}, broadly consistent with the most reduced CAI interior (Simon *et al.,* 2005). The low Ti^{3+} contents might hint to later oxidation of parts of the CAIs, consistent with widespread secondary minerals in Allende and CV chondrites (Krot *et al.,* 1995). Notably, we only sampled small pieces for EMP analyses, often from the rim with meteorite matrix attached, where parent body processes might have been more pronounced. However, we note that our EMP measurement protocol might not have been accurate enough without the use of secondary standards. More details including BSE pictures and mineral analyses can be found in Appendices A and B.

CAI_C-BN_1 exhibits an unusual mineralogy. In contrast to the typical minerals observed in CAIs, it consists of clinopyroxene (close to Hedenbergite endmember, $CaFeSi_2O_6$), Fe-rich spinel [$(Fe,Mg)Al_2O_4$], grossular, and nepheline ($NaAlSiO_4$). These minerals are described as typical alteration products in oxidized CV3 chondrites (Krot *et al.,* 1995). However, this assemblage with exactly these constituents has not yet been described elsewhere. Ca-Fe-rich inclusions exhibit assemblages of hedenbergite pyroxenes, andradite ($Ca_3Fe_2Si_3O_{12}$), kirschsteinite ($CaFeSiO_4$), and wollastonite ($Ca_3Si_3O_9$) and are normally related to dark inclusions (Krot *et al.,* 1998). The spinels in CAI-1 are rounded and show an onion-shell pattern, unusual for the usually euhedral, early formed crystals observed inside refractory inclusions (see Appendix A). Either they are crystallized secondary or, more likely, this texture is the result of an aqueous exchange and erosion of the primary crystals (Krot *et al.,* 1995). Together with the mineralogy, we interpret this pattern as a secondary alteration feature of a CAI with delivery of Na and Fe during leaching of Mg and subsequent metamorphic dehydration. Notably, CAI-1 was macroscopically zoned but just one small grain was randomly collected for EMP analysis, which most likely originates from the outer and altered rim. All grains collected from the CAIs in this study were collected from the crushed sample material before digestion, so that they do not necessarily provide a representative view on the overall mineralogy of the inclusions.

Table 4.1 Weights, classification and mineralogy of analyzed CAIs. Information of A33 and A44 are taken from Jacobsen et al. (2008). Note that CAI-1 is an altered CAI with secondary mineralogy (denoted as "alt.") and CAI-6 is the CAI-rich powder C4 from Stracke et al. (2012). Abbreviations are as follows: me = melilite; px = pyroxene (usually fassaite, Ti-Al-diopside); sp = Mg-spinel; pv = perovskite; an = anorthite; grs = grossular; di = diopside; mcl = monticellite [$Ca(Mg,Fe)SiO_4$]; ne = nepheline. Fields in the table lacking the respective mineral phase are marked with n.d. (not determined) and "-" denotes the inability to constrain the information due to lacking sample material or information.

CAI	**Meteorite**	**Weight**	**Grain size**	**REE pattern**	**Type**	**Mineralogy**		**Composition**			
						Major	minor/ secondary	melilite	fassaite		
		mg						mol.%	TiO_2 (wt.%)	Al_2O_3 (wt.%)	Ti^{3+}/Ti^{total}
A33	Allende	-	coarse	Group I	A	me, Ca-px, sp	pv, an, Al-di	Åk9–21	up to 16	20	-
A44	Allende	-	coarse	Group III	B	me, Ca-px, sp, an	pv, an, grs, mcl, metal-sulfides	Åk21–55	2–8	18–20	-
CAI_C-BN_1	Allende	29.94	fine	Group II	alt.	Fe-rich sp, Fe-rich di, ne, (hydro-)grs	-	n.d.	n.d.	up to 2	n.d.
CAI_C-BN_2	Allende	89.66	coarse	Group II	A	me, sp, Ca-px	pv, Fe-rich sp, an, Al-di	Åk5–36	5-7.8	20-22	0-0.76
CAI_C-BN_3	Allende	181.26	coarse	Group II	B	me, Ca-px, sp	grs	Åk51–75	1.4-6.0	12.7-20.8	0.52
CAI_C-BN_4	NWA3095	288.89	coarse	Group V	B	me, Ca-px, sp, an	grs, Al-di	Åk26–54	4.8–9.6	14.2–21.8	0.26-0.76
CAI_C-BN_5	NWA3095	201.22	coarse	Group II + V	A	me, sp	pv, an, albite	Åk11-23	n.d.	n.d.	n.d.
CAI_C-BN_6	Allende	181.85	-	Group III	-	-	-	-	-	-	-

4.3.2 Rare earth and high-field strength element isotope dilution concentration determinations of CAIs

The concentration data for the HFSE achieved with two methods is different for several elements. Particularly the HFSE concentrations in CAI-1 obtained at Kiel are elevated by up to 200% in W, which might be a result of the small sample size and additional blank contributions. In contrast, most of the elements in CAI-5 are depleted in the Kiel data by *ca.* 10%. Niobium and Ta seem to have selectively been lost in CAI-3, which is lacking 80-90% of the elements compared to isotope dilution data.

On the basis of their REE patterns, CAIs can be classified into six groups (after Martin and Mason, 1974; Mason and Taylor, 1982). For interpretation, concentration data are normalized to REE concentrations that were recently determined for CI chondrites at higher accuracy (Dauphas and Pourmand, 2015). Allende CAIs 1 to 3 exhibit typical group II patterns, associated with the previous fractionation of an ultra-refractory phase, whereas the other patterns are relatively flat (CAI-4: group V; CAI-5: group II + V; CAI-6 group III). All REE patterns of investigated CAIs are shown in Fig. 4.1, and the resulting classification is listed in Table 4.1. Concentration data for A33 and A44 were provided by Palme and Spettel (pers. comm.). The REE pattern of CAI-6 (C4) is in accord with the published compositions of type III CAIs, with only a minor negative Eu anomaly (Stracke *et al.,* 2012). In general, the lack of negative Eu anomalies is a striking feature in all our analyses, which is usually one of the benchmarks in CAI classification.

In detail, further features are distinct from the patterns originally published by Martin and Mason (1974). Calcium-Aluminum-rich inclusion 2 is depleted in LREE elements relative to MREE, while the HREE still show the type II pattern. Reincorporation of ultra-refractory material into the depleted CAI with type II pattern might result in the observed enrichment of Eu to Ho. A negative Ce-anomaly is present in CAI-3, indicating more oxidizing conditions at some stage of its history (Davis *et al.,* 1982). CAI- 5 seems to exhibit a transitional pattern with unfractionated type V and only a slight depletion in elements (Gd - Er, Lu) typical for CAI-type II. Those deviations in REE patterns from thermodynamically controlled condensation might be imprints of a multi-stage history experienced by the individual CAIs, *i.e.*, changes in oxygen fugacity during later (partial) melting and mixture of material (e.g., Ireland and Fegley, 2000).

Notably, the severe alteration did not erase of the typical group II pattern in CAI-1. Thus, we infer that isotope anomalies in fluid-immobile HFSE are still inherited from the original inclusion. In contrast, fluid-mobile elements like Rb and Cs are present in all CAIs in comparable abundances as on the bulk rock scale, although they are moderately volatile and should not be as abundant in high-temperature condensates like CAIs. Thus, aqueous alteration must have been pervasive all over the

parent body, affecting all components in CV chondrites (Brearley and Krot, 2013). In case of CAI-1, Zn, Rb, Sn and Cs are even enriched to abundances higher than those of bulk CV chondrites. The full trace element data set for all CAIs is given in Appendix C.

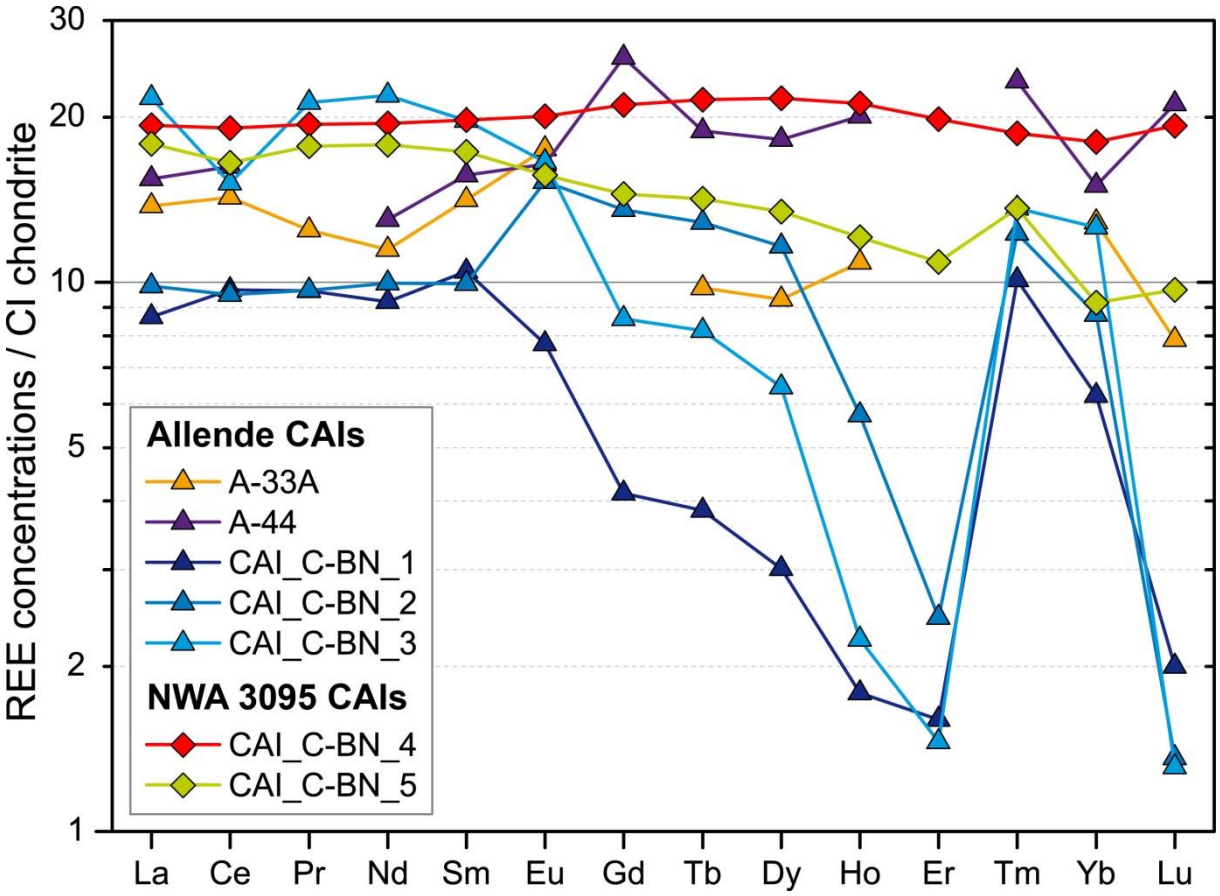

Fig. 4.1 Rare Earth element patterns of investigated CAIs. The data are normalized to the average CI data from Dauphas and Pourmand (2015). Data for A33 and A44 were provided by Palme and Spettel (pers. comm.).

The extended isotope dilution HFSE+ U and Th data set is presented in Table 4.2 and plotted relative to CI chondrite abundances in Figure 4.2. The repeated HFSE and Lu measurement of Allende C4 powder (here: CAI-6) are indistinguishable within 1% from earlier data (Stracke *et al.,* 2012), except for Nb and Ta that are lower by 10 and 3%, respectively. Minor sample heterogeneity with regard to Nb and Ta might explain the differences and these were also inferred to account for variations between complementary methods in the previous study (Stracke *et al.,* 2012). Historical inclusions A-33 and A-44 were constrained to contain 0.24 and 0.25 µg/g Ta, respectively. The inclusions with type II REE pattern are depleted in Zr and Hf, which behaved similar to the ultra-refractory REE. Calcium-aluminum-rich inclusions 4 and 6 have unfractionated HFSE pattern, enriched by a constant factor relative to CI chondrite. Tungsten and Mo are depleted in CAIs with type II patterns, where the more refractory W shows less depletion. The depletion of Mo cannot

directly be reconciled with other REE in terms of the condensation temperature as Mo has a comparable condensation temperature as La or Pm (1590K vs. 1578 and 1582, respectively; Lodders, 2003) that are not depleted. Uranium shows the most variability, which is not related to any condensation pattern. This may reflect aqueous alteration as for Rb or Cs. Thorium and Ta are only depleted to a minor degree in CAIs with group II pattern. Interestingly, Nb is always more depleted relative to Ta.

Lutetium concentration data together with Lu-Hf systematics and radiogenic ^{176}Hf isotope data are additionally reported in Table 4.2. The ^{176}Lu/^{177}Hf ratio of 0.032 – 0.043 is rather uniform over different REE groups of investigated CAIs. This was in the first place unexpected but is an expression of the similar high condensation temperatures, where both elements are effectively depleted in CAIs with type II patterns. The large variability in ε^{176}Hf is a consequence of the error on the small amounts of Hf measured and possible nucleosynthetic anomalies that are not yet corrected (Sprung *et al.,* 2010; Akram *et al.,* 2013).

Table 4.2 Extended HFSE concentrations and ^{176}Hf isotope systematics determined by MC-ICP-MS. Error on Hf data are given on the last digits. Concentrations are given as µg/g. Allende C4 powder data from Stracke *et al.* (2012) are shown for comparison. Note that the Hf isotope data are not yet corrected for nucleosynthetic anomalies.

	CAI-1	**CAI-2**	**CAI-3**	**CAI-4**	**CAI-5**	**CAI-6**	**All C4**
Zr	4.807	4.364	4.119	68.28	29.86	26.29	26.47
Nb	1.24	1.78	1.69	4.56	1.46	1.67	1.86
Lu	0.0341	0.0295	0.0294	0.4898	0.2774	0.1962	0.1969
Hf	0.1516	0.1117	0.1151	2.009	0.9120	0.7629	0.7690
Ta	0.1193	0.1767	0.0991	0.2998	0.1883	0.0991	0.1020
W	0.242	0.529	0.207	1.56	1.05	0.590	0.595
Th	0.139	0.199	0.339	0.529	0.421	0.206	
U	0.111	0.033	0.051	0.058	0.136	0.046	
^{180}Hf/^{184}W	0.717	0.242	0.637	1.472	0.998	1.480	1.480
^{176}Lu/^{177}Hf	0.03194	0.03753	0.03625	0.03461	0.04318	0.03652	0.03635
^{176}Hf/^{177}Hf	0.286479	0.284216	0.283881	0.282901	0.283778	0.283151	0.283041
±2 S.E.	261	78	55	7	12	18	8
ε^{176}Hf(4567)	136.5	37.8	29.9	0.1	4.2	3.0	-0.4
Zr/Nb	3.89	2.45	2.43	15.0	20.5	15.7	14.2
Zr/Hf	31.72	39.06	35.79	34.00	32.74	34.46	34.42
Nb/Ta	10.4	10.1	17.1	15.2	7.75	16.9	18.3

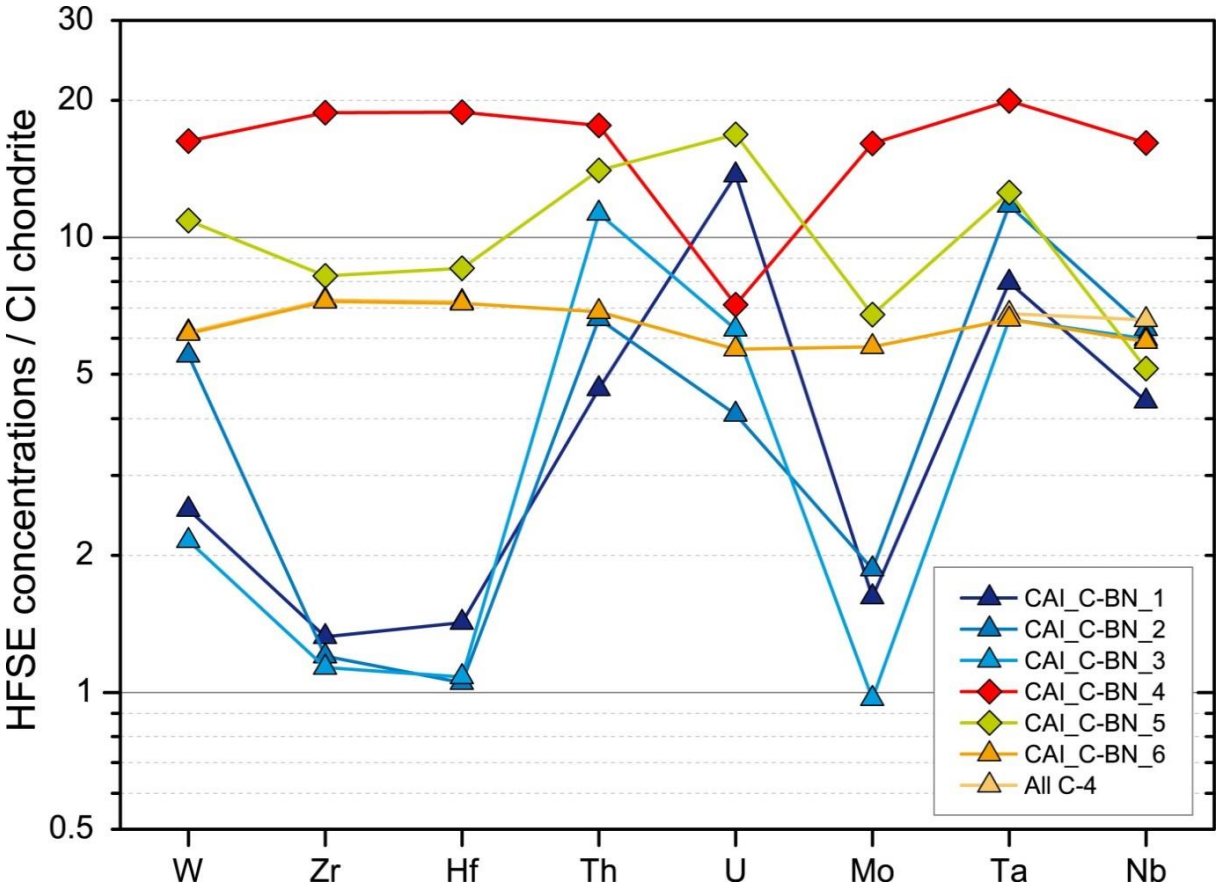

Fig. 4.2 Extended HFSE high precision isotope-dilution concentration data normalized to CI after Palme et al. (2014). The elements are arranged according to their 50% condensation temperature from highest on the left to lowest on the right (Lodders, 2003).Allende C4 powder is shown for comparison (Stracke *et al.,* 2012). The molybdenum concentrations were obtained without isotope dilution. The general HFSE patterns exhibit typical features which can be related to the same processes controlling the REE patterns, namely variable depletion of ultra-refractory elements.

4.3.3 Ta and Hf isotope ratio data

In contrast to terrestrial samples and bulk meteorites (chapter 3.3), leachates of meteorites and refractory inclusions exhibit Ta isotope anomalies (Fig. 4.3). Two leachates 2 are slightly resolvable outside the external reproducibility (Table 4.3). The Allende leachate 2 shows positive ^{180}Ta anomalies with ε^{180}Ta = +8.9 whereas the Murchison leachate 2 is negative with ε^{180}Ta = -10.0. NWA 3118 has no resolvable anomalies and the residues have Ta concentrations that are too low for precise measurements. A terrestrial basalt was leached with the same procedure to test the accuracy and did not exhibit any anomalies. Hafnium isotopes show deviations in ^{174}Hf, ^{178}Hf and ^{180}Hf in the ^{179}Hf/^{177}Hf normalization scheme. The Hf isotope anomalies are correlated and can unequivocally be explained by deficits and enrichments of an s-process component (Elfers *et al.*, in review). The initial

leaching protocol applied did not dissolve enough Ta and Hf, which prevented measurements of the leachates 1.

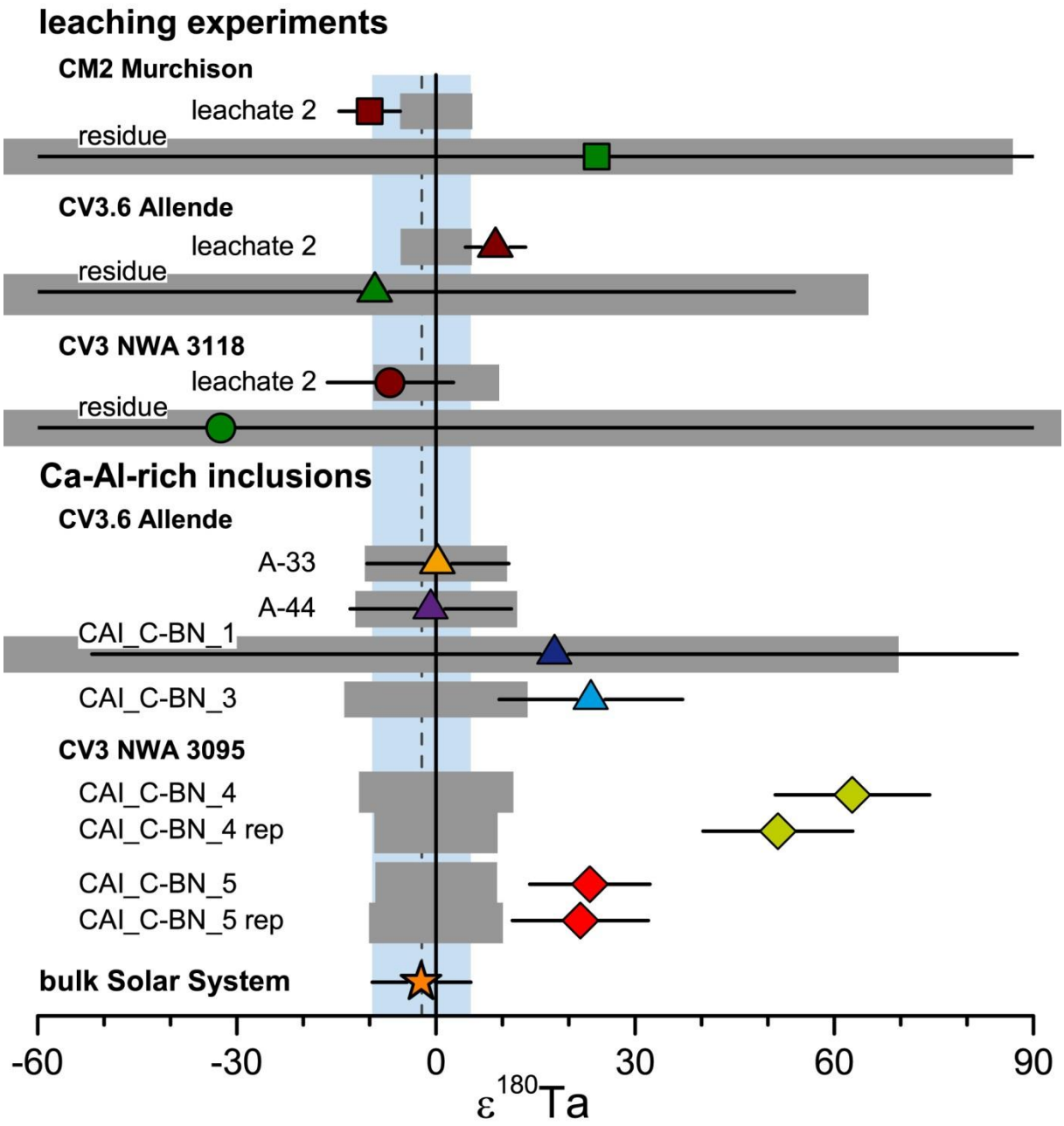

Fig. 4.3 Tantalum isotope composition of leaching experiments and CAIs. The bulk solar system value is given for comparison and indicated by the blue field (see chapter 3.3). The grey bars give the external reproducibility of individual measurements associated with the respective quantity of measured Ta. Note that error bars of the residues are larger than the scale.

Table 4.3 Tantalum and Hf isotope compositions of leachates and residues. The uncertainties are given as the 2 S.E. of the individual measurements and the terrestrial data are given as presented with the 2S.E. of repeated measurements.

	Tantalum isotope data (rel. $^{171}Yb/^{173}Yb$)				**Hafnium isotope data (rel. $^{179}Hf/^{177}Hf$)**						
	$\varepsilon^{180}Ta$	±	ext. rep. (ε)	Cut (%)	$\varepsilon^{174}Hf$	±	$\varepsilon^{178}Hf$	±	$\varepsilon^{180}Hf$	±	cut (%)
LP2 (ocean island basalt, La Palma)											
leachate 1	2.7	1.3	4.0	-	-	-	-	-	-	-	-
leachate 2	1.8	1.1	4.0	-	-	-	-	-	-	-	-
Residue	2.0	1.4	4.0	-	-	-	-	-	-	-	-
Murchison (CM2 chondrite)											
leachate 2	-10.0	4.6	5.4	94	-0.07	0.36	0.04	0.03	0.13	0.06	67
Residue	24.2	85.2	86.9	6	1.11	0.41	1.92	0.03	2.39	0.08	33
Allende (CV3.6 chondrite)											
leachate 2	8.9	4.5	5.4	93	1.09	0.48	2.52	0.03	3.15	0.05	51
Residue	-9.2	63.2	65.1	7	-0.55	0.47	0.10	0.03	0.14	0.14	49
NWA 3118 (CV3 chondrite)											
leachate 2	-6.9	9.5	9.5	94	-0.15	0.36	0.01	0.04	0.25	0.05	55
Residue	-32.4	155.3	155.3	6	-0.82	0.76	0.06	0.04	0.59	0.06	45

The CAIs analyzed in this study span a range in $\varepsilon^{180}Ta$ from -1 to +63 (Table 4.4). The CAIs 4 and 5 from NWA 3095 can be resolved from the terrestrial value at their external reproducibility. CAIs 1, 3, and 5 seem to exhibit a common positive anomaly of *ca.* + 20 $\varepsilon^{180}Ta$. Allende CAIs A-33 and A-44, however, overlap the terrestrial value. Peters et al. (2016) published isotope data for Hf on the same set of CAIs, which is further used to compare and constrain the origin of the Ta isotopes anomalies. Please note, that CAI-2 was excluded due to contamination by the mixed HFSE-spike during sample preparation and CAI-6 was not measured for its Ta isotope composition.

Table 4.4 Tantalum isotope data from CAIs analyzed in this study together with Hf and W data, taken from Peters et al. (2016). Measured Ta isotope compositions were normalized to doped $^{171}Yb/^{173}Yb$, and Hf and W are internally normalized to $^{179}Hf/^{177}Hf$ and $^{184}W/^{186}W$, respectively. A-33 and A-44 have not been analyzed for their Hf and W isotope compositions and Ta isotopes of CAI-6 were not measured.

	Tantalum isotopes			**Hafnium isotopes**				**Tungsten isotopes**	
	$\varepsilon^{180}Ta$	±	ext. rep. (ε)	$\varepsilon^{174}Hf$	±	$\mu^{180}Hf$	±	$\mu^{183}W$	±
CAI-A33	0.3	10.7	10.7	-	-	-	-	-	-
CAI-A44	-0.8	12.2	12.2	-	-	-	-	-	-
CAI_C-BN_1	17.8	69.7	69.7	2.0	9.9	13	35	28	16
CAI_C-BN_3	23.4	13.8	13.8	-3.0	3.6	30	21	25	13
CAI_C-BN_4	62.7	8.6	11.6	-4.1	0.8	-2	6	6	8
	51.5	7.0	9.3	-4.5	0.8	-4	5		
Weighted Mean	56.0	5.4		-4.3	0.2	-3	1		
CAI_C-BN_5	23.2	9.1	9.2	-1.5	0.7	36	7	-7	10
	21.7	10.2	10.1						
Weighted Mean	22.5	6.8							
CAI_C-BN_6	-	-	-	-1.0	0.9	25	8	11	16

4.4 DISCUSSION

Tantalum only has two stable isotopes. Thus, mass-dependent and mass-independent isotope effects cannot be unambiguously distinguished. Here, we compare Ta isotope anomalies with isotope data for other elements in CAIs to identify the potential process leading to Ta isotope fractionation and discuss processes in the early solar system that may account for the Ta isotope data.

4.4.1 Processes leading to elemental fractionation of HFSE in CAIs

As reported in chapter 4.3.2, the extended HFSE pattern in CAIs cannot solely be explained by condensation from a hot solar nebula. Some features like Zr and Hf depletion can be directly related to type II REE patterns, indicating that the same processes acted at least for some of the REE and HFSE. The variability in W, U, Mo, and the fractionation of Nb from Ta, however, suggests processes beyond pure condensation and removal of ultra-refractory phases. Kornacki and Fegley (1986) observed discrepancies in the calculated condensation temperatures of Nb and U and their enrichment over CI chondrite relative to other refractory elements, which let them assign a higher volatility to Nb and U. Whereas the extended HFSE are relatively immobile in aqueous solutions, U is

an exception, as it is highly soluble in terrestrial systems in its oxidized U^{6+} state. NWA 3095 experienced terrestrial weathering, which might have influenced U in contrast to the other elements of the extended HFSE set. Indeed, CAI-4 is constantly enriched in HFSE at *ca.* 16 to 20 times CI-chondritic, while U is the only element with a lower enrichment factor. Possibly, the solutions on the meteorite parent body were sufficiently oxidizing to leach part of the U, which might explain the larger variability compared to immobile Th and Ta. Jacobsen *et al.* (2008) observed variable $^{232}Th/^{238}U$ ratios (the κ-value, back-calculated from Pb isotope measurements) in different CAIs, while the ratio was constant in leachates of the same CAI. They attributed this to a presolar origin of the ratio in each CAI inherited from an interstellar dust reservoir. Considering galactical chemical evolution, the measured U/Th ratios in Jacobsen *et al.* (2008) were reasonable with respect to the age of the galaxy. However, the larger spread in elemental ratios in this study is inconsistent with the age of the universe. The most conclusive explanation is a condensation origin of the U/Th in their analyzed set of CAIs, where subsequent elemental fractionation during CAI reprocessing and melting between minerals either did not take place or the distribution coefficients of U and Th into growing minerals were almost identical.

Tungsten is assumed to condense first in a refractory metal alloy, although it is not as depleted as the most refractory lithophile elements Zr, Hf, Er, Ho, Y, Dy, Tb, and Gd. These elements are assumed to have been removed by an ultra-refractory phase like perovskite or hibonite (Boynton, 1975). In contrast to lithophile refractory elements, W condensed in ultra-refractory metal nuggets, which must have survived fractionation from later condensing elements. Possibly, early hibonite or perovskite were easier to separate from the CAI reservoir by a physical process due to their larger sizes than the sub-µm metal grains hosting the W. After condensation and preservation of W in the CAI forming region, a second process caused the observed depletion. CAI-3 might give a hint to volatility controlled processes, as it exhibits a negative Ce anomaly, typical for more oxidizing conditions (Davis *et al.,* 1982). An important role of oxygen fugacity has recently been inferred to be of importance for W and Mo concentrations in refractory inclusions and is assumed to be a primary condensation feature (Fegley and Palme, 1985). Molybdenum is always more depleted than W, in accord with thermodynamical calculations (Fegley and Palme, 1985). However, this model is in contradiction to the very low oxygen fugacity, inferred from the high Ti^{3+}-in-fassaite data. An explanation might be a later transport of Mo, W, and Ce in a more oxidized nebular reservoir during CAI reprocessing, as suggested from the low-Ti^{3+} fassaite in this study and the more oxidized Wark-Lovering-rims around CAIs (Simon *et al.,* 2005), tracing changing oxygen fugacity during the histories of single CAIs. In this scenario, not all of the CAI can have been re-equilibrated with the solar nebula, either due to only partial melting or due to short timescales of melting. The scenario of partly more oxidizing conditions is in accord with lacking Eu and Yb anomalies in the REE patterns. Possibly, the

approach in sampling all the CAI led to incorporation of later condensed or more oxidized material, where either the more volatile Eu^{2+} or the then oxidized Eu^{3+} was later condensed in CAI rims or adjacent matrix. The alternative of aqueous mobilization of W on the parent body is considered as unlikely. In such a case, the Hf-W systematics would have been disturbed during significantly later parent body alteration while ^{182}Hf was still extant (Hutcheon, 1998). In this study, the W and Mo depletions are only found in the CAIs with type II patterns, but this is considered as coincidence, taking into account the original publication with W-Mo depletion reported for all CAI groups (Fegley and Palme, 1985).

The fractionation of Nb relative to Ta has recently been observed in bulk CV chondrites, ranging from 15.8 to 17.5, and was explained by addition of refractory material with distinctively low Nb/Ta (Münker *et al.,* 2003; Stracke *et al.,* 2012). The depletion of Nb over Ta relative to CI chondrites is also pronounced in the CAIs analyzed in this study (Nb/Ta = 7.75 to 18.3), the most in CAIs with group II REE patterns. Like it is apparent with the REE, elemental characteristics of HFSE inherited from CAIs are also visible on the bulk rock scale in CV chondrites, especially for Nb/Ta. Applying a mass balance approach with 3% molar abundance of CAIs in CV3 chondrites (Hezel *et al.,* 2008) and typical CI-chondritic concentrations of Nb and Ta (Palme *et al.,* 2014), we model a bulk CV Nb/Ta of 17.1 using the average Nb and Ta concentrations of CAI-1 to 5. This is well within the range previously observed and underlines the impact of refractory material on bulk trace element concentrations in the CV chondrite group (Münker *et al.,* 2003; Stracke *et al.,* 2012). Larger spread in Nb/Ta previously reported in Allende can be well explained by variable contributions of different CAI types in heterogeneous samples splits (Stracke *et al.,* 2012).

The fractionation of Nb from Ta is generally consistent with the somewhat higher volatility of Nb relative to Ta, where Nb is not yet fully condensed in CAIs showing type II REE patterns (Kornacki and Fegley, 1986). However, it is ambiguous why more volatile elements like Eu and Yb are enriched in the analyzed set of CAIs compared to Nb. The initial thermodynamical calculations consider Nb as being present in Nb^{2+} and Nb^{3+} state, while Ta exists in its oxidized 5+ state. The inferred 50% condensation temperatures of Nb and Ta differ by only 14K with Nb being assumed in the models to exclusively condense in titanate whereas Ta is assumed to condense in both hibonite and titanate (Lodders, 2003). Possibly, the redox state and resulting chemical bonding environment of Nb and Ta in either the gas phase or the first condensates plays a larger role than inferred from physical calculations. This might lead to stronger fractionation between the elemental twins Nb and Ta due to preferences for different condensing phases. As the difference of 14K in condensation temperatures seems to be too small to generate significant effects, a physical process might then separate the different phases containing Nb and Ta. In addition, Ta is, compared to Nb, affected differently by fractionation of presumed ultra-refractory phases, although it is neither an ultra-refractory, nor a

more volatile element in terms of condensation models (Fig. 4.4; Kornacki and Fegley, 1986). By comparing Nb and Ta relative to an index of fractionation (here Sm/Er, where Er is fractionated from Sm in Group II patterns), Nb is more easily depleted relative to Ta, but stays relatively constant while Ta concentrations further decrease with increasing Sm/Er. The Nb/Ta elemental ratio first changes to lower than CI-chondritic values, but again approaches CI values at higher degrees of ultra-refractory fractionation. This underlines the assumption that either different phases host the Nb-Ta or different processes during condensation control elemental fractionation of Nb and Ta.

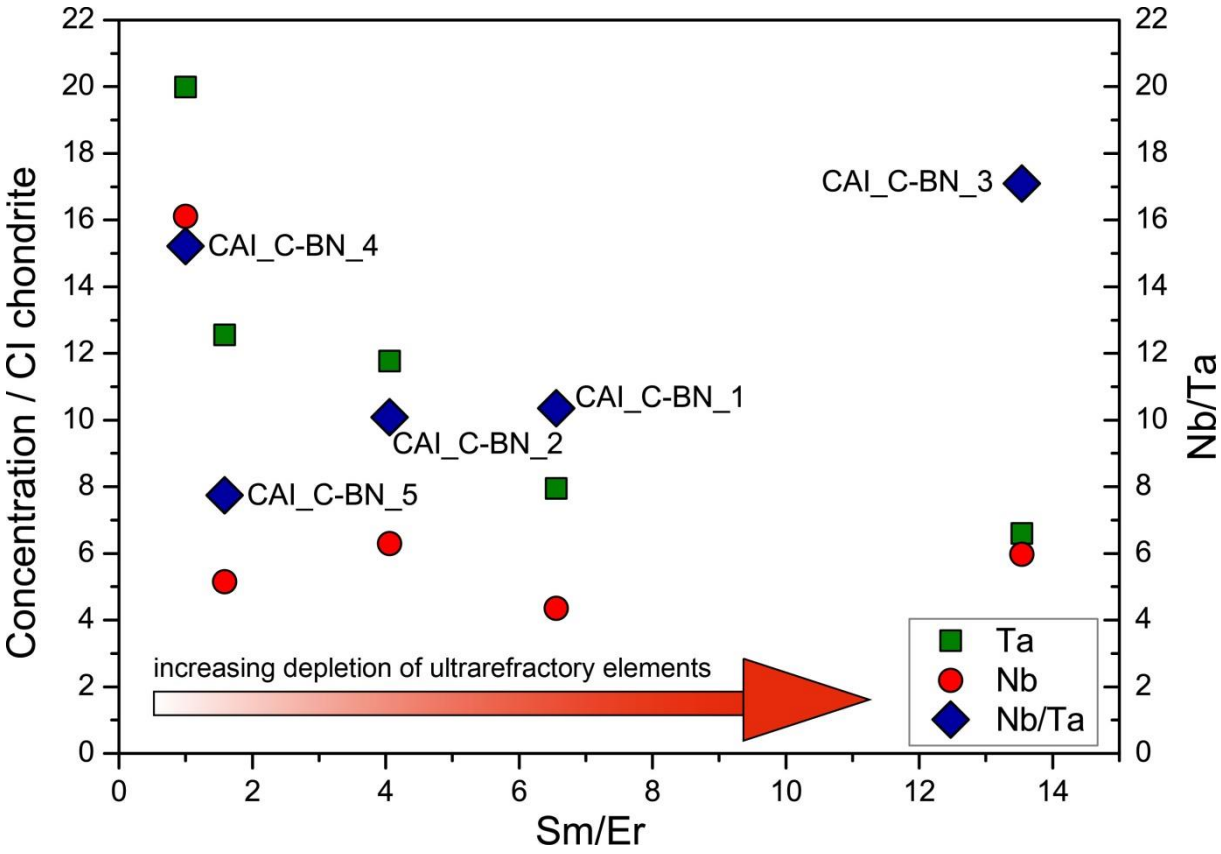

Fig. 4.4 Niobium and Ta concentrations normalized to CI-chondritic values and the elemental Nb/Ta ratio as a function of increasing refractory element depletion, indicated by increasing Sm/Er CI-chondritic ratios. Tantalum becomes further depleted, whereas Nb is relatively constant after initial depletion. This results in a steady increase of Nb/Ta ratios with further refractory element depletion.

In the light of the complex trace element patterns that are more complex than would be expected from pure condensation processes, further parameters like oxidative evaporation and aqueous mobilization seem to exert some control on trace element abundances in CAIs. Furthermore, affinities of elements during condensation might differ from phases predicted in thermodynamical calculations, and this bias may possibly be related to different oxidation states. Combination of W concentration and isotope data (Fig. 4.5) supports the assumption that larger CAIs

are processed over longer timescales causing homogenization of W isotopes, *i.e.*, nucleosynthetic components become diluted with increasing W concentrations and time (Peters *et al.*, 2016). This is also in accord with models that larger CAIs resided for prolonged timescales in the CAI forming region (Charnoz *et al.,* 2015). Multi-stage evolution of CAIs with episodes of re-heating, re-melting, evaporation, and reactions in regions with higher dust/gas ratio (*e.g.*, Kennedy *et al.,* 1997; Ireland and Fegley, 2000; Wakaki *et al.,* 2013) can viably explain the diversions from simple condensation models in refractory element patterns. Importantly, in contrast to earlier work, the full CAIs were sampled here, also including the outer portions with possibly larger imprints of secondary processes.

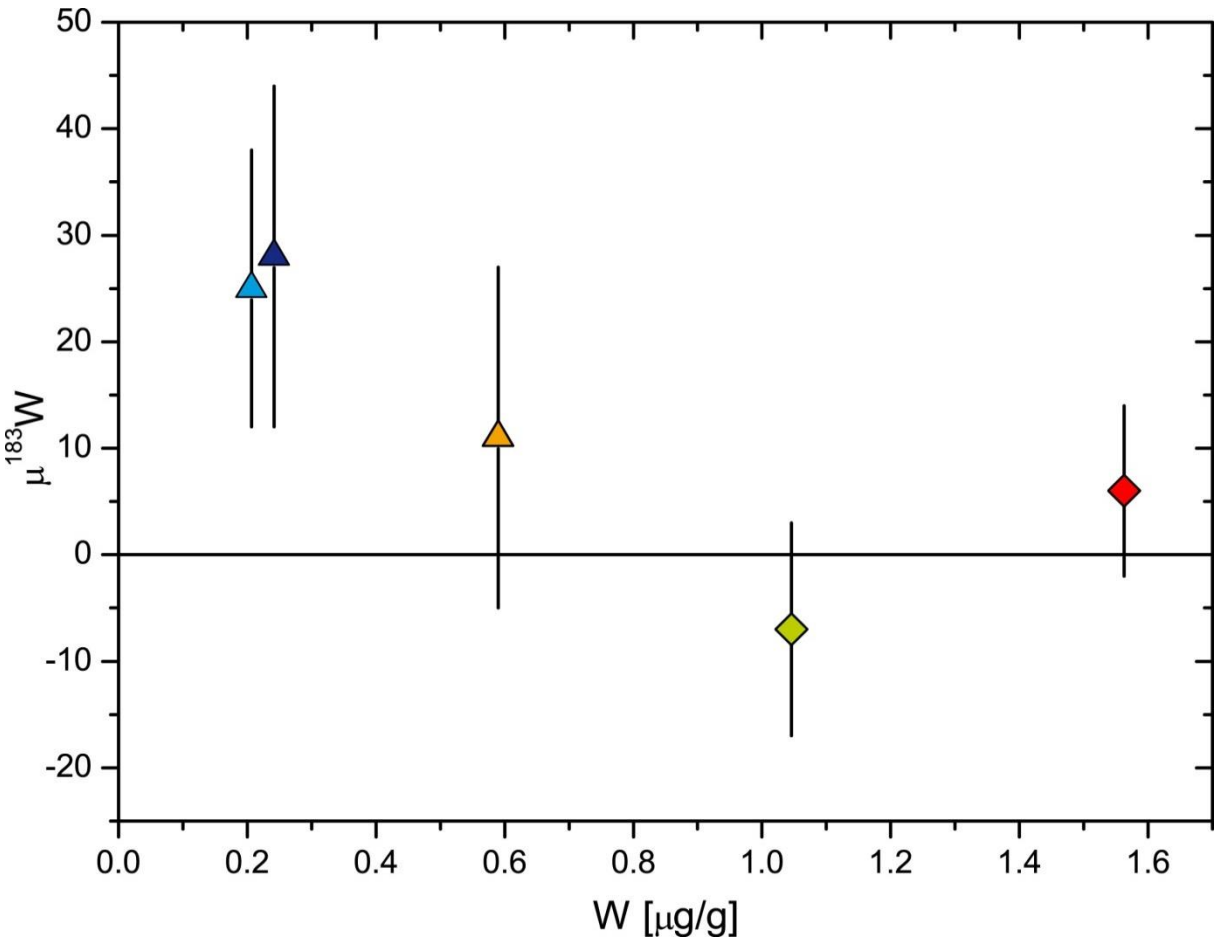

Fig. 5 Tungsten measured $\mu^{183}W$ versus concentrations in CAIs as a proxy for nucleosynthetic heterogeneity (taken from Peters et al. 2016). Refractory inclusions with higher W concentrations do not show resolvable variations in ^{183}W, which is indicative of dilution and homogenization effects during processing of CAIs.

4.4.2 Quality assessment of Ta isotope measurements and potential stable Ta isotope fractionation

The set of samples investigated in this study underwent secondary processes, which might have altered their primary isotope compositions. Inclusion CAI-1 was affected by aqueous alteration and parent body metamorphism and CAIs 4 and 5 in NWA 3095 have been exposed to terrestrial weathering. Nonetheless, all CAIs show isotope anomalies distinct from bulk meteorites and terrestrial rocks. This is clear evidence for sufficient immobility under aqueous conditions of the elements analyzed in this study (Hf, Ta, and W). Furthermore, intense alteration or weathering would lead to dilution, mixing, and eventually erasure of anomalous isotope signals. Potential artificial isotope fractionation during laboratory treatment, e.g., during leaching of the bulk meteorites or chemical separation, can be excluded. These possible analytical artefacts were evaluated using the isotopically unfractionated leached terrestrial basalt (Table 4.3) and earlier tests of the purification protocol (see chapter 3.2.4.3). Stable Tantalum isotope fractionation was found to be negligible at our level of analytical precision for terrestrial rocks and bulk meteorites (see chapter 3.3). Thus, processes like igneous equilibrium fractionation and subsequent segregation of minerals from molten CAIs can be considered as irrelevant.

Calcium-Aluminum-rich inclusions condensed from a solar gas and encountered subsequent evaporation events (e.g., Ireland and Fegley, 2000). In theory, during the physical transition between gaseous and solid state, the lighter isotopes are preferentially present in the gas phase, while the heavy isotopes are enriched in the condensate or residue (Urey, 1947). Evaporation-induced kinetic isotope fractionation was indeed observed for major refractory elements like Ca or Ti (Niederer and Papanastassiou, 1984; Niemeyer and Lugmair, 1984; Niederer *et al.,* 1985) and was reproduced in laboratory experiments (Zhang *et al.,* 2014). These elements are enriched in their heavy isotopes in the evaporation residues. Tantalum isotopes in CAIs, however, are lighter than bulk meteorites and terrestrial rocks, opposite to what is expected. However, further stable isotope work has been performed on more volatile elements in CAIs like Sr, Ba, and Eu, which show enrichments of the lighter isotopes if compared to meteorites (Patchett, 1980; Moynier *et al.,* 2006; Moynier *et al.,* 2015). For these elements, the isotope fractionation has been inferred to be caused by electromagnetic sorting, a process dependent on the first ionization potential of these elements. In case of Ta, however, the first ionization potential is too high to make this effect a reasonable explanation for isotope fractionation (Moynier *et al.,* 2006; Moynier *et al.,* 2015).

Of the extended HFSE and U-Th, only Uranium has been investigated for its stable isotope composition in CAIs. The differences encountered in $^{238}U/^{235}U$ were attributed to the decay from ^{247}Cm present in the early solar system (Brennecka *et al.,* 2010; Tissot *et al.,* 2016) but some of the

variation is considered being related to incomplete condensation of U from the solar gas, where an ultra-refractory component with heavy isotopic composition has been removed (Connelly *et al.,* 2012; Tissot *et al.,* 2016). If heavy Ta isotopes were removed by an early condensate, the light Ta isotope signatures should increase with decreasing concentrations. In our data set, however, the Ta isotope composition is not correlated with Ta concentration (Fig.4.6). The largest Ta isotope anomaly is observed in the unfractionated CAI-4 and there is no correlation evident with Sm/Er, arguing against stable isotope fractionation with increasing separation of refractory mineral phases.

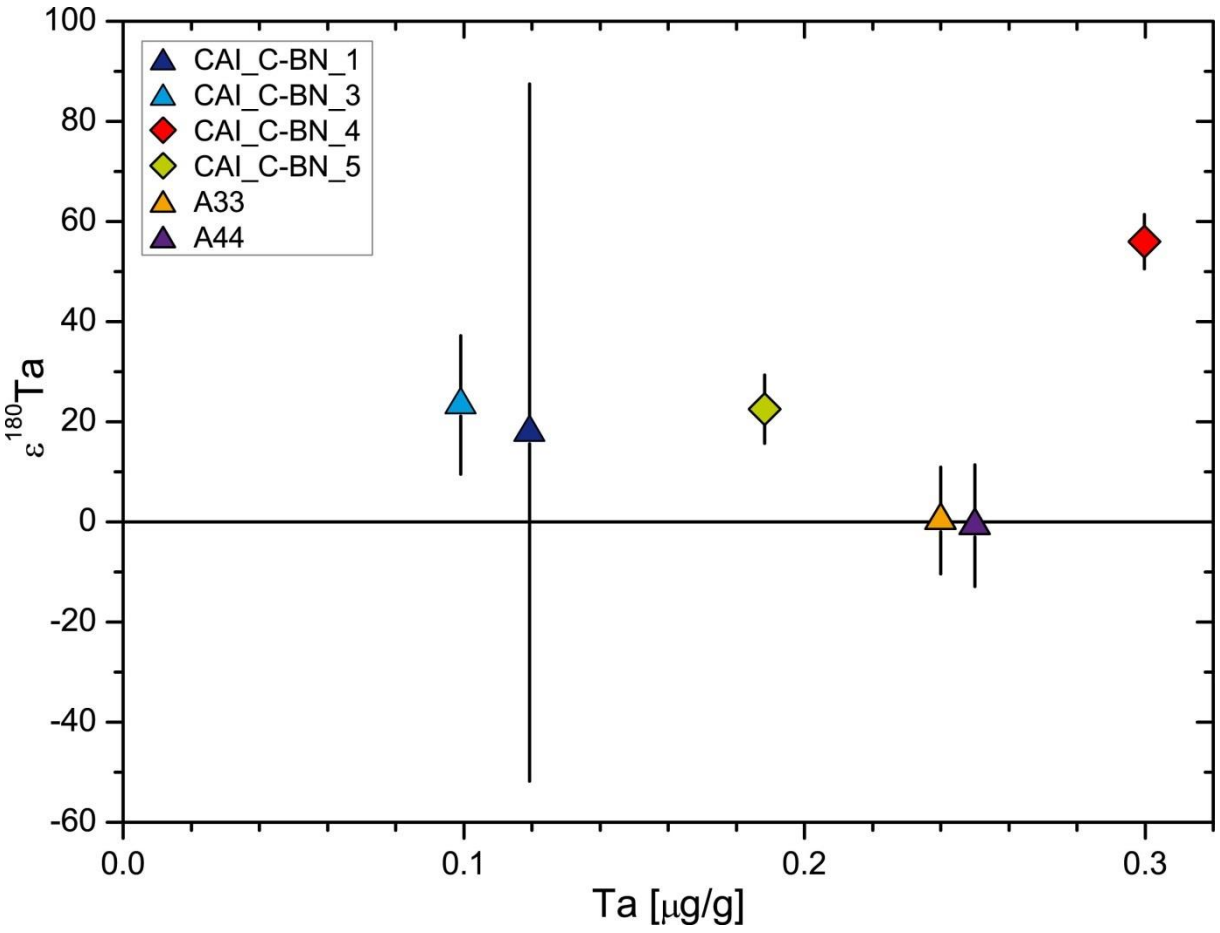

Fig. 4.6 Tantalum concentration against isotope composition of the individual CAIs. The Ta isotope compositions are not correlated with the Ta concentrations in the CAIs.

The measured positive ε^{180}Ta, *i.e.*, an enrichment of the light isotope, argues against an evaporation-related fractionation of Ta isotopes, and no correlation with Ta concentration or Sm/Er excludes a condensation scenario. These lines of evidence suggest that stable isotope fractionation was not a factor in fractionating the Ta isotope composition.

4.4.3 Nucleosynthetic Ta components in meteorites

Objects in the solar system are known to exhibit ubiquitous nucleosynthetic anomalies, particularly on the component scale of meteorites (see Dauphas and Schauble, 2016; and references therein for a recent review). Tantalum isotope anomalies might be inherited from their stellar site of production. However, direct identification of the source lacks more stable isotope fingerprinting in order to identify the exact process (*e.g.*, for Mo, Burkhardt *et al.,* 2011). Here, we compare the Ta with high-precision complementary Hf and W isotope data on the same samples to infer if Ta correlates with anomalies of other elements clearly associated with nucleosynthetic components.

Elfers et al. (in review) identified s-process anomalies in chondritic meteorite leachates and related them to s-process variations. A plot of ε^{180}Ta vs. ε^{174}Hf reveals a weak positive correlation (Fig. 4.7; Note that ^{174}Hf is a p-process nuclide but the anomalies are related to the normalization to s-process-influenced isotopes during measurements). The correlation might therefore be attributed to a common carrier phase of s-process Ta and Hf. By modeling the measured Hf isotope pattern by addition and subtraction of an s-process component from isotopically normal solar system Hf, the isotope variations can be explained by (un-)mixing of *ca.* ±1 per mil of s-process material. The co-variation can be caused by the s-process signature in Hf and Ta being carried in the same mineral phase, being condensed in the outflows of an AGB star and being present as presolar grains in primitive meteorites. Most recent models of the s-process assume 84% of ^{180}Ta and 47% of ^{181}Ta are derived from the s-process, thus, s-process excess does indeed result in positive ε^{180}Ta (Bisterzo *et al.,* 2014 updated with the new solar system abundance of ^{180}Ta, see chapter 2.3.4). However, the anomalies in Ta are much larger than those for Hf, which seems counterintuitive as s-process Hf and Ta are both present to comparable percentages in the solar system (Bisterzo *et al.,* 2014). A viable scenario is that elemental ratios in phases incorporating both elements in stellar environments were different. The carrier of the isotope anomalies present in our samples studied must have incorporated significantly more Ta than Hf, tentatively suggesting different condensation behavior of Hf and Ta in a circumstellar environment. Moreover, the high Ta/Hf phase would have been more resistant to destruction in the interstellar medium than the low Ta/Hf phase prior to solar system formation. However, we note that the obtained data set with the leaching protocol applied here is limited, as only two samples show Ta isotope compositions resolved outside the external reproducibility. Furthermore, the precision is too low to identify the complementary reservoir of the resolved Ta anomalies. The intercept resolved from the terrestrial origin in the plot of ε^{180}Ta vs. ε^{174}Hf might hint at analytical artefacts during these measurements.

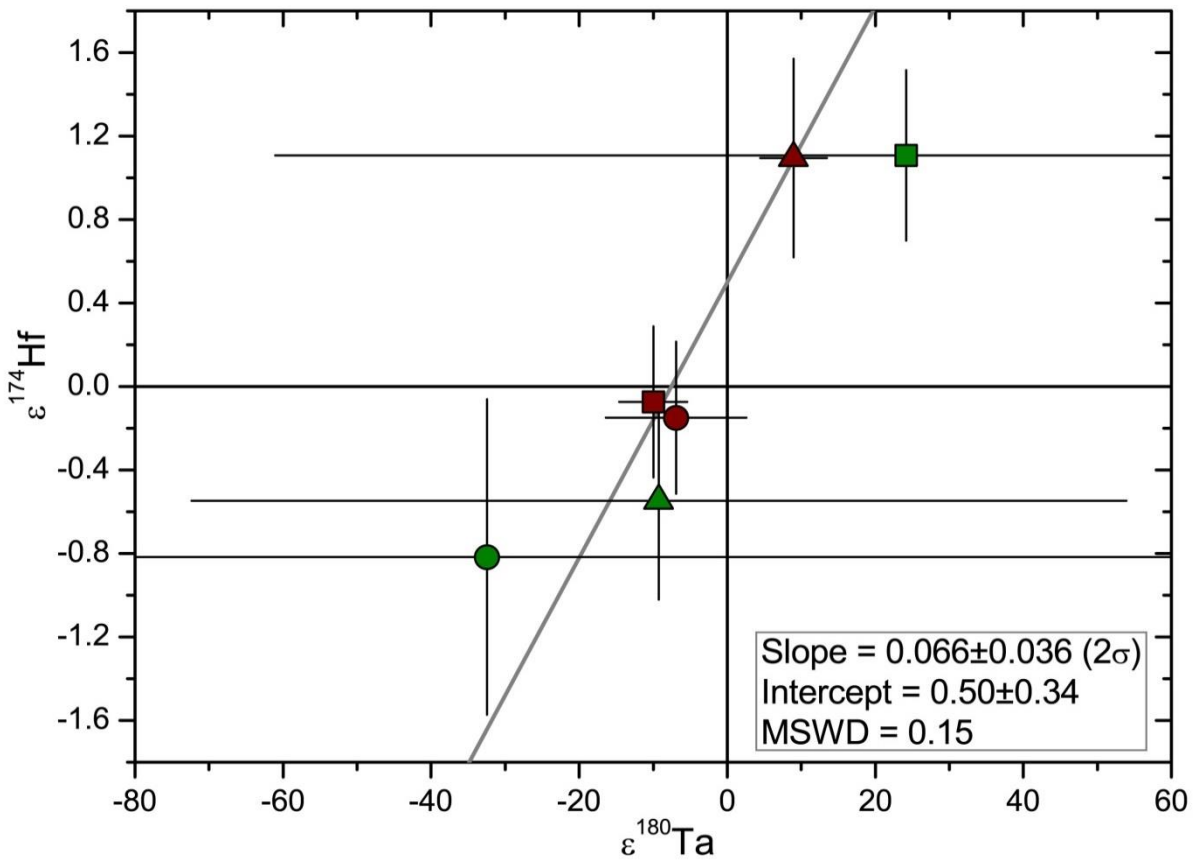

Fig. 4.7 Isotope anomalies of ^{180}Ta vs. ^{174}Hf in cuts from the leaching experiments. The data are only weakly resolved and form two fields. The grey slope is the weighted correlation through the data set. Note that the error bars of the residues are larger than shown in the diagram. Symbols are the same as in Fig. 4.3.

In contrast to leaching data, two of the CAIs show clearly resolved positive ε^{180}Ta. However, ε^{180}Ta is not correlated with any Hf or W isotope anomalies, arguing against a common origin of Hf and Ta isotope anomalies (Fig. 4.8). Peters *et al.* (2016) have recently shown for the same set of CAIs that ^{174}Hf is decoupled from pure s- and r-process isotope variations. As both ^{180}Ta and ^{174}Hf have at least in part a p-process origin, differences in this component seem likely. However, even when using the ^{174}Hf data corrected for other nucleosynthetic components from Peters *et al.* (2016), still no correlation with ^{180}Ta is observed (Fig. 4.8a). Alternatively, a deficit in ^{181}Ta results in positive ε^{180}Ta. This requires a larger deficit in r-process material, which is considered less likely as such extents in r-process anomalies have not been observed in isotopes of neighboring elements, e.g., Hf and W (Burkhardt *et al.,* 2008; Akram *et al.,* 2013; Kruijer *et al.,* 2014; Peters *et al.*, 2016).

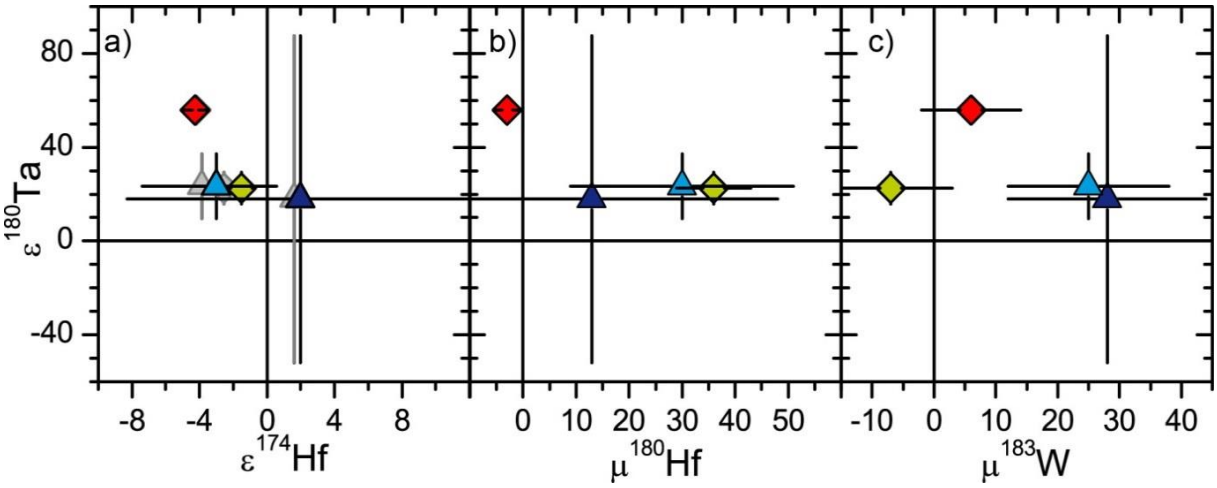

Fig. 4.8 Isotope anomalies of ε^{180}Ta in CAIs plotted against a) ε^{174}Hf, b) μ^{180}Hf, and c) μ^{183}W. The Hf and W data are taken from Peters *et al.* (2016). The grey symbols in a) indicate the s- or r-process corrected ^{174}Hf data after the model from Wisshak *et al.* (2006; Peters *et al.*, 2016) and measured μ^{180}Hf anomalies, giving the residual p-process ^{174}Hf component. Symbols are the same as Fig. 4.3.

An approach to explain the differences in ^{174}Hf and ^{180}Ta from a nucleosynthesis perspective is to consider the exact processes of nuclide production. Hafnium-174 is a typical p-process nuclide produced during photodisintegration, *i.e.*, the ejection of protons out of seed nuclei by high-energetic photons during supernova explosions (*e.g.*, Rayet *et al.,* 1995; Arnould and Goriely, 2003; Rauscher *et al.,* 2013). Tantalum-180 is the only heavy nuclide beside ^{138}La that is produced during neutrino nucleosynthesis, where the seed nucleii interact with neutrinos (*e.g.*, Woosley *et al.,* 1990; Heger *et al.,* 2005; Kajino *et al.,* 2014). This production pathway is uncommon due to the very low rate of interactions of neutrinos and requires high neutrino fluxes, which is only achieved during formation of a neutron star in supernova explosions. Recent work on ^{138}La in CAIs revealed a resolved excess of up to ~50 ε^{138}La and a correlation with ^{48}Ca and ^{50}Ti that was interpreted as an incorporation of presolar carriers enriched in ejecta of a core-collapse type II supernova (cc SNe II; Shen and Lee, 2003; Chen *et al.,* 2015). As a portion of ^{180}Ta is produced by the ν-process, excess of both nuclides in CAIs would seem reasonable.

Taking further heavy p-nuclides into account, nucleosynthetic anomalies from the ν-process are considered less likely. Some heavy p-nuclides were shown to be depleted in normal CAIs, e.g. Nd, Sm, and Hf (Brennecka *et al.,* 2013; Peters *et al.*, 2016) whereas ^{138}La and ^{180}Ta as ν-process nuclides are enriched in CAIs. This would require a decoupling between the gamma-process (γ-process) and the ν-process, although both are considered to take place in explosive O-Ne shell burning during cc SNe II for the nuclides discussed above (e.g., Woosley *et al.,* 1990; Rauscher *et al.,* 2013). There is no evidence for a physical processes leading to specific nuclide separation during SNe. Fractionation

during condensation of presolar grains is also unlikely as separation of La from other REE and Ta from other HFSE cannot be achieved.

Collectively, the magnitude of Ta isotope anomalies in CAIs is much larger than the nucleosynthetic isotope anomalies of Hf or W (only a few ε in the same samples). Deviations in ^{180}Ta do not correlate with isotope anomalies in other p-process nuclides produced in the γ-process, arguing against ν-process related excesses originating from O-Ne shell burning during cc SNe II. Although it is not possible to exclude nucleosynthetic ν-process isotope anomalies in ^{180}Ta, we consider it less likely. In contrast to nucleosynthetic W anomalies, Ta isotope anomalies do not diminish with increasing elemental concentration and homogenization (Fig. 4.5; 4.6). This points to a process independent of initial nucleosynthetic heterogeneity in the protosolar nebula.

4.4.4 Irradiation of CAI-forming region from nascent sun

Meteorites might have been subjected to intense irradiation, either in the early solar system or after parent body break-up. It has been discussed that γ-irradiation in the early solar system might be responsible for disturbances in Lu-Hf systematics of meteorites (Albarède *et al.,* 2006), which could also have changed the Ta isotope ratio due to an isomeric transition of ^{180}Ta to its unstable ground state. However, this scenario was excluded for ^{176}Lu by the study of Bast *et al.* (2017; chapter 3.4.2). The neutron capture cross sections of the Ta isotopes are lower than the cross sections of Hf isotopes, which can be measured at significantly higher precision (Peters *et al.*, 2016). All Hf analyses presented here show no signs of neutron capture, making this effect negligible for altering the Ta isotope composition.

An interesting approach to explain the Ta isotope anomalies is solar flare induced proton irradiation from the accreting proto-sun during the time of CAI formation (Shu, 1997; Lee *et al.,* 1998; Gounelle *et al.,* 2001). The particles were energetic enough (several to tens of MeV per nucleon) to produce short-lived isotopes through spallation reactions, as evident from extinct ^{10}Be and possibly ^{7}Be in CAIs, which cannot originate from a stellar source (McKeegan, 2000; Chaussidon *et al.,* 2006). The early theoretical papers of Lee *et al.* (1998) and Gounelle *et al.* (2001) also discussed the possibility of production of ^{50}V and ^{138}La. This was the initial motivation to study La isotopes in CAIs (Shen and Lee, 2003) and an excess of ^{50}V was indeed recently reported (Sossi *et al.*, 2016). Vanadium-50, ^{138}La, and ^{180}Ta are odd-odd-nuclides, which are orders of magnitude lower in abundance than the stable isotopes ^{51}V, ^{139}La, and ^{181}Ta. Furthermore, they sit on an interstitial position in the chart of nuclides, where they can be accessed by production on much more abundant isotopes ^{49,50}Ti, ^{138}Ba, or ^{180}Hf by (p,γ) or (p,n) reactions (Gounelle *et al.,* 2001). The large abundance of parent nuclides and the tiny amounts of daughter nuclides, as expressed by the large isotope

differences of V, La and Ta make them ideal test sites for nucleogenic ingrowth. Here, we suggest that Tantalum isotope anomalies might be a further recorder of early irradiation in the solar system.

A problem in this model arises from the production yields of stable ^{180}Ta from ^{180}Hf. Even though photons of sufficient energy are assumed to have been present in the early solar nebula, the ^{180}Ta likely to be produced would largely be present in its nuclear ground state, which decays with a half-life of *ca.* 8 hours back to ^{180}Hf and to a minor degree to ^{180}W (Takács *et al.,* 2011; Shahid *et al.,* 2014). Still, ^{180}Hf is 21,000 times more abundant in the solar System than ^{180}Ta, which might be sufficient to resolve nucleogenic ingrowth even at production rates of the isomeric state of less than 1 %.

In contrast to nucleosynthetic isotope anomalies in W, larger CAIs with higher Ta concentrations might show larger Ta isotope anomalies compared to smaller ones (Fig. 4.5, 4.6). Statistical evaluation of the CAI content and sizes in Allende indicates that larger CAIs experienced longer times in the CAI forming region (Charnoz *et al.,* 2015). Smaller and fine-grained inclusions were rapidly separated from the CAI-forming region and carry larger isotope anomalies inherited from condensation. In contrast, the larger grains are likely to have been irradiated more often by solar flares, while nucleosynthetic components were diluted during repeated melting, fragmentation, and coagulation. This might allow progressive ingrowth in ^{50}V, ^{138}La and ^{180}Ta by irradiation and contemporaneous erasure of nucleosynthetic isotope anomalies.

4.4.5 Approaching the processes responsible for isotope anomalies in the early solar system

Both possible explanations of nucleosynthetic anomalies and early irradiation involve major problems. For nucleosynthetic anomalies, Ta isotope anomalies seem to be too large for an s-process component and a correlation of ε^{180}Ta with other p-process nuclides is still lacking. In case of the irradiation scenario, the production of isomeric ^{180}Ta might be insufficient. The way to disentangle the source of ^{180}Ta anomalies in further studies would therefore be a multi-isotopic approach on the same samples. Particularly our potential to combine the isotope data with high-precision concentration data allows normalization of possible irradiation production to the parent/ daughter isotope ratios of each nuclear reaction system.

Table 4.5 lists the isotopes of interest and their production pathways during irradiation in the solar nebula and their production in stars. The strongest evidences for early irradiation are the decay products of in-situ produced ^{10}Be and ^{7}Be (McKeegan, 2000; Chaussidon *et al.,* 2006). Sossi *et al.* correlated for the first time ^{10}Be in CAIs with an excess in ^{50}V (Sossi *et al.*, 2016), giving a strong

argument for ^{50}V production in the early solar system. To distinguish between nucleosynthesis and irradiation for La and Ta, a correlation of the parent-normalized anomalies with V anomalies should be visible if the irradiation scenario is valid. If La and Ta anomalies are exclusively of nucleosynthetic origin, a correlation with V will not necessarily be observed. Vanadium-50 production in massive stars is decoupled from ^{138}La and ^{180}Ta in space and time. Although ^{50}V is also partly produced during explosive Ne burning , the majority is bred in burning stages prior to the supernova event (Woosley and Weaver, 1995; Woosley *et al.,* 2002). Furthermore, measurements of Hf isotopes are important, as this permits checking with possible p-process anomalies for the γ-process that is assumed to take place in the same shell during cc SNe II (*e.g.*, Rauscher *et al.,* 2013).

Table 4.5 Isotopes of interest for investigation of isotope anomalies to discriminate between early irradiation and nucleosynthesis. The abbreviations ISM and GCR stand for interstellar medium and galactic cosmic rays. For references of the nuclide production, see text.

	Early solar system	**Galactical production**	
	Protosolar irradiation	Site	Process
^{7}Be, ^{10}Be	Spallation on ^{16}O etc	ISM	Spallation through GCR
^{50}V	soft p-γ on ^{49}Ti and ^{50}Ti	(Pre-)SNe II massive stars	C-burning; Ne (expl.) burning
^{138}La	p-n on ^{138}Ba	O-Ne shell in cc SNe II	ν-process
^{180}Ta	p-n on ^{180}Hf?	Higher mass AGB stars; O-Ne shell in cc SNe II	84% s-process branching; 16% ν-process
^{180}Hf, ^{180}W	None	O-Ne shell in cc SNe II	γ-process

Further support to the early irradiation model is also provided by the presence of bulk anomalies of V isotopes in meteorites (Nielsen *et al.,* 2014). Inner solar system objects like Earth are depleted in ^{50}V, which led the authors to the suggestion that irradiated material was transferred to the outer solar system and incorporated into carbonaceous chondrites. A multi-isotopic approach of CAIs and meteorites could allow distinguishing between irradiation-related isotope anomalies or a specific nucleosynthetic component. This might help to narrow down possible sources of differing vanadium isotope anomalies throughout early solar system materials.

4.5 CONCLUSIONS

High-precision HFSE concentration measurements in CAIs reveal a more complex history in the earliest solar system materials than would be inferred from a pure condensation model. Redox conditions and fractionation of elements into major condensing phases might differ from the theoretical canonical condensation model (Lodders, 2003). Subsequent processing of CAIs with repeated heating, melting, and transfer in the protoplanetary disk could further influence the distribution of refractory trace elements in CAIs.

We are not yet able to unambiguously resolve Ta isotope anomalies in leaching experiments of bulk powders of primitive meteorites. However, Ta isotope ratios tentatively correlate with Hf nucleosynthetic anomalies obtained for the same samples and might hint to a common carrier of s-process material for both elements in carbonaceous chondrites. This would support the view that ^{180}Ta is produced to a considerable part in the s-process. With the newly established solar ^{180}Ta isotope abundance of 0.0117% (chapter 2.3.4), the residual ^{180}Ta that cannot be modelled in s-process reaction networks can be reduced to 16% (using the recent s-process yields from Bisterzo *et al.,* 2014).

Two out of six measured CAIs did express significantly elevated ratios in Ta isotopes of up to ε^{180}Ta = 60. This is generally in accord with larger nucleosynthetic anomalies being present in earliest condensates of the solar system. In contrast to leaching data, no correlations of Ta isotope compositions with isotope compositions of other elements (Hf and W) were observed. The decoupling of Ta isotope ratios from other elemental anomalies might either hint to an exotic nucleosynthetic component derived from the ν-process or to in situ production of Ta.

Collectively, we therefore either suggest a more exotic ν-process nucleosynthetic component in the CAI forming region or that proton-irradiation in the early solar system may have been a more important process for in-situ nuclide production of nuclides than previously thought. Future combined isotope measurements of V, La, and Ta should disentangle the origin of the excesses observed in the rare odd-odd nuclides in CAIs (Nielsen *et al.,* 2014; Shen and Lee, 2003; this study).

5 References

Abraham, K., Barling, J., Siebert, C., Belshaw, N., Gall, L., Halliday, A. N. (2015) Determination of mass-dependent variations in tungsten stable isotope compositions of geological reference materials by double-spike and MC-ICPMS. *Journal of Analytical Atomic Spectrometry.* **30,** 2334–2342.

Akram, W., Schönbächler, M., Sprung, P., Vogel, N. (2013) Zirconium-Hafnium Isotope evidence from Meteorites for the decoupled synthesis of light and heavy neutron-rich nuclei. The Astrophysical Journal 777, 169.

Albalat, E., Telouk, P., Albarède, F. (2012) Er and Yb isotope fractionation in planetary materials. *Earth and Planetary Science Letters* **355-356,** 39–50.

Albarède, F., Scherer, E. E., Blichert-Toft, J., Rosing, M., Simionovici, A., Bizzarro, M. (2006) γ-ray irradiation in the early Solar System and the conundrum of the 176Lu decay constant. *Geochimica et Cosmochimica Acta* **70,** 1261–1270.

Albarède, F., Telouk, P., Blichert-Toft, J., Boyet, M., Agranier, A., Nelson, B. (2004) Precise and accurate isotopic measurements using multiple-collector ICPMS. *Geochimica et Cosmochimica Acta* **68,** 2725–2744.

Anders, E., Zinner, E. (1993) Interstellar Grains in Primitive Meteorites: Diamond, Silicon Carbide, and Graphite. *Meteoritics* **28,** 490–514.

Andreasen, R., Sharma, M. (2006) Solar Nebula Heterogeneity in p-Process Samarium and Neodymium Isotopes. *Science* **314,** 806–809.

Angeli, I., Marinova, K. (2013) Table of experimental nuclear ground state charge radii: An update. *Atomic Data and Nuclear Data Tables* **99,** 69–95.

Arlandini, C., Kappeler, F., Wisshak, K., Gallino, R., Lugaro, M., Busso, M., Straniero, O. (1999) Neutron Capture in Low-Mass Asymptotic Giant Branch Stars: Cross Sections and Abundance Signatures. *The Astrophysical Journal* **525,** 886–900.

Arnould, M. (1976) Possibility of synthesis of proton-rich nuclei in highly evolved stars. II. *Astronomy and Astrophysics* **46,** 117–125.

Arnould, M., Goriely, S. (2003) The p-process of stellar nucleosynthesis: astrophysics and nuclear physics status. *Physics Reports* **384,** 1–84.

Audi, G., Wapstra, A., Thibault, C. (2003) The Ame2003 atomic mass evaluation. *Nuclear Physics A* **729,** 337–676.

Ávila, J. N., Lugaro, M., Ireland, T. R., Gyngard, F., Zinner, E., Cristallo, S. et al. (2012) Tungsten isotopic compositions in stardust SiC grains from the Murchison meteorite: Constraints on the s-process in the Hf-Ta-W-Re-Os region. *The Astrophysical Journal* **744,** 49.

Barrat, J., Zanda, B., Jambon, A., Bollinger, C. (2014) The lithophile trace elements in enstatite chondrites. *Geochimica et Cosmochimica Acta* **128,** 71–94.

Bartels, A., Holtz, F., Linnen, R. L. (2010) Solubility of manganotantalite and manganocolumbite in pegmatitic melts. *American Mineralogist* **95,** 537–544.

Barth, M. G., McDonough, W. F., Rudnick, R. L. (2000) Tracking the budget of Nb and Ta in the continental crust. *Chemical Geology* **165,** 197–213.

Bast, R., Scherer, E., Bischoff, A. (2017) The 176Lu-176Hf systematics of ALM-A: A sample of the recent Almahata Sitta meteorite fall. *Geochemical Perspectives Letters* **3,** 45–54.

Bast, R., Scherer, E. E., Sprung, P., Fischer-Gödde, M., Stracke, A., Mezger, K. (2015) A rapid and efficient ion-exchange chromatography for Lu–Hf, Sm–Nd, and Rb–Sr geochronology and the

routine isotope analysis of sub-ng amounts of Hf by MC-ICP-MS. *Journal of Analytical Atomic Spectrometry* **30,** 2323–2333.

Beer, H., Ward, R. A. (1981) Neutron-capture nucleosynthesis of nature's rarest stable isotope. *Nature* **291,** 308–310.

Belic, D., Arlandini, C., Besserer, J., Boer, J. de, Carroll, J., Enders, J. et al. (1999) Photoactivation of 180Tam and Its Implications for the Nucleosynthesis of Nature's Rarest Naturally Occurring Isotope. *Physical Review Letters* **83,** 5242–5245.

Berglund, M., Wieser, M. E. (2011) Isotopic compositions of the elements 2009 (IUPAC Technical Report). *Pure and Applied Chemistry* **83,** 397–410.

Bigeleisen, J. (1996) Nuclear Size and Shape Effects in Chemical Reactions. Isotope Chemistry of the Heavy Elements. *Journal of the American Chemical Society* **118,** 3676–3680.

Bisterzo, S., Gallino, R., Straniero, O., Cristallo, S., Käppeler, F. (2011) The s-process in low-metallicity stars - II. Interpretation of high-resolution spectroscopic observations with asymptotic giant branch models. *Monthly Notices of the Royal Astronomical Society* **418,** 284–319.

Bisterzo, S., Travaglio, C., Gallino, R., Wiescher, M., Käppeler, F. (2014) Galactical chemical evolution and solar s-process abundances: Dependence on the 13C-pocket structure. *The Astrophysical Journal* **787,** 10.

Bizzarro, M., Baker, J. A., Haack, H., Ulfbeck, D., Rosing, M. (2003) Early history of Earth's crust–mantle system inferred from hafnium isotopes in chondrites. *Nature* **421,** 931–933.

Boyet, M., Carlson, R. W. (2005) 142Nd Evidence for Early (>4.53 Ga) Global Differentiation of the Silicate Earth. *Science* **309,** 576–581.

Boynton, W. V. (1975) Fractionation in the solar nebula: condensation of yttrium and the rare earth elements. *Geochimica et Cosmochimica Acta* **39,** 569–584.

Brearley A. J. and Krot A. N. (2013) Metasomatism in the early solar system: the record from chondritic meteorites. In: *Metasomatism and the Chemical Transformation of Rock – Lecture Notes in Earth System Sciences* (eds. Harlov, D. E., and Austrheim, H.). Springer. Heidelberg. 659–789.

Brenan, J., Shaw, H., Phinney, D., Ryerson, F. (1994) Rutile-aqueous fluid partitioning of Nb, Ta, Hf, Zr, U and Th: implications for high field strength element depletions in island-arc basalts. *Earth and Planetary Science Letters* **128,** 327–339.

Brennecka, G. A., Borg, L. E., Wadhwa, M. (2013) Evidence for supernova injection into the solar nebula and the decoupling of r-process nucleosynthesis. *Proceedings of the National Academy of Sciences* **110,** 17241–17246.

Brennecka, G. A., Weyer, S., Wadhwa, M., Janney, P. E., Zipfel, J., Anbar, A. D. (2010) 238U/235U Variations in Meteorites: Extant 247Cm and Implications for Pb-Pb Dating. *Science* **327,** 449–451.

Breton, T., Quitté, G. (2014) High-precision measurements of tungsten stable isotopes and application to earth sciences. *Journal of Analytical Atomic Spectrometry* **29,** 2284–2293.

Burbidge, E., Burbidge, G., Fowler, W., Hoyle, F. (1957) Synthesis of the Elements in Stars. *Reviews of Modern Physics* **29,** 547–650.

Burkhardt, C., Kleine, T., Bourdon, B., Palme, H., Zipfel, J., Friedrich, J. M., Ebel, D. S. (2008) Hf–W mineral isochron for Ca,Al-rich inclusions: Age of the solar system and the timing of core formation in planetesimals. *Geochimica et Cosmochimica Acta* **72,** 6177–6197.

Burkhardt, C., Kleine, T., Oberli, F., Pack, A., Bourdon, B., Wieler, R. (2011) Molybdenum isotope anomalies in meteorites: Constraints on solar nebula evolution and origin of the Earth. *Earth and Planetary Science Letters* **312,** 390–400.

Burnham, A. D., Berry, A. J., Wood, B. J., Cibin, G. (2012) The oxidation states of niobium and tantalum in mantle melts. *Chemical Geology* **330-331,** 228–232.

Cameron, A., Truran, J. (1977) The supernova trigger for formation of the solar system. *Icarus* **30,** 447–461.

Cartier, C., Hammouda, T., Boyet, M., Mathon, O., Testemale, D., Moine, B. N. (2015) Evidence for Nb 2+ and Ta 3+ in silicate melts under highly reducing conditions: A XANES study. *American Mineralogist* **100,** 2152–2158.

Cartier, C., Hammouda, T., Doucelance, R., Boyet, M., Devidal, J.-L., Moine, B. (2014) Experimental study of trace element partitioning between enstatite and melt in Enstatite-Chondrites at low oxygen fugacities and 5 GPa. *Geochimica et Cosmochimica Acta* **130,** 167–187.

Chakhmouradian, A. R. (2006) High-field-strength elements in carbonatitic rocks: Geochemistry, crystal chemistry and significance for constraining the sources of carbonatites. *Chemical Geology* **235,** 138–160.

Charnoz, S., Aléon, J., Chaumard, N., Baillié, K., Taillifet, E. (2015) Growth of calcium–aluminum-rich inclusions by coagulation and fragmentation in a turbulent protoplanetary disk: Observations and simulations. *Icarus* **252,** 440–453.

Chaussidon, M., Robert, F., McKeegan, K. D. (2006) Li and B isotopic variations in an Allende CAI: Evidence for the in situ decay of short-lived 10Be and for the possible presence of the short-lived nuclide 7Be in the early solar system. *Geochimica et Cosmochimica Acta* **70,** 224–245.

Chen, H.-W., Lee, T., Lee, D.-C., Chen, J.-C. (2015) CORRELATION OF 48 Ca, 50 Ti, AND 138 La HETEROGENEITY IN THE ALLENDE REFRACTORY INCLUSIONS. *The Astrophysical Journal* **806,** L21.

Chen, J., Papanastassiou, D., Wasserburg, G. (2010) Ruthenium endemic isotope effects in chondrites and differentiated meteorites. *Geochimica et Cosmochimica Acta* **74,** 3851–3862.

Collins, C., Eberhard, C., Glesener, J., Anderson, J. (1988) Depopulation of the isomeric state Tam180 by the reaction Tam180(γ,γ′)Ta180. *Physical Review C* **37,** 2267–2269.

Connelly, J. N., Bizzarro, M., Krot, A. N., Nordlund, A., Wielandt, D., Ivanova, M. A. (2012) The Absolute Chronology and Thermal Processing of Solids in the Solar Protoplanetary Disk. *Science* **338,** 651–655.

Dauphas, N., Davis, A. M., Marty, B., Reisberg, L. (2004) The cosmic molybdenum–ruthenium isotope correlation. *Earth and Planetary Science Letters* **226,** 465–475.

Dauphas, N., Marty, B., Reisberg, L. (2002) Molybdenum Evidence for Inherited Planetary Scale Isotope Heterogeneity of the Protosolar Nebula. *The Astrophysical Journal* **565,** 640–644.

Dauphas, N., Pourmand, A. (2015) Thulium anomalies and rare earth element patterns in meteorites and Earth: Nebular fractionation and the nugget effect. *Geochimica et Cosmochimica Acta* **163,** 234–261.

Dauphas, N., Schauble, E. A. (2016) Mass Fractionation Laws, Mass-Independent Effects, and Isotopic Anomalies. *Annual Review of Earth and Planetary Sciences* **44,** 709–783.

Davis, A. M., Grossman, L. (1979) Condensation and fractionation of rare earths in the solar nebula. *Geochimica et Cosmochimica Acta* **43,** 1611–1632.

Davis, A. M., Tanaka, T., Grossman, L., Lee, T., Wasserburg, G. (1982) Chemical composition of HAL, an isotopically-unusual Allende inclusion. *Geochimica et Cosmochimica Acta* **46,** 1627–1651.

Demartis, M., Melgarejo, J. C., Colombo, F., Alfonso, P., Coniglio, J. E., Pinotti, L. P., D'Eramo, F. J. (2014) Extreme F activities in late pegmatitic events as a key factor for LILE and HFSE enrichment: The Ángel Pegmatite, Central Argentina. *The Canadian Mineralogist* **52,** 247–269.

Desch, S. J., Morris, M. A., Connolly, H. C., Boss, A. P. (2010) A critical examination of the X-Wind model for chondrule and Calcium-Aluminum-rich inclusion formation and radionuclide production. *The Astrophysical Journal* **725,** 692–711.

Dill, H. G. (2010) The "chessboard" classification scheme of mineral deposits: Mineralogy and geology from aluminum to zirconium. *Earth-Science Reviews* **100,** 1–420.

Ekeberg, A. G. (1802) Ueber ein neues Metall, Tantalum, welches zugleich mit der Yttererde in einigen schwedischen Fossilien entdeckt worden ist; nebst einigen Anmerkungen über die Eigenschaften der Yttererde, in Vergleichung mit der Beryllerde. *Crells Annalen der Chemie* **1**, 1–21.

Elfers, B.-M., Sprung, P., Pfeifer, M., Wombacher, F., Peters, S. T. M., Münker, C. (2016) S -process variability in early solar system materials - evidence from 174Hf and 180W in sequentially leached primitive chondrites. *Geochimica et Cosmochimica Acta,* under review.

Fegley, B., Palme, H. (1985) Evidence for oxidizing conditions in the solar nebula from Mo and W depletions in refractory inclusions in carbonaceous chondrites. *Earth and Planetary Science Letters* **72,** 311–326.

Floss, C., El Goresy, A., Palme, H., Spettel, B., Zinner, E. (1992) An unusual Ca–Ti–Al silicate in a Type A Allende inclusion. *Meteoritics* **27**, 220.

Foley, S. F., Barth, M. G., Jenner, G. A. (2000) Rutile/melt partition coefficients for trace elements and an assessment of the influence of rutile on the trace element characteristics of subduction zone magmas. *Geochimica et Cosmochimica Acta* **64,** 933–938.

Fonseca, R. O., Mallmann, G., Sprung, P., Sommer, J. E., Heuser, A., Speelmanns, I. M., Blanchard, H. (2014) Redox controls on tungsten and uranium crystal/silicate melt partitioning and implications for the U/W and Th/W ratio of the lunar mantle. *Earth and Planetary Science Letters* **404,** 1–13.

Garbe-Schönberg C-D (1993) Simultaneous determination of 37 trace elements in 28 international rock standards by ICP-MS. *Geostandards Newsletter* **17**, 81-93

Gounelle, M., Meynet, G. (2012) Solar system genealogy revealed by extinct short-lived radionuclides in meteorites. *Astronomy & Astrophysics* **545,** A4.

Gounelle, M., Shu, F. H., Shang, H., Glassgold, A. E., Rehm, K. E., Lee, T. (2001) Extinct Radioactivities and Protosolar Cosmic Rays: Self-Shielding and Light Elements. *The Astrophysical Journal* **548,** 1051–1070.

Gramlich, J. W., Murphy, T. J., Garner, E.L., Shields, W. R. (1973) *Journal of Research National Bureau of Standards, Section A*, **77A**, 691.

Green, T., Pearson, N. (1987) An experimental study of Nb and Ta partitioning between Ti-rich minerals and silicate liquids at high pressure and temperature. *Geochimica et Cosmochimica Acta* **51,** 55–62.

Grossman, L. (1972) Condensation in the primitive solar nebula. *Geochimica et Cosmochimica Acta* **36,** 597–619.

Grossman, L., Ebel, D. S., Simon, S. B. (2002) Formation of refractory inclusions by evaporation of condensate precursors. *Geochimica et Cosmochimica Acta* **66,** 145–161.

Griffith, W. P., Morris, P. J. T. (2003) Charles Hatchett FRS (1765-1847), chemist and discoverer of niobium. *Notes and Records of the Royal Society* **57,** 299–316.

Guthöhrlein, G. H., Helmrich, G., Windholz, L. (1994) Isotope shift in the tantalum atomic spectrum. *Physical Review A* **49,** 120–127.

Hayakawa, T., Mohr, P., Kajino, T., Chiba, S., Mathews, G. J. (2010) Reanalysis of the (J=5) state at 592 keV in 180Ta and its role in the ν-process nucleosynthesis of 180Ta in supernovae. *Physical Review C* **82**, 058801.

Heger, A., Kolbe, E., Haxton, W., Langanke, K., Martínez-Pinedo, G., Woosley, S. (2005) Neutrino nucleosynthesis. *Physics Letters B* **606,** 258–264.

Herwig, F. (2005) Evolution of Asymptotic Giant Branch Stars. *Annual Review of Astronomy and Astrophysics* **43,** 435–479.

Hester, J. J., Desch, S. J. 2005: Understanding Our Origins: Star Formation in H II Region Environments. In: *Chondrites and the Protoplanetray Disk*, ASP Conference Series **341** (eds. Krot, A. N., Scott, E. R. D., Reipurth B.) San Francisco: Astronomical Society of the Pacific

Hezel, D. C., Russell, S. S., ROSS, A. J., KEARSLEY, A. T. (2008) Modal abundances of CAIs: Implications for bulk chondrite element abundances and fractionations. *Meteoritics & Planetary Science* **43,** 1879–1894.

Hidaka, H., Ohta, Y., Yoneda, S. (2003) Nucleosynthetic components of the early solar system inferred from Ba isotopic compositions in carbonaceous chondrites. *Earth and Planetary Science Letters* **214,** 455–466.

Holleman, A. F., Wiberg, N. (2007) Lehrbuch der anorganischen Chemie. 102nd ed. De Gruyter. Berlin.

Holst, J. C., Paton, C., Wielandt, D., Bizzarro, M. (2015) Tungsten isotopes in bulk meteorites and their inclusions-Implications for processing of presolar components in the solar protoplanetary disk. *Meteoritics & Planetary Science* **50,** 1643–1660.

Hult, M., Gasparro, J., Marissens, G., Lindahl, P., Wätjen, U., Johnston, P. et al. (2006) Underground search for the decay of Ta180m. *Physical Review C* **74,** 54311.

Huss, G. R., Meshik, A. P., Smith, J. B., Hohenberg, C. (2003) Presolar diamond, silicon carbide, and graphite in carbonaceous chondrites: implications for thermal processing in the solar nebula. *Geochimica et Cosmochimica Acta* **67,** 4823–4848.

Hutcheon, I. D. (1998) 53Mn-53Cr Dating of Fayalite Formation in the CV3 Chondrite Mokoia: Evidence for Asteroidal Alteration. *Science* **282,** 1865–1867.

Ionov, D., Hofmann, A. (1995) Nb-Ta-rich mantle amphiboles and micas: Implications for subduction-related metasomatic trace element fractionations. *Earth and Planetary Science Letters* **131,** 341–356.

Ireland, T. R., Fegley, B. (2000) The Solar System's Earliest Chemistry: Systematics of Refractory Inclusions. *International Geology Review* **42,** 865–894.

Jacobsen, B., Yin, Q.-Z., Moynier, F., Amelin, Y., Krot, A. N., Nagashima, K. et al. (2008) 26Al–26Mg and 207Pb–206Pb systematics of Allende CAIs: Canonical solar initial 26Al/27Al ratio reinstated. *Earth and Planetary Science Letters* **272,** 353–364.

Jochum, K. P., Nohl, U., Herwig, K., Lammel, E., Stoll, B., Hofmann, A. W. (2005) GeoReM: A New Geochemical Database for Reference Materials and Isotopic Standards. *Geostandards and Geoanalytical Research* **29,** 333–338.

Jochum, K., Seufert, H., Spettel, B., Palme, H. (1986) The solar-system abundances of Nb, Ta, and Y, and the relative abundances of refractory lithophile elements in differentiated planetary bodies. *Geochimica et Cosmochimica Acta* **50,** 1173–1183.

Joint Committee for Guides in Metrology (JCGM) (2012) *International vocabulary of metrology – Basic and general concepts and associated terms (VIM),* BIPM.

Joint Committee for Guides in Metrology (JCGM) (2008) *Evaluation of measurement data — Guide to the expressionof uncertainty in measurement*, ISO/BIPM.

Jones A. P. (2004) Dust destruction processes. In: *Astrophysics of Dust.* ASP Conference Series **309** (eds. Witt, A.N., Clayton, G. C., Draine B. T.) San Francisco: Astronomical Society of the Pacific. 347–367.

Kajino, T., Mathews, G. J., Hayakawa, T. (2014) Neutrinos in core-collapse supernovae and nucleosynthesis. *Journal of Physics G: Nuclear and Particle Physics* **41,** 44007.

Käppeler, F., Arlandini, C., Heil, M., Voss, F., Wisshak, K., Reifarth, R. et al. (2004) Stellar neutron capture on Tam180. II. Defining the s -process contribution to nature's rarest isotope. *Physical Review C* **69,** 055802.

Keil, K. (1968) Mineralogical and chemical relationships among enstatite chondrites. *Journal of Geophysical Research* **73,** 6945–6976.

Kennedy, A. K., Beckett, J. R., Edwards, D. A., Hutcheon, I. D. (1997) Trace element disequilibria and magnesium isotope heterogeneity in 3655A: Evidence for a complex multi-stage evolution of a typical Allende Type B1 CAI. *Geochimica et Cosmochimica Acta* **61,** 1541–1561.

Kimura, J.-i., Chang, Q., Kanazawa, N., Sasaki, S., Vaglarov, B. S. (2016) High-precision in situ analysis of Pb isotopes in glasses using 10 13 Ω resistor high gain amplifiers with ultraviolet femtosecond laser ablation multiple Faraday collector inductively coupled plasma mass spectrometry. *Journal of Analytical Atomic Spectrometry* **31**, 790–800.

Klaver, M., Smeets, R. J., Koornneef, J. M., Davies, G. R., Vroon, P. Z. (2016) Pb isotope analysis of ng size samples by TIMS equipped with a 10 13 Ω resistor using a 207 Pb– 204 Pb double spike. *Journal of Analytical Atomic Spectrometry* **31,** 171–178.

Kleine, T., Mezger, K., Münker, C., Palme, H., Bischoff, A. (2004) 182Hf-182W isotope systematics of chondrites, eucrites, and martian meteorites: Chronology of core formation and early mantle differentiation in Vesta and Mars. *Geochimica et Cosmochimica Acta* **68,** 2935–2946.

Kleine, T., Touboul, M., Bourdon, B., Nimmo, F., Mezger, K., Palme, H. et al. (2009) Hf–W chronology of the accretion and early evolution of asteroids and terrestrial planets. *Geochimica et Cosmochimica Acta* **73,** 5150–5188.

König, S., Münker, C., Hohl, S., Paulick, H., Barth, A., Lagos, M. et al. (2011) The Earth's tungsten budget during mantle melting and crust formation. *Geochimica et Cosmochimica Acta* **75,** 2119–2136.

König, S., Münker, C., Schuth, S., Garbe-Schönberg, D. (2008) Mobility of tungsten in subduction zones. *Earth and Planetary Science Letters* **274,** 82–92.

Kööp, L., Davis, A. M., Nakashima, D., Park, C., Krot, A. N., Nagashima, K. et al. (2016) A link between oxygen, calcium and titanium isotopes in 26Al-poor hibonite-rich CAIs from Murchison and implications for the heterogeneity of dust reservoirs in the solar nebula. *Geochimica et Cosmochimica Acta* **189,** 70–95.

Koornneef, J. M., Bouman, C., Schwieters, J. B., Davies, G. R. (2013) Use of 1012 ohm current amplifiers in Sr and Nd isotope analyses by TIMS for application to sub-nanogram samples. *Journal of Analytical Atomic Spectrometry* **28,** 749.

Koornneef, J. M., Nikogosian, I., van Bergen, M. J., Smeets, R., Bouman, C., Davies, G. R. (2015) TIMS analysis of Sr and Nd isotopes in melt inclusions from Italian potassium-rich lavas using prototype 1013Ω amplifiers. *Chemical Geology* **397,** 14–23.

Koornneef, J., Bouman, C., Schwieters, J., Davies, G. (2014) Measurement of small ion beams by thermal ionisation mass spectrometry using new 1013Ohm resistors. *Analytica Chimica Acta* **819,** 49–55.

Kornacki, A. S., Fegley, B. (1986) The abundance and relative volatility of refractory trace elements in Allende Ca,Al-rich inclusions: implications for chemical and physical processes in the solar nebula. *Earth and Planetary Science Letters* **79,** 217–234.

Kröner, A., Hoffmann, J. E., Xie, H., Münker, C., Hegner, E., Wan, Y. et al. (2014) Generation of early Archaean grey gneisses through melting of older crust in the eastern Kaapvaal craton, southern Africa. *Precambrian Research* **255,** 823–846.

Krot, A. N., PETAEV, M. I., Zolensky, M. E., Keil, K., Scott, E. R. D., NAKAMURA, K. (1998) Secondary calcium-iron-rich minerals in the Bali-like and Allende-like oxidized CV3 chondrites and Allende dark inclusions. *Meteoritics & Planetary Science* **33,** 623–645.

Krot, A. N., Scott, E. R. D., Zolensky, M. E. (1995) Mineralogical and chemical modification of components in CV3 chondrites: Nebular or asteroidal processing? *Meteoritics* **30,** 748–775.

Kruijer, T. S., Kleine, T., Fischer-Gödde, M., Burkhardt, C., Wieler, R. (2014) Nucleosynthetic W isotope anomalies and the Hf–W chronometry of Ca–Al-rich inclusions. *Earth and Planetary Science Letters* **403,** 317–327.

Kuhlmann, L. (2011) Isotopen- und Spurenelementanalysen an mafischen Vulkangesteinen aus La Palma und Teneriffa. Bachelor thesis. University of Cologne.

Lagos, M., Scherer, E. E., Tomaschek, F., Münker, C., Keiter, M., Berndt, J., Ballhaus, C. (2007) High precision Lu–Hf geochronology of Eocene eclogite-facies rocks from Syros, Cyclades, Greece. *Chemical Geology* **243,** 16–35.

de Laeter, J. R., Bukilic, N. (2005) Isotope abundance of Ta180m and p-process nucleosynthesis. *Physical Review C* **72,** 25801.

de Laeter, J. R., Bukilic, N. (2006) The isotopic composition and atomic weight of ytterbium. *International Journal of Mass Spectrometry* **252,** 222–227.

Lee, T., Shu, F. H., Shang, H., Glassgold, A. E., Rehm, K. E. (1998) Protostellar Cosmic Rays and Extinct Radioactivities in Meteorites. *The Astrophysical Journal* **506,** 898–912.

Leya, I., Wieler, R., Halliday, A. N. (2003) The influence of cosmic-ray production on extinct nuclide systems. *Geochimica et Cosmochimica Acta* **67,** 529–541.

Linnen, R. L., van Lichtervelde, M., Černy, P. (2012) Granitic Pegmatites as Sources of Strategic Metals. *Elements* **8,** 275–280.

Liu, J., Pearson, D. G. (2014) Rapid, precise and accurate Os isotope ratio measurements of nanogram to sub-nanogram amounts using multiple Faraday collectors and amplifiers equipped with 1012 Ω resistors by N-TIMS. *Chemical Geology* **363,** 301–311.

Lodders, K. (2003) Solar System Abundances and Condensation Temperatures of the Elements. *The Astrophysical Journal* **591,** 1220–1247.

Longerich, H., Fryer, B., Strong, D. (1987) Determination of lead isotope ratios by inductively coupled plasma-mass spectrometry (ICP-MS). Spectrochimica Acta Part B: Atomic Spectroscopy **42**, 39–48.

Ludwig, K.R. (2003) Isoplot 3.00: a Geochronologica lToolkit for Microsoft Excel. Berkeley Geochronology Center Special Publication **4**, 70.

Luo, X., Rehkämper, M., Lee, D.-C., Halliday, A. N. (1997) High precision 230Th/232Th and 234U/238U measurements using energyfiltered ICP magnetic sector multiple collector mass spectrometry. *International Journal of Mass Spectrometry and Ion Processes* **171,** 105–117.

Maréchal, C. N., Télouk, P., Albarède, F. (1999) Precise analysis of copper and zinc isotopic compositions by plasma-source mass spectrometry. Chemical Geology **156**, 251–273.

Martin, P. M., Mason, B. (1974) Major and trace elements in the Allende meteorite. *Nature* **249,** 333–334.

Mason, B., Taylor, S. R. (1982) Inclusions in the Allende Meteorite. *Smithsonian Contributions to the Earth Sciences* **25,** 1–30.

Mayanovic, R. A., Yan, H., Anderson, A. J., Solferino, G. (2013) Investigation of the structural environment of Ta in a silicate glass and water system under high P–T conditions. *Journal of Non-Crystalline Solids* **368,** 71–78.

McCulloch, M., Gamble, J. (1991) Geochemical and geodynamical constraints on subduction zone magmatism. *Earth and Planetary Science Letters* **102,** 358–374.

McCulloch, M. T., Wasserburg, G. J. (1978a) Barium and neodymium isotopic anomalies in the Allende meteorite. *The Astrophysical Journal* **220,** L15-L19.

McCulloch, M. T., Wasserburg, G. J. (1978b) More anomalies from the Allende Meteorite: Samarium. *Geophysical Research Letters* **5,** 599–602.

McKeegan, K. D. (2000) Incorporation of Short-Lived 10Be in a Calcium-Aluminum-Rich Inclusion from the Allende Meteorite. *Science* **289,** 1334–1337.

Meija, J., Coplen, T. B., Berglund, M., Brand, W. A., Bièvre, P. de, Gröning, M. et al. (2016) Isotopic compositions of the elements 2013 (IUPAC Technical Report). Pure and Applied Chemistry **88**, 293-206.

Meyer, B. S. (1994) The r-, s-, and p-Processes in Nucleosynthesis. *Annual Review of Astronomy and Astrophysics* **32,** 153–190.

Miller, C. A., Peucker-Ehrenbrink, B., Schauble, E. A. (2015) Theoretical modeling of rhenium isotope fractionation, natural variations across a black shale weathering profile, and potential as a paleoredox proxy. *Earth and Planetary Science Letters* **430,** 339–348.

Möller, H. (2002) Magma genesis and mantle sources at the Mid-Atlantic Ridge East of Ascension Island. Dissertation. Kiel. http://eldiss.uni-kiel.de/macau/receive/dissertation_diss_597, visited 11.2014.

Mohr, P., Käppeler, F., Gallino, R. (2007) Survival of nature's rarest isotope Ta180 under stellar conditions. *Physical Review C* **75,** 012802(R).

Moynier, F., Bouvier, A., Blichert-Toft, J., Telouk, P., Gasperini, D., Albarède, F. (2006) Europium isotopic variations in Allende CAIs and the nature of mass-dependent fractionation in the solar nebula. *Geochimica et Cosmochimica Acta* **70,** 4287–4294.

Moynier, F., Pringle, E. A., Bouvier, A., Moureau, J. (2015) Barium stable isotope composition of the Earth, meteorites, and calcium–aluminum-rich inclusions. *Chemical Geology* **413,** 1–6.

Mughabghab, S. F. (2003) Thermal neutron capture cross sections, resonance integrals, and g-factors. INDC(NDS)-440. Vienna.

Münker, C., Pfänder, J. A., Weyer, S., Buchl, A., Kleine, T., Mezger, K. (2003) Evolution of Planetary Cores and the Earth-Moon System from Nb/Ta Systematics. *Science* **301,** 84–87.

Münker, C., Weyer, S., Scherer, E., Mezger, K. (2001) Separation of high field strength elements (Nb, Ta, Zr, Hf) and Lu from rock samples for MC-ICPMS measurements. *Geochemistry, Geophysics, Geosystems* **2,** 2001GC000183.

Naumenko, M. O., Mezger, K., Nägler, T. F., Villa, I. M. (2013) High precision determination of the terrestrial 40K abundance. *Geochimica et Cosmochimica Acta* **122,** 353–362.

Newman, K. (2012) Effects of the sampling interface in MC-ICP-MS: Relative elemental sensitivities and non-linear mass dependent fractionation of Nd isotopes. Journal of Analytical Atomic Spectrometry **27**, 63.

Niederer, F. R., Papanastassiou, D. (1984) Ca isotopes in refractory inclusions. *Geochimica et Cosmochimica Acta* **48,** 1279–1293.

Niederer, F., Papanastassiou, D., Wasserburg, G. (1985) Absolute isotopic abundances of Ti in meteorites. *Geochimica et Cosmochimica Acta* **49,** 835–851.

Nielsen, S. G., Prytulak, J., Wood, B. J., Halliday, A. N. (2014) Vanadium isotopic difference between the silicate Earth and meteorites. *Earth and Planetary Science Letters* **389,** 167–175.

Niemeyer, S., Lugmair, G. (1984) Titanium isotopic anomalies in meteorites. *Geochimica et Cosmochimica Acta* **48,** 1401–1416.

Palme, H., Lodders, K., Jones, A. (2014) Solar System Abundances of the Elements. In : *Treatise on Geochemistry (Second Edition): Volume 1*. Elsevier. Amsterdam. 15–36.

Palme, H., O'Neill, H. (2014) Cosmochemical Estimates of Mantle Composition. In : *Treatise on Geochemistry (Second Edition): Volume 2*. Elsevier. Amsterdam. 1–39.

Patchett, P. J. (1980) Sr isotopic fractionation in Ca–Al inclusions from the Allende meteorite. *Nature* **283,** 438–441.

Patchett, P. J., Tatsumoto, M. (1981) A routine high-precision method for Lu-Hf isotope geochemistry and chronology. *Contributions to Mineralogy and Petrology* **75,** 263–267.

Pearce, J. A., Peate, D. W. (1995) Tectonic Implications of the Composition of Volcanic ARC Magmas. *Annual Review of Earth and Planetary Sciences* **23,** 251–285.

Peters, S. T., Münker, C., Becker, H., Schulz, T. (2014) Alpha-decay of 184Os revealed by radiogenic 180W in meteorites: Half life determination and viability as geochronometer. *Earth and Planetary Science Letters* **391,** 69–76.

Peters, S. T., Münker, C., Wombacher, F., Elfers, B.-M. (2015) Precise determination of low abundance isotopes (^{174}Hf, ^{180}W and ^{190}Pt) in terrestrial materials and meteorites using multiple collector ICP-MS equipped with $10^{12}\Omega$ Faraday amplifiers. *Chemical Geology* **413,** 132–145.

Peters, S. T. M., Münker, C., Pfeifer, M., Elfers, B.-M., Sprung, P. (2016) Distribution of p-process ^{174}Hf in early solar system materials and the origin of nucleosynthetic Hf and W isotope anomalies in Ca–Al rich inclusions. *Earth and Planetary Science Letters*. http://dx.doi.org/10.1016/j.epsl.2016.11.009

Pfeifer, M., Lloyd, N. S., Peters, S. T. M., Wombacher, F., Elfers, B.-M., Schulz, T., Münker, C. (2016) Tantalum isotope ratio measurements and isotope abundances determined by MC-ICP-MS using amplifiers equipped with 10^{10}, 10^{12} and 10^{13} Ohm resistors. *Journal of Analytical Atomic* Spectrometry **32**, 130-143.

Pritzkow, W., Wunderli, S., Vogl, J., Fortunato, G. (2007) The isotope abundances and the atomic weight of cadmium by a metrological approach. *International Journal of Mass Spectrometry* **261,** 74–85.

Ranen, M. C., Jacobsen, S. B. (2006) Barium Isotopes in Chondritic Meteorites: Implications for Planetary Reservoir Models. *Science* **314,** 809–812.

Rauscher, T., Dauphas, N., Dillmann, I., Fröhlich, C., Fülöp, Z., Gyürky, G. (2013) Constraining the astrophysical origin of the p-nuclei through nuclear physics and meteoritic data. *Reports on Progress in Physics* **76,** 66201.

Rayet, M., Arnould, M., Hashimoto, M., Prantzos, N., Nomoto, K. (1995) The p-process in Type II supernovae. *Astronomy and Astrophysics* **298,** 517–527.

Rehkämper, M., Frank, M., Hein, J., Porcelli, D., Halliday, A. N., Ingri, J., Liebetrau, V. (2002) Thallium isotope variations in seawater and hydrogenetic, diagenetic, and hydrothermal ferromanganese deposits. *Earth and Planetary Science Letters* **197,** 65–81.

Richter, S., Eykens, R., Kühn, H., Aregbe, Y., Verbruggen, A., Weyer, S. (2010) New average values for the n(238U)/n(235U) isotope ratios of natural uranium standards. *International Journal of Mass Spectrometry* **295,** 94–97.

Rose, H. (1844) Ueber die Zusammensetzung der Tantalite und ein im Tantalite von Baiern enthaltenes neues Metall. *Annalen der Physik.* **139**, 317–341.

Rotaru, M., Birck, J. L., Allègre, C. J. (1992) Clues to early Solar System history from chromium isotopes in carbonaceous chondrites. *Nature* **358,** 465–470.

Rubin, A. E., Fegley B., Brett J. R. (1988) Oxidation state in chondrites. In: *Meteorites and the Early Solar System* (eds. Kerridge, J. F., Matthews M. S.) University of Arizona Press. Tucson, Arizona. 488-511.

Rudnick, R., Gao, S. (2014) Composition of the Continental Crust. In : *Treatise on Geochemistry (Second Edition): Volume 4*. Elsevier. Amsterdam. 1–51.

Russell, W., Papanastassiou, D., Tombrello, T. (1978) Ca isotope fractionation on the Earth and other solar system materials. *Geochimica et Cosmochimica Acta* **42,** 1075–1090.

Sarkar, C., Pearson, D., Heaman, L. M., Woodland, S. (2015) Precise Pb isotope ratio determination of picogram-size samples: A comparison between multiple Faraday collectors equipped with 1012Ω amplifiers and multiple ion counters. *Chemical Geology* **395,** 27–40.

Schauble, E. A. (2007) Role of nuclear volume in driving equilibrium stable isotope fractionation of mercury, thallium, and other very heavy elements. *Geochimica et Cosmochimica Acta* **71,** 2170–2189.

Scherer, E. E., Münker, C., Mezger, K. (2001) Calibration of the Lutetium-Hafnium Clock. *Science* **293,** 683–687.

Schiller, M., Paton, C., Bizzarro, M. (2012) Calcium isotope measurement by combined HR-MC-ICPMS and TIMS. *Journal of Analytical Atomic Spectrometry* **27,** 38.

Schmidt, K., Bau, M., Hein, J. R., Koschinsky, A. (2014) Fractionation of the geochemical twins Zr–Hf and Nb–Ta during scavenging from seawater by hydrogenetic ferromanganese crusts. *Geochimica et Cosmochimica Acta* **140,** 468–487.

Schönbächler, M., Lee, D.-C., Rehkämper, M., Halliday, A. N., Fehr, M. A., Hattendorf, B., Günther, D. (2003) Zirconium isotope evidence for incomplete admixing of r-process components in the solar nebula. *Earth and Planetary Science Letters* **216,** 467–481.

Schulz, T., Münker, C., Peters, S. T. (2013) p-Process 180W anomalies in iron meteorites: Nucleosynthetic versus non-nucleosynthetic origins. *Earth and Planetary Science Letters* **362,** 246–257.

Shahid, M., Kim, K., Naik, H., Kim, G. (2014) Measurement of cross-sections for produced radionuclide in proton induced reactions on natHf up to 45MeV. *Nuclear Instruments and Methods in Physics Research Section B: Beam Interactions with Materials and Atoms* **322,** 13–22.

Shannon, R. D. (1976) Revised effective ionic radii and systematic studies of interatomic distances in halides and chalcogenides. *Acta Crystallographica Section A* **32,** 751–767.

Shen, J. J.-S., Lee, T. (2003) 138 La Anomaly in the Early Solar System. *The Astrophysical Journal* **596,** L109.

Shu, F. H. (1997) X-rays and Fluctuating X-Winds from Protostars. *Science* **277,** 1475–1479.

Siegel, K., Wagner, T., Trumbull, R. B., Jonsson, E., Matalin, G., Wälle, M., Heinrich, C. A., (2016) Stable isotope (B, H, O) and mineral-chemistry constraints on the magmatic to hydrothermal evolution of the Varuträsk rare-element pegmatite (Northern Sweden). *Chemical Geology* **421**, 1-16.

Simon, J. I., Young, E. D., Russell, S. S., Tonui, E. K., Dyl, K. A., Manning, C. E. (2005) A short timescale for changing oxygen fugacity in the solar nebula revealed by high-resolution 26Al–26Mg dating of CAI rims. *Earth and Planetary Science Letters* **238,** 272–283.

Sneden, C., Cowan, J. J., Gallino, R. (2008) Neutron-Capture Elements in the Early Galaxy. Annual Review of Astronomy and Astrophysics **46**, 241–288.

Soderlund, U., Patchett, P. J., Vervoort, J. D., Isachsen, C. E., (2004) The ^{176}Lu decay constant determined by Lu–Hf and U–Pb isotope systematics of Precambrian mafic intrusions. *Earth and Planetary Science Letters* **219,** 311–324.

Soloviev, V. (1998) Vibrational states on the isomers in deformed nuclei. *Nuclear Physics A* **633,** 247–265.

Sossi, P. A., Moynier, F., Chaussidon, M., Gounelle, M., Villeneuve, J., Kato, C. (2016) Correlated 50V and 10Be excesses of irradiation origin in refractory inclusions from carbonaceous condrites. *79th Annual Meeting of the Meteoritical Society*. Abstract 6383.

Sprung, P., Scherer, E. E., Upadhyay, D., Leya, I., Mezger, K. (2010) Non-nucleosynthetic heterogeneity in non-radiogenic stable Hf isotopes: Implications for early solar system chronology. *Earth and Planetary Science Letters* **295,** 1–11.

Stracke, A., Palme, H., Gellissen, M., Münker, C., Kleine, T., Birbaum, K. et al. (2012) Refractory element fractionation in the Allende meteorite: Implications for solar nebula condensation and the chondritic composition of planetary bodies. *Geochimica et Cosmochimica Acta* **85,** 114–141.

Stracke, A., Scherer, E., Reynolds, B. (2014) Application of Isotope Dilution in Geochemistry. In : *Treatise on Geochemistry (Second Edition): Volume 15*. Elsevier. Amsterdam. 71–86.

Suzuki, K., Miyata, Y., Kanazawa, N. (2004) The isotopic composition of Rhenium. *International Journal of Mass Spectrometry* **235**, 97.

Takács, S., Tárkányi, F., Hermanne, A., Adam Rebeles, R. (2011) Activation cross sections of proton induced nuclear reactions on natural hafnium. *Nuclear Instruments and Methods in Physics Research Section B: Beam Interactions with Materials and Atoms* **269,** 2824–2834.

Tanaka, R., Makishima, A., Kitagawa, H., Nakamura, E. (2003) Suppression of Zr, Nb, Hf and Ta coprecipitation in fluoride compounds for determination in Ca-rich materials. *Journal of Analytical Atomic Spectrometry* **18,** 1458.

Thermo Fisher Scientific (2010) Neptune Plus Hardware Manual - Revision C. Edited by Thermo Fisher Scientific. Bremen.

Thielemann, F.-K., Arcones, A., Käppeli, R., Liebendörfer, M., Rauscher, T., Winteler, C. et al. (2011) What are the astrophysical sites for the r-process and the production of heavy elements? *Progress in Particle and Nuclear Physics* **66,** 346–353.

Thirlwall, M. (2001) Inappropriate tail corrections can cause large inaccuracy in isotope ratio determination by MC-ICP-MS. *Journal of Analytical Atomic Spectrometry* **16,** 1121–1125.

Thirlwall, M., Anczkiewicz, R. (2004) Multidynamic isotope ratio analysis using MC–ICP–MS and the causes of secular drift in Hf, Nd and Pb isotope ratios. *International Journal of Mass Spectrometry* **235,** 59–81.

Tiepolo, M., Vannucci, R., Oberti, R., Foley, S., Bottazzi, P., Zanetti, A. (2000) Nb and Ta incorporation and fractionation in titanian pargasite and kaersutite: crystal–chemical constraints and implications for natural systems. *Earth and Planetary Science Letters* **176,** 185–201.

Tissot, F. L. H., Dauphas, N., Grossman, L. (2016) Origin of uranium isotope variations in early solar nebula condensates. *Science Advances* **2,** e1501400.

Touboul, M., Puchtel, I. S., Walker, R. J. (2015) Tungsten isotopic evidence for disproportional late accretion to the Earth and Moon. *Nature* **520,** 530–533.

Travaglio, C., Röpke, F. K., Gallino, R., Hillebrandt, W. (2011) Type Ia Supernovae as sites of the p-process: Two-dimensional models coupled to nucleosynthesis. *The Astrophysical Journal* **739,** 93.

Trinquier, A., Elliott, T., Ulfbeck, D., Coath, C., Krot, A. N., Bizzarro, M. (2009) Origin of Nucleosynthetic Isotope Heterogeneity in the Solar Protoplanetary Disk. *Science* **324,** 374–376.

Tsujimoto, T., Shigeyama, T. (2014) Enrichment history of r-process elements shaped by a merger of neutron star pairs. *Astronomy & Astrophysics* **565,** L5.

Urey, H. C. (1947) The thermodynamic properties of isotopic substances. *Journal of the Chemical Society (Resumed)***,** 562.

Vockenhuber, C., Dillmann, I., Heil, M., Käppeler, F., Winckler, N., Kutschera, W. et al. (2007) Stellar (n,γ) cross sections of Hf174 and radioactive Hf182. *Physical Review C* **75,** 015804.

Wakaki, S., Itoh, S., Tanaka, T., Yurimoto, H. (2013) Petrology, trace element abundances and oxygen isotopic compositions of a compound CAI–chondrule object from Allende. *Geochimica et Cosmochimica Acta* **102,** 261–279.

Wallerstein, G., Iben, I., Parker, P., Boesgaard, A., Hale, G., Champagne, A. et al. (1997) Synthesis of the elements in stars: forty years of progress. *Reviews of Modern Physics* **69,** 995–1084.

Wang, J., Ren, T., Lu, H., Zhou, T., Zhou, Y. (2015) The absolute isotopic composition and atomic weight of ytterbium using multi-collector inductively coupled plasma mass spectrometry and development of an SI-traceable ytterbium isotopic certified reference material. *Journal of Analytical Atomic Spectrometry* **30,** 1377–1385.

Wang, M., Audi, G., Wapstra, A., Kondev, F., MacCormick, M., Xu, X., Pfeiffer, B. (2012) The Ame2012 atomic mass evaluation. *Chinese Physics C* **36,** 1603–2014.

Warren, P. H. (2011) Stable-isotopic anomalies and the accretionary assemblage of the Earth and Mars: A subordinate role for carbonaceous chondrites. *Earth and Planetary Science Letters* **311,** 93–100.

Wasserburg, G. J., Busso, M., Gallino, R. (1996) Abundances of Actinides and Short-lived Nonactinides in the Interstellar Medium: Diverse Supernova Sources for the r-Processes. *The Astrophysical Journal* **466,** L109.

Weyer, S., Anbar, A., Gerdes, A., Gordon, G., Algeo, T., Boyle, E. (2008) Natural fractionation of 238U/235U. *Geochimica et Cosmochimica Acta* **72,** 345–359.

Weyer, S., Münker, C., Mezger, K. (2003) Nb/Ta, Zr/Hf and REE in the depleted mantle: implications for the differentiation history of the crust–mantle system. *Earth and Planetary Science Letters* **205,** 309–324.

Weyer, S., Münker, C., Rehkämper, M., Mezger, K. (2002) Determination of ultra-low Nb, Ta, Zr and Hf concentrations and the chondritic Zr/Hf and Nb/Ta ratios by isotope dilution analyses with multiple collector ICP-MS. *Chemical Geology* **187,** 295–313.

Wielandt, D., Bizzarro, M. (2011) A TIMS-based method for the high precision measurements of the three-isotope potassium composition of small samples. *Journal of Analytical Atomic Spectrometry* **26,** 366.

Wieser, M. E., Schwieters, J. B. (2005) The development of multiple collector mass spectrometry for isotope ratio measurements. *International Journal of Mass Spectrometry* **242,** 97–115.

Wimpenny, J. B., Amelin, Y., Yin, Q.-Z. (2013) Precise Determination of the Lutetium Isotopic Composition in Rocks and Minerals Using Multicollector ICPMS. *Analytical Chemistry* **85,** 11258–11264.

Wisshak, K., Voss, F., Kaeppeler, F., Kazakov, L., Bečvář, F., Krtička, M., Gallino, R. and Pignatari, M., (2006) Fast neutron capture on the Hf isotopes: Cross sections, isomer production, and stellar aspects. *Physical Review C* **73**, 045807.

White, F. A., Collins, T. L., Rourke, F. M. (1955) New Naturally Occurring Isotope of Tantalum. Physical Review 97, 566–567.

Willbold, M. (2007) Determination of Ce isotopes by TIMS and MC-ICPMS and initiation of a new, homogeneous Ce isotopic reference material. *Journal of Analytical Atomic Spectrometry* **22,** 1364.

Wombacher, F., Rehkämper, M. (2003) Investigation of the mass discrimination of multiple collector ICP-MS using neodymium isotopes and the generalised power law. *Journal of Analytical Atomic Spectrometry* **18,** 1371.

Woosley, S. E., Hartmann, D. H., Hoffman, R. D., Haxton, W. C. (1990) The nu-process. *The Astrophysical Journal* **356,** 272.

Woosley, S. E., Heger, A., Weaver, T. A. (2002) The evolution and explosion of massive stars. *Reviews of Modern Physics* **74,** 1015–1071.

Woosley, S. E., Weaver, T. A. (1995) The Evolution and Explosion of Massive Stars. II. Explosive Hydrodynamics and Nucleosynthesis. *The Astrophysical Journal Supplement Series* **101,** 181.

Yin, Q., Jacobsen, S. B., Yamashita, K. (2002) Diverse supernova sources of pre-solar material inferred from molybdenum isotopes in meteorites. *Nature* **415,** 881–883.

Yokoi, K., Takahashi, K. (1983) Slow neutron capture origin for 180Tam. *Nature* **305,** 198–200.

Zhang, J., Huang, S., Davis, A. M., Dauphas, N., Hashimoto, A., Jacobsen, S. B. (2014) Calcium and titanium isotopic fractionations during evaporation. *Geochimica et Cosmochimica Acta* **140,** 365–380.

6 Danksagung

Zuallererst möchte ich meinem Betreuer Carsten Münker danken. Danke, dass Du mir die Möglichkeit gegeben hast bei Dir promovieren zu dürfen. Ich hatte für die Promotion zuvorderst nach einem Projekt in der Kosmochemie und Massenspektrometrie gesucht. Dass ich mich dann im Wissenschaftlichen, wie auch im Sozialen perfekt in Köln und Bonn aufgehoben fühle, liegt zu einem großen Teil an Dir. Danke für Dein Vertrauen (auch zukünftig).

Ein besonderer Dank geht zudem an Frank Wombacher, unserem unermüdlichen Laborleiter. Gerade bei einem analytisch anspruchsvollen Projekt, wie dem meinen, war der Austausch mit Dir unerlässlich zum Gelingen. Selbst wenn Du nie Zeit hattest, konnten sich zwischen Tür und Angel immer ausgedehnte Fachdiskussionen entwickeln. Ich habe eine Menge von dir über Massenspektrometrie gelernt und habe einen großen Spaß daran entwickelt, die Grenzen der Geräte immer weiter auszutesten.

Many thanks go to Stefan for his introduction into the topic and the Schloss. You paved the way for Bo and me with your great previous work. We just had to walk it. Apart from science, there was always time for a Genever. Bedankt!

Allgemein möchte ich der Arbeitsgruppe in Köln/ Bonn danken. Das freundliche Miteinander im, neben und nach dem Labor ist eine unserer Stärken. Neben den bereits genannten, war vor allem Hilfe und Austausch von und mit Dominik, Peter, Elis und Maria immer willkommen. Von dem Zusammenhalt unter uns Doktoranden, Claudia, Kathrin, Christiane, Vicky, Ninja, Julia, Christian, dem Laborkater Jonas, Sebastian, Max und Alessandro, haben wir alle profitiert. Max, thanks for your help with editing parts of the thesis and for feeding me.

Die Zeit in Bonn wäre ohne die Leute im Schloss nicht so befriedigend gewesen. Die Gemeinschaft, die über gemeinsame Arbeit hinausgeht, ist etwas Besonderes und wird sicher kaum an anderen „Arbeitsplätzen“ zu finden sein.

Related to my project, I am thankful to the Thermo Fisher Bremen people, especially Nicholas Lloyd and Claudia Bouman, who gave me the opportunity for repeated measurements. Even if every measurement session had its problems, there had always been a chance to come back.

Als Kosmochemiker ist man immer auf Proben angewiesen, die man zumeist (leider) nicht selbst holen kann. Daher ein Dank an alle Spender (neben Stefan, Carsten, Frank und Peter): Addi Bischof, Erik Strub, Rolf Hollerbach, Elis Hoffmann und Herbert Palme. Zudem ein Dank für die Spurenelementmessungen nach Kiel an Ulrike Westernströer und Dieter Garbe-Schönberg.

Besonders hervorzuheben habe ich noch Bo-Magnus Elfers. Durch unsere gekoppelten Projekte, die zeitglich starteten, waren wir durchgängig auf einem ähnlichen Wissensstand und konnten jederzeit wissenschaftlich diskutieren und an gleichen Proben arbeiten. Durch unser gegenseitiges betreutes Forschen haben wir beide persönlich und wissenschaftlich profitiert. Die Tatsache ein Büro tiefer einen Leidensgenossen zu haben, hat mir immer über Durststrecken hinweg geholfen. Ich freue mich mit Dir in Zukunft weiter zusammen arbeiten zu dürfen. Ein Jägermeister auf Dich!

Zu Guter Letzt hat meine Familie, Mama, Papa und Thorsten, eine Würdigung verdient. Ich hätte mir früher nie vorstellen könne, jemals eine Dissertation zu verfassen. Das verdanke ich vor allem meinen Eltern, die mich in jeder Lebenslage unermüdlich unterstützt haben, und es weiterhin tun. Diesen Doktortitel habt Ihr euch mit verdient.

Appendix A: Backscattered electron images of CAIs

Backscattered electron image of unusual CAI_C-BN_1. The different phases are indicated in the image and can be discerned by their grey scales.

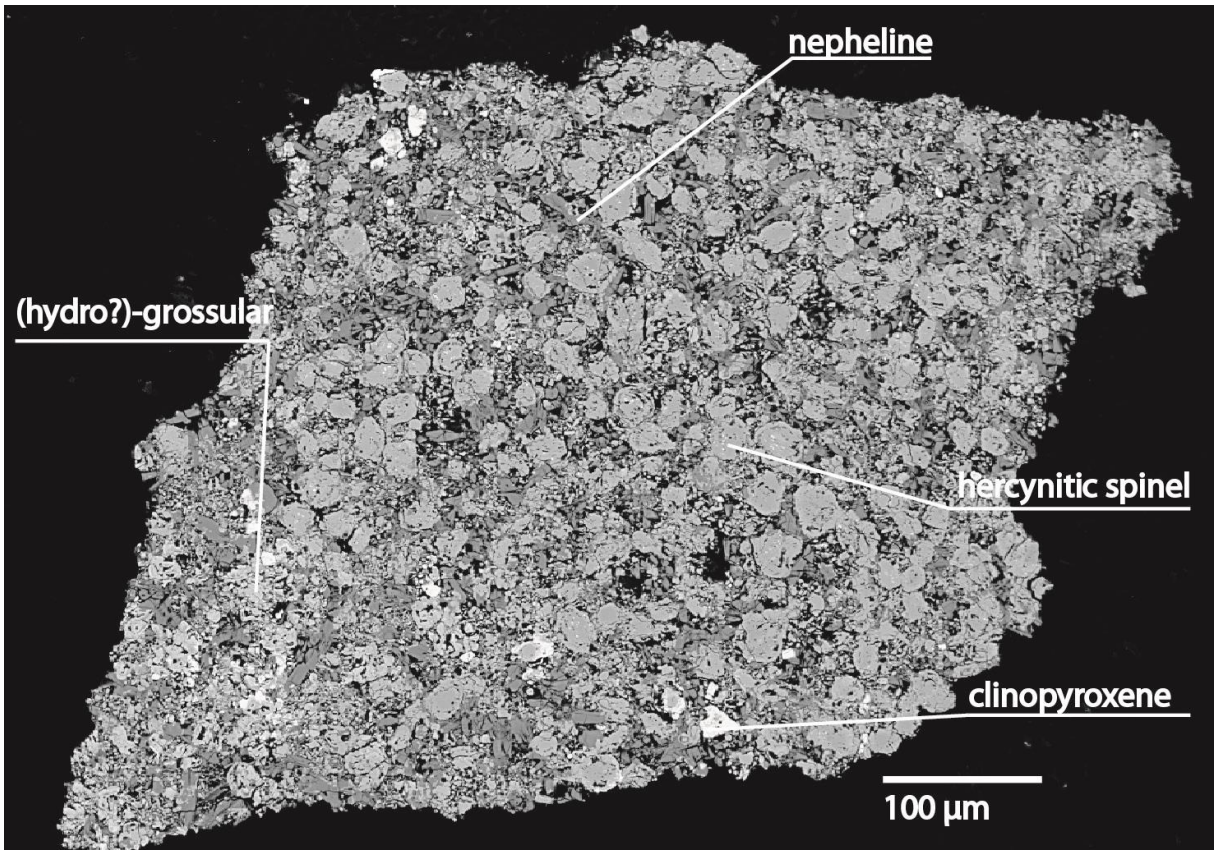

Backscattered electron image of CAI_C-BN_2. The different phases are indicated in the image and can be discerned by their grey scales. Calcic pyroxene indicates fassaite.

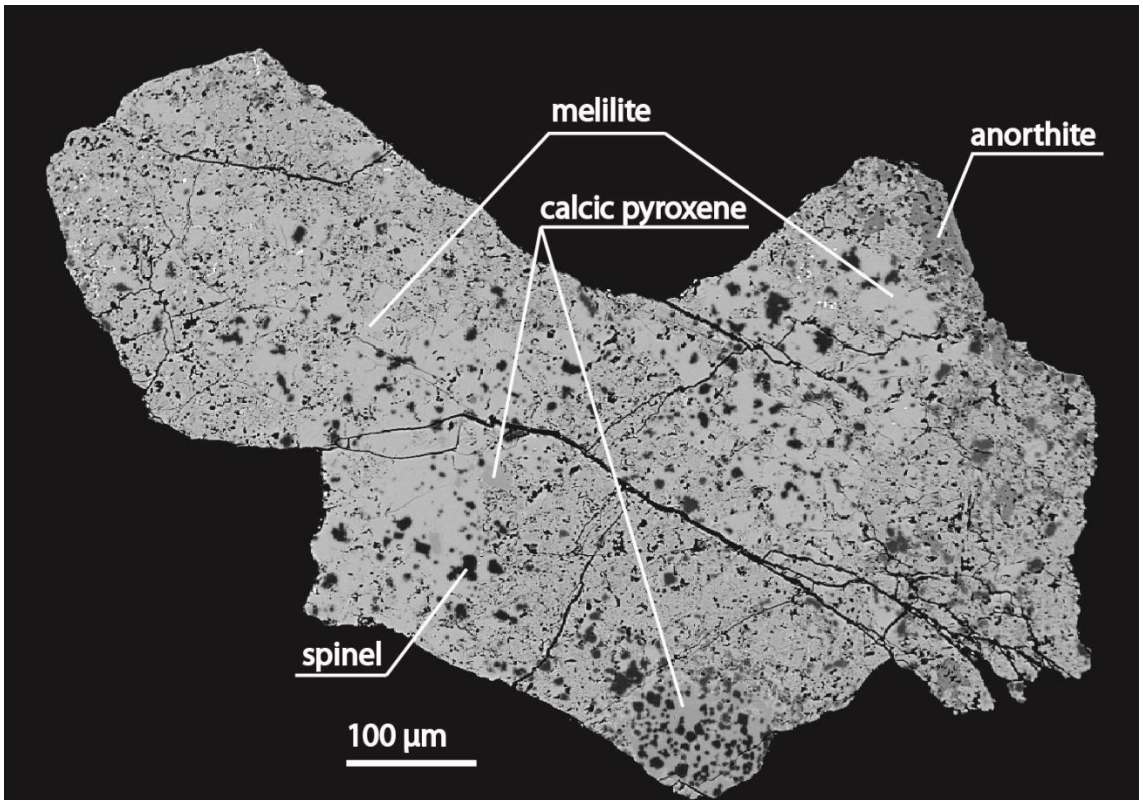

Backscattered electron image of CAI_C-BN_3. The different phases are indicated in the image and can be discerned by their grey scales.

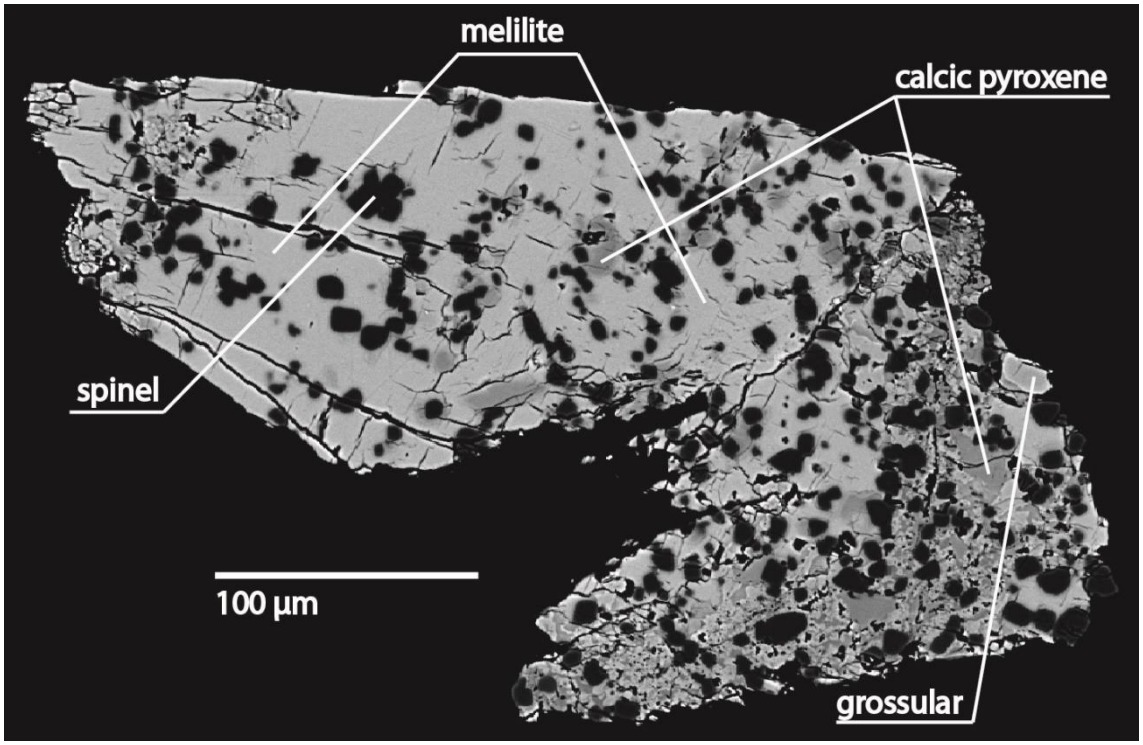

Backscattered electron image of CAI_C-BN_4. The different phases are indicated in the image and can be discerned by their grey scales. Calcic pyroxene indicates fassaite.

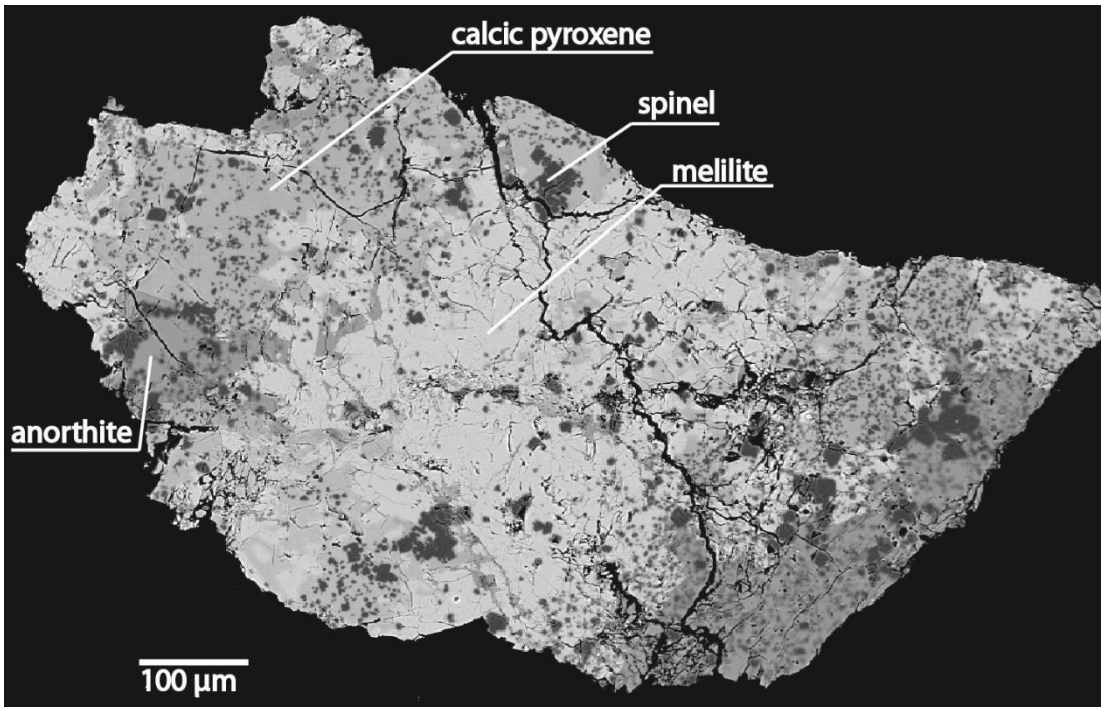

Backscattered electron image of CAI_C-BN_5. The different phases are indicated in the image and can be discerned by their grey scales. Here, the adjacent matrix and the accretionary rim towards the CAI are present. The interior of the CAI is partly altered (anorthite veins).

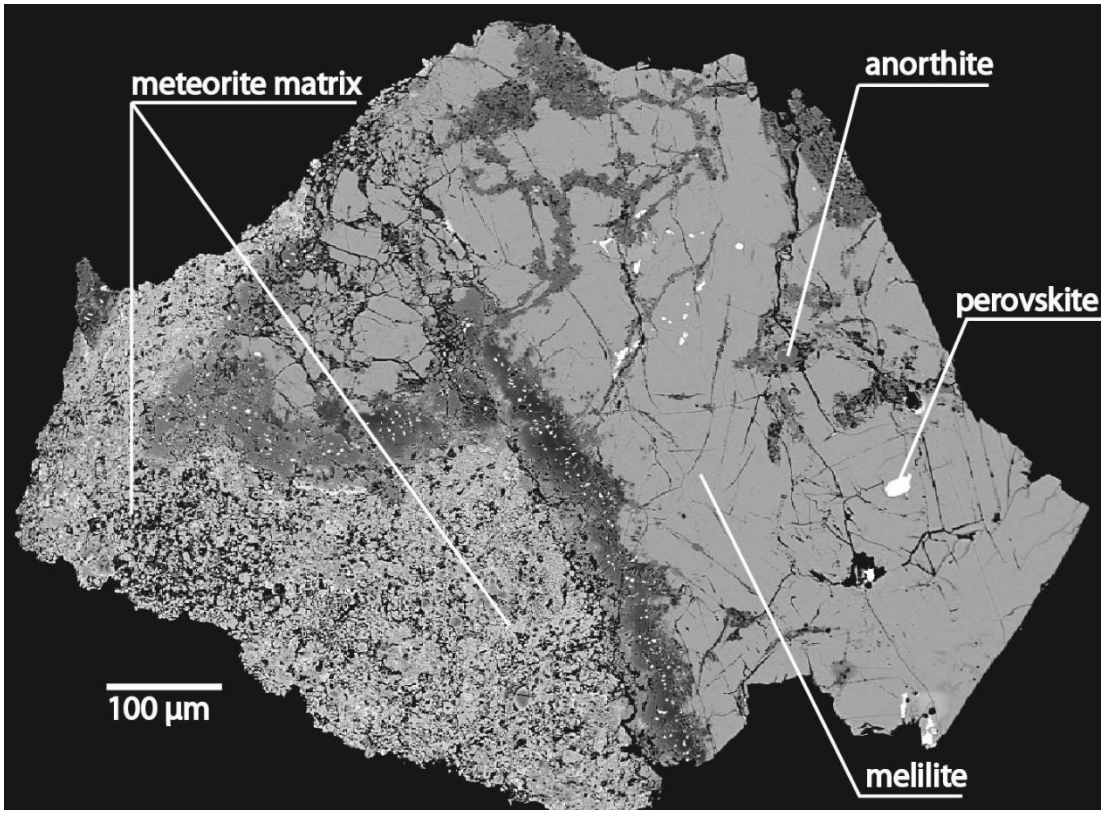

Appendix B: EMP mineral analyses on CAIs

Representative EMP analyses of CAI 1. The comment line gives the name of the individual measurement. Sp indicates spinell, di=diopside.

mineral	**di**	**hercynitic sp**	**hercynitic sp**	**di**
comment	CAI 5_1	CAI 5_6	CAI 5_7	CAI 5_9
SiO2	50.29	0.18	0.49	49.05
TiO2	0.04	0.62	0.51	0.06
Al2O3	1.36	67.08	66.11	0.39
Cr2O3	0.00	0.11	0.12	0.00
FeO	18.68	14.66	14.78	25.33
MnO	0.25	0.01	0.01	0.43
NiO	0.01	0.00	0.00	0.00
MgO	5.23	17.66	17.77	0.47
CaO	25.59	0.53	0.38	23.64
Na2O	0.03	0.03	0.06	0.00
Sum	**101.47**	**100.87**	**100.23**	**99.37**

Representative EMP analyses of CAI 2. The comment line gives the name of the individual measurement. Sp=spinell, me=melilite, fas=fassaite, an=anorthite, di=diopside

mineral	**me**	**me**	**fas**	**fas**	**an**	**di**	**me**	**me**	**me**	**me**	**me**
comment	CAI 4a_1	CAI 4a_4	CAI 4a_6	CAI 4a_8	CAI 4a_13	CAI 4a_14	CAI 4a_15	CAI 4b_1	CAI 4b_2	CAI 4b_7	CAI 4b_9
SiO2	26.59	30.35	37.87	37.98	41.71	53.83	25.83	27.02	0.01	22.90	28.39
TiO2	0.00	0.00	7.67	7.80	0.00	0.09	0.01	0.04	0.24	0.03	0.00
Al2O3	28.90	24.14	19.92	20.61	35.76	1.34	30.01	26.42	71.11	35.08	24.75
Cr2O3	0.02	0.00	0.04	0.06	0.01	0.05	0.01	0.01	0.14	0.00	0.00
FeO	0.04	0.01	0.00	0.00	0.12	0.06	0.05	0.01	1.51	0.10	0.04
MnO	0.01	0.00	0.03	0.00	0.00	0.00	0.00	0.00	0.03	0.00	0.00
NiO	0.00	0.03	0.02	0.00	0.01	0.00	0.01	0.00	0.01	0.01	0.02
MgO	2.96	5.19	9.04	9.07	0.29	18.52	2.82	3.96	27.16	0.89	4.49
CaO	41.48	41.50	25.24	25.35	20.86	25.32	41.79	41.14	0.21	41.41	41.22
Na2O	0.11	0.12	0.02	0.00	0.09	0.06	0.03	0.11	0.00	0.06	0.09
Sum	**100.10**	**101.34**	**99.84**	**100.88**	**98.86**	**99.28**	**100.55**	**98.71**	**100.42**	**100.48**	**99.00**

Representative EMP analyses of CAI 3. The comment line gives the name of the individual measurement. All measured fassaites are reported Sp were all stoichiometric with the Mg-rich endmember. Me=melilite, fas=fassaite, grs=grossular.

mineral	**me**	**me**	**fas**	**fas**	**fas**	**fas**	**grs**	**grs**	**fas**	**fas**	**fas**	**me**	**fas**	**me**
comment	CAI 6_1	CAI 6_4	CAI 6_5	CAI 6_6	CAI 6_8	CAI 6_10	CAI 6_12	CAI 6b_6	CAI 6b_11	CAI 6b_12	CAI 6b_13	CAI 6b_15	CAI 6b_16	CAI 6b_18
SiO2	35.15	38.70	38.72	44.24	38.44	41.16	39.47	40.53	40.05	41.62	40.46	33.50	40.37	35.29
TiO2	0.00	0.00	4.68	1.38	5.97	2.99	0.05	0.00	5.10	5.47	5.59	0.00	4.03	0.04
Al2O3	15.00	9.19	18.07	12.73	19.97	20.76	22.36	22.31	17.55	17.95	20.46	18.51	20.02	14.74
Cr2O3	0.00	0.00	0.09	0.07	0.09	0.10	0.00	0.00	0.06	0.13	0.08	0.02	0.08	0.01
FeO	0.01	0.05	0.00	0.00	0.05	0.03	0.03	0.30	0.00	0.02	0.00	0.02	0.00	0.00
MnO	0.02	0.00	0.03	0.01	0.00	0.00	0.00	0.00	0.00	0.00	0.03	0.02	0.00	0.01
NiO	0.00	0.00	0.01	0.02	0.02	0.01	0.00	0.00	0.00	0.02	0.00	0.00	0.00	0.01
MgO	8.66	10.84	10.02	13.26	10.23	10.35	1.37	2.12	10.09	10.59	9.63	7.51	10.45	9.32
CaO	40.88	40.99	28.71	26.97	24.78	25.07	36.98	35.99	27.12	25.02	25.07	40.57	24.72	39.86
Na2O	0.19	0.27	0.06	0.04	0.00	0.06	0.02	0.02	0.02	0.00	0.03	0.15	0.00	0.14
sum	**99.91**	**100.04**	**100.39**	**98.72**	**99.54**	**100.54**	**100.28**	**101.26**	**99.98**	**100.82**	**101.34**	**100.29**	**99.67**	**99.42**

Representative EMP analyses of CAI 4. The comment line gives the name of the individual measurement. All measured fassaites are reported Sp were all stoichiometric with the Mg-rich endmember. Me=melilite, fas=fassaite, an=anorthite, grs=grossular.

Mineral	**me**	**fas**	**an**	**me**	**me**	**an**	**fas**	**grs**	**fas**	**me**	**fas**	**me**	**me**	**fas**
comment	CAI 1_1	CAI 1_02	CAI 1_03	CAI 1_05	CAI 1_08	CAI 1_09	CAI 1_11	CAI 1_12	CAI 1_16	CAI 1_18	CAI 1_19	CAI 1b_1	CAI 1b_5	CAI 1b_6
SiO2	33.79	39.25	42.79	32.51	30.39	44.03	43.23	40.36	38.89	32.21	36.45	29.13	27.62	42.24
TiO2	0.01	6.24	0.08	0.04	0.00	0.02	5.16	0.01	6.74	0.02	9.64	0.00	0.00	0.02
Al2O3	17.10	18.59	36.31	20.10	23.32	35.66	14.54	22.76	19.32	21.56	21.78	25.58	27.10	18.35
Cr2O3	0.00	0.06	0.00	0.01	0.03	0.02	0.05	0.01	0.07	0.01	0.07	0.01	0.00	0.01
FeO	0.02	0.01	0.05	0.00	0.08	0.00	0.00	0.04	0.00	0.02	0.02	0.10	0.13	2.72
MnO	0.02	0.00	0.00	0.02	0.01	0.00	0.00	0.00	0.01	0.00	0.00	0.04	0.00	0.03
NiO	0.07	0.03	0.02	0.44	0.47	0.03	0.00	0.07	0.05	0.12	0.01	0.63	0.01	0.01
MgO	7.97	10.21	0.12	6.60	4.93	0.04	11.51	2.99	9.07	5.76	7.25	4.11	3.79	9.53
CaO	40.77	25.51	20.44	40.68	40.16	20.23	25.57	35.15	25.30	41.77	25.39	38.90	41.84	25.92
Na2O	0.18	0.03	0.10	0.20	0.11	0.07	0.02	0.00	0.04	0.18	0.00	0.19	0.08	0.02
sum	**99.93**	**99.92**	**99.89**	**100.60**	**99.50**	**100.09**	**100.09**	**101.39**	**99.48**	**101.63**	**100.61**	**98.69**	**100.57**	**98.84**

Representative EMP analyses of CAI 5. The comment line gives the name of the individual measurement. Sp were all stoichiometric with the Mg-rich endmember. Me=melilite, an=anorthite, pv=perovskite.

mineral	**me**	**me**	**me**	**me**	**an**	**me**	**me**	**me**	**me**	**me**	**pv**	**me**	**pv**	**me**
comment	CAI 2a_1	CAI 2a_2	CAI 2a_3	CAI 2a_4	CAI 2a_5	CAI 2b_1	CAI 2b_4	CAI 2b_8	CAI 3a_1	CAI 3a_2	CAI 3a_5	CAI 3a_6	CAI 3a_8	CAI 3a_9
SiO2	23.85	24.13	25.20	26.60	43.91	25.94	26.76	24.83	24.03	24.43	4.73	24.99	0.14	24.83
TiO2	0.11	0.10	0.04	0.08	0.00	0.06	0.03	0.06	0.20	0.07	48.71	0.05	57.13	0.09
Al2O3	31.74	32.88	30.91	31.69	35.89	29.47	28.41	29.98	32.67	32.09	3.87	29.92	0.39	30.26
Cr2O3	0.00	0.02	0.00	0.00	0.00	0.00	0.02	0.00	0.01	0.01	0.00	0.00	0.02	0.00
FeO	0.00	0.00	0.00	0.43	0.12	0.06	0.06	0.01	0.20	0.01	0.15	0.07	0.00	0.03
MnO	0.00	0.04	0.01	0.02	0.00	0.00	0.00	0.01	0.00	0.00	0.03	0.00	0.05	0.00
NiO	0.03	0.03	0.03	0.21	0.14	0.02	0.02	0.01	0.13	0.05	0.21	0.03	0.00	0.02
MgO	1.70	1.80	2.49	2.18	0.23	2.83	3.35	2.48	1.99	1.97	0.89	2.47	0.02	2.65
CaO	41.83	41.80	41.62	39.11	19.69	41.54	41.41	41.93	41.49	41.96	40.63	42.08	42.08	41.84
Na2O	0.03	0.00	0.01	0.17	0.48	0.03	0.00	0.00	0.16	0.01	0.03	0.03	0.05	0.03
sum	**99.29**	**100.79**	**100.30**	**100.48**	**100.46**	**99.95**	**100.06**	**99.32**	**100.87**	**100.60**	**99.26**	**99.64**	**99.87**	**99.75**

Appendix C: Trace element concentrations of CAIs

Sample ID	CAI_C-BN_1 µg/g	CAI_C-BN_2 µg/g	CAI_C-BN_3 µg/g	CAI_C-BN_4 µg/g	CAI_C-BN_5 µg/g	CAI_C-BN_6 µg/g
Li / 7	2.67	1.40	0.975	0.559	2.16	1.52
Sc / 45	11.6	24.6	16.9	136	49.5	48.5
V / 51	148	536	706	1166	488	285
Cr / 52	1410	1150	855	520	852	2570
Co / 59	205	196	164	206	261	478
Ni / 60	4010	4070	3570	5080	6200	9750
Cu / 63	30.5	29.4	23.1	40.0	29.4	71.5
Zn / 66	317	146	103	91.3	155	164
Ga / 71	8.66	2.67	2.32	0.883	3.00	5.48
Rb / 85	8.08	0.944	1.07	0.570	0.731	1.45
Sr / 88	43.3	118	115	147	125	60.3
Y / 89	1.93	3.12	1.85	32.3	17.2	12.2
Zr / 90	5.27	4.53	4.20	81.4	29.8	30.7
Nb / 93	1.22	1.70	0.100	4.98	1.18	1.99
Mo / 98	1.56	1.79	0.930	15.5	6.50	5.53
Sn / 120	1.01	0.309	4.29	0.127	0.153	0.340
Sb / 121	0.362	0.059	0.185	0.026	0.061	0.081
Cs / 133	0.181	0.072	0.069	0.058	0.037	0.103
Ba / 138	12.9	37.6	37.4	61.6	28.8	10.7
La / 139	2.15	2.44	5.38	4.80	4.44	1.96
Ce / 140	6.17	6.05	9.65	12.2	10.5	4.73
Pr / 141	0.930	0.932	2.05	1.87	1.71	0.76
Nd / 146	4.50	4.86	10.7	9.52	8.69	3.98
Sm / 147	1.64	1.56	3.08	3.09	2.70	1.31
Eu / 151	0.464	0.915	0.994	1.20	0.942	0.463
Gd / 157	0.868	2.85	1.81	4.43	3.05	1.68
Tb / 159	0.146	0.487	0.309	0.815	0.538	0.308
Dy / 163	0.775	3.00	1.66	5.58	3.46	2.08
Ho / 165	0.099	0.316	0.123	1.17	0.665	0.449
Er / 166	0.264	0.405	0.241	3.28	1.80	1.30
Tm / 169	0.261	0.317	0.352	0.482	0.352	0.216
Yb / 172	1.05	1.47	2.12	3.04	1.55	1.02
Lu / 175	0.051	0.035	0.033	0.490	0.246	0.202
Hf / 178	0.206	0.127	0.126	1.96	0.792	0.790
Ta / 181	0.132	0.181	0.011	0.269	0.166	0.116
W / 182	0.730	0.652	0.153	1.78	0.900	0.701
Tl / 205	0.059	0.032	0.026	0.023	0.042	0.064
Pb / 208	2.89	1.46	1.32	0.357	0.715	1.17
Th / 232	0.176	0.203	0.331	0.534	0.394	0.220
U / 238	0.070	0.041	0.046	0.064	0.139	0.044

Erklärung

Ich versichere, dass ich die von mir vorgelegte Dissertation selbständig angefertigt, die benutzten Quellen und Hilfsmittel vollständig angegeben und die Stellen der Arbeit − einschließlich Tabellen, Karten und Abbildungen −, die anderen Werken im Wortlaut oder dem Sinn nach entnommen sind, in jedem Einzelfall als Entlehnung kenntlich gemacht habe; dass diese Dissertation noch keiner anderen Fakultät oder Universität zur Prüfung vorgelegen hat; dass sie − abgesehen von unten angegebenen Teilpublikationen − noch nicht veröffentlicht worden ist, sowie, dass ich eine solche Veröffentlichung vor Abschluss des Promotionsverfahrens nicht vornehmen werde. Die Bestimmungen der Promotionsordnung sind mir bekannt. Die von mir vorgelegte Dissertation ist von Prof. Dr. Carsten Münker betreut worden.

Nachfolgend genannte Teilpublikationen liegen vor:

Pfeifer, M., Lloyd, N. S., Peters, S. T. M., Wombacher, F., Elfers, B.-M., Schulz, T., Münker, C. (2017) Tantalum isotope ratio measurements and isotope abundances determined by MC-ICP-MS using amplifiers equipped with 10^{10}, 10^{12} and 10^{13} Ohm resistors. *Journal of Analytical Atomic Spectrometry*, **32**, 130-143.

09.11.2017

Datum Unterschrift